A GAS-CERENKOV TELESCOPE EXPERIMENT TO OBSERVE COSMIC GAMMA-RAYS
HOFFMAN, JEFFREY ALAN
ProQuest Dissertations and Theses; 1971; ProQuest Dissertations & Theses Global

INFORMATION TO USERS

This dissertation was produced from a microfilm copy of the original document. While the most advanced technological means to photograph and reproduce this document have been used, the quality is heavily dependent upon the quality of the original submitted.

The following explanation of techniques is provided to help you understand markings or patterns which may appear on this reproduction.

1. The sign or "target" for pages apparently lacking from the document photographed is "Missing Page(s)". If it was possible to obtain the missing page(s) or section, they are spliced into the film along with adjacent pages. This may have necessitated cutting thru an image and duplicating adjacent pages to insure you complete continuity.

2. When an image on the film is obliterated with a large round black mark, it is an indication that the photographer suspected that the copy may have moved during exposure and thus cause a blurred image. You will find a good image of the page in the adjacent frame.

3. When a map, drawing or chart, etc., was part of the material being photographed the photographer followed a definite method in "sectioning" the material. It is customary to begin photoing at the upper left hand corner of a large sheet and to continue photoing from left to right in equal sections with a small overlap. If necessary, sectioning is continued again — beginning below the first row and continuing on until complete.

4. The majority of users indicate that the textual content is of greatest value, however, a somewhat higher quality reproduction could be made from "photographs" if essential to the understanding of the dissertation. Silver prints of "photographs" may be ordered at additional charge by writing the Order Department, giving the catalog number, title, author and specific pages you wish reproduced.

University Microfilms
300 North Zeeb Road
Ann Arbor, Michigan 48106
A Xerox Education Company

Reproduced with permission of the copyright owner. Further reproduction prohibited without permission.

72-15,058

HOFFMAN, Jeffrey Alan, 1944-
A GAS-ČERENKOV TELESCOPE EXPERIMENT TO OBSERVE COSMIC GAMMA RAYS. [Pages 144-147, Appendix II: "Gas-Čerenkov Detector For Low Energy Gamma Ray Astronomy", not microfilmed at request of school. Available for consultation at Harvard College Observatory Library].

Harvard University, Ph.D., 1971
Astrophysics

University Microfilms, A XEROX Company, Ann Arbor, Michigan

Reproduced with permission of the copyright owner. Further reproduction prohibited without permission.

A GAS-ČERENKOV TELESCOPE EXPERIMENT TO OBSERVE COSMIC GAMMA RAYS

A Thesis Presented

by

Jeffrey Alan Hoffman

to

The Department of Astronomy

in partial fulfillment of the requirements

for the degree of

Doctor of Philosophy

in the subject of

Astronomy

Harvard University

Cambridge, Massachusetts

May, 1971

Reproduced with permission of the copyright owner. Further reproduction prohibited without permission.

PLEASE NOTE:

Some pages may have

indistinct print.

Filmed as received.

University Microfilms, A Xerox Education Company

Reproduced with permission of the copyright owner. Further reproduction prohibited without permission.

ABSTRACT

The gas-Čerenkov balloon-borne cosmic gamma ray detector described here has a variable energy threshold and is sensitive down to 15 MeV with a half-angle resolution of 5° to 7°. Gamma rays are detected by a coincidence between light pulses in a scintillator at the top of the detector and pulses of Čerenkov light collected by a mirror at the bottom of the detector. Gamma rays convert or Compton scatter in the scintillator, and the resulting electrons emit Čerenkov radiation as they move through the 2 m gas column between the scintillator and the mirror.

The detector's efficiency and angular response were calculated by a Monte Carlo simulation and checked experimentally by a calibration with gamma rays and electrons.

The detector was flown in a balloon from Palestine, Texas on 29 September, 1970 and observed M87, the Crab Nebula, and the atmospheric gamma ray background. The background measurements, combined with other measurements at higher energies, show a flattening of the atmospheric gamma ray spectrum below 50 MeV, caused by the superposition of a pion-produced gamma ray spectrum peaked at 70 MeV on a power law bremsstrahlung spectrum.

No gamma ray flux was seen from M87 with a 95% confidence upper limit of $F_\gamma(>15\text{MeV}) < 2.7 \times 10^{-4}\ \gamma\text{cm}^{-2}\text{sec}^{-1}$. No statistically significant flux was detected from the direction of the Crab Nebula, although a 1σ excess of gamma ray counts was observed. The corresponding 95% confidence upper limit to the total gamma ray flux from the Crab is $F_\gamma(>15\text{MeV}) < 4.7 \times 10^{-4}\ \gamma\text{cm}^{-2}\text{sec}^{-1}$. The gamma rays from the direction

Reproduced with permission of the copyright owner. Further reproduction prohibited without permission.

of the Crab were phase analyzed for the period of the pulsar NP0532, but no pulsed structure was observed, setting a 95% confidence upper limit on the pulsed gamma ray flux from NP0532 of $F_\gamma(>15\text{MeV}) < 1.4 \times 10^{-4}\ \gamma\text{cm}^{-2}\text{sec}^{-1}$.

Further balloon flights are planned, with improvements in the detector which should increase its sensitivity at least threefold.

Reproduced with permission of the copyright owner. Further reproduction prohibited without permission.

ACKNOWLEDGMENTS

The successful construction and operation of this detector would have been impossible without the constant help and encouragement I received from Dr. Henry Helmken, my thesis adviser, to whom I am deeply grateful. I also appreciate the contributions of several other people to my work on this experiment. In particular, my thanks go to Dr. Giovanni Fazio, whose office door was never closed when I wanted to discuss a problem; to Val Puopolo, who in addition to building so many parts of the detector, has given me an appreciation of the artistry in a research machinist's work; to Jinny Rosenthal, who patiently and skillfully typed this thesis; and to Δρυσ, who kept me company during many late nights at the observatory.

Reproduced with permission of the copyright owner. Further reproduction prohibited without permission.

PREFACE

Readers wishing to glean the main points of this thesis without wading through the technical details of electronics design, calibration, etc. should read first Appendix 2 and then Chapter IV. While some of the results have been modified since the paper (Helmken and Hoffman, 1970) comprising Appendix 2 was published (because of modifications in the detector) this article gives a good, brief description of the detector, the results of the Monte Carlo simulation, and calculations of the predicted sensitivity of the detector for observing cosmic gamma ray sources. Chapter IV describes the results of the first balloon flight of the detector and includes at the end a discussion of ways of improving the detector's sensitivity for future balloon flights.

Reproduced with permission of the copyright owner. Further reproduction prohibited without permission.

TABLE OF CONTENTS

ABSTRACT ii

ACKNOWLEDGMENTS iv

PREFACE v

TABLE OF CONTENTS vi

LIST OF TABLES x

LIST OF ILLUSTRATIONS xi

INTRODUCTION 2

I. Gamma Ray Astronomy 2

II. Production Mechanisms 3

III. Experimental Techniques and Difficulties of the 10-100 MeV Region 7

THE DETECTOR 18

I. Basic Operation 18

II. Detector Design 20

Converter-Scintillator 20

Mirror 23

Gas 24

Canister and Frame 25

III. Electronics 31

Detection of Gamma Rays 31

Housekeeping 33

IV. Pointing System 35

Reproduced with permission of the copyright owner. Further reproduction prohibited without permission.

V. Monte Carlo Study of the Detector 41
Results 44
Gas Pressure. 45
Energy Response 45
Integral Efficiency 49
Corrections to Monte Carlo Results. 51
Energy Discrimination 52
Energy Threshold. 55

VI. Predicted Noise, False Events, and Charged Particle . . . 57
Rejection

TESTING AND CALIBRATION 63
I. Laboratory Testing. 63
Coincidence Plateau 63
Random Coincidence Rate 63
Shutter and A2 Shield 65
Detector Count Rate vs. Čerenkov Threshold Energy . . 66
II. LINAC Calibration 70
Introduction. 70
Experimental Setup. 72
Electron Results. 75
Gamma Ray Results 82
III. Anticoincidence Efficiency. 83
Laboratory Testing. 83
LINAC Anticoincidence Inefficiency Tests. 88

Reproduced with permission of the copyright owner. Further reproduction prohibited without permission.

BALLOON FLIGHT AND RESULTS 96

I. Flight Description 96

II. Background Radiation 97

Ascent 97

Zenith Angle Dependence. 101

Measured Atmospheric Gamma Ray Intensity 103

Pulse Height Analysis. 107

III. Reduction of Pointing Information. 109

Preflight Testing. 109

Post-Flight Analysis 110

IV. M87. 113

Results of 29 September, 1970 Flight 113

Comparison with Other Detectors and Interpretation . . 113

V. Crab Nebula. 116

Search for Steady Emission 116

Search for Pulsed Gamma Rays from NP0532 117

VI. Expected Sensitivity with Improvements in the Detector . . 124

APPENDIX I: DESCRIPTION OF MONTE CARLO PROGRAM FOR SIMULATION 128
OF THE DETECTOR

I. Gamma Ray Interactions 128

II. Electron Energy Loss 130

III. Multiple Scattering. 132

IV. Angular Transformation for Scattering. 133

V. Čerenkov Radiation in the Gas. 136

VI. Efficiency Calculation 139

Reproduced with permission of the copyright owner. Further reproduction prohibited without permission.

APPENDIX II: GAS-ČERENKOV DETECTOR FOR LOW ENERGY GAMMA RAY ASTRONOMY (H. Helmken and J. Hoffman, Nuclear Instruments and Methods, 80, 125) 144

REFERENCES 149

Reproduced with permission of the copyright owner. Further reproduction prohibited without permission.

LIST OF TABLES

Table		Page
1.	Čerenkov Radiation and Multiple Scattering Properties of Various Gases	26
2.	Monte Carlo Results Showing for Various Gamma Ray Energies the Relative Fractions of Compton Scattering and Pair Production Interactions and the Fraction of Detected Events Giving Čerenkov Light Levels Corresponding to Two Čerenkov-Radiating Electrons	53
3.	Anticoincidence Inefficiency vs. Electron Beam Rate with Detector Turned 180° in LINAC Beam	91
4.	Atmospheric Gamma Ray Measurements	104
5.	Pulse Height Distribution of Atmospheric Radiation	108

Reproduced with permission of the copyright owner. Further reproduction prohibited without permission.

LIST OF ILLUSTRATIONS

Figure		Page
1.	Gamma Ray Interaction Cross-Sections in Air	8
2.	Inversion of Compton Scattering Formulae.	10
3.	Mean Energy and Angle of Gamma Rays Producing Observed Electrons for Two Values of Incident Gamma Ray Spectral Index	12
4.	Schematic of Gamma Ray Telescope	19
5.	Placement of Photomultipliers for Viewing Scintillation Light from a Large Scintillator Plate	22
6.	Lower Section of Cannister, Base, and Inner Support Structure of the Detector	29
7.	RCA 4522 Support Structure and Čerenkov Light-Collecting Mirror	30
8.	Block Diagram of Detector Electronics	32
9.	Pulse Height Analyzer	34
10.	Azimuth Drive Unit	37
11.	Detector Suspended from Pointing System	38
12.	Pointing System Stability; Damped Suspension Line Oscillations Superimposed on Balloon Rotation	39 40
13.	Sun Sensor Schematic and Output	42
14.	Differential Efficiency vs. Off-Axis Angle for 50 MeV Gamma Rays with Different Pressures of Propane	46
15.	Detector Efficiency vs. Off-Axis Angle for Various Gamma Ray Energies	47
16.	Integral Efficiency vs. Incident Gamma Ray Threshold Energy for Different Incident Gamma Ray Spectral Indices	50
17.	Fraction of Detected Gamma Ray Events Producing Two Light-Producing Electrons vs. Gamma Ray Differential Spectral Index	54
18.	Folding of Detector Efficiency and Incident Power Law Gamma Ray Spectra for Two Incident Gamma Ray Spectral Indices	56

Reproduced with permission of the copyright owner. Further reproduction prohibited without permission.

19. Coincidence Timing Plateau between RCA4522 and Converter-Scintillator Photomultipliers 64

20. Sea-Level Count Rates vs. Effective Čerenkov Threshold Energy for Muons 67

21. Various Beam-Detector Configurations 73

22. Energy Distribution of Gamma Rays Used in LINAC Calibration 76

23. Efficiency of Detector for 60 MeV on-axis Electrons vs. Horizontal Distance from Axis 78

24. Efficiency of Gamma Ray Detector in Detecting 60 MeV Electrons vs. off-axis Angle 79

25. Half-angle of Gamma Ray Detector Acceptance Cone vs. Incident Gamma Ray Energy 81

26. Scintillator Configurations for Measuring Anticoincidency Inefficiency 84

27. Passive Mixing of N Inputs with Internal Impedance R_1 . . . 85

28. Various Pulse Shapes and Discriminator Firing Modes 87

29. Increase in Anticoincidence Inefficiency with Electron Beam Rate 89

30. Pulse Bunching after Principal Electron Pulse 92

31. Gamma Ray and Charged Particle Coincidence Rates vs. Altitude (0° Zenith Angle) 98

32. Photomultiplier Singles Rates vs. Altitude, Time 99

33. Gamma Ray Count Rate vs. Overlying Air Pressure 100

34. Angular Dependence of Background Gamma Rays in the Atmosphere 102

35. Electromagnetic Spectrum of M87 with Present and Previous High-Energy Observations 114

36. The Hard X-Ray Spectrum of the Crab Nebula 118

37. Gamma Rays from the Direction of NP0532 Phase-Analyzed for a Period of 33.1129 msec 120

38. X-Ray and Gamma Ray Observations of NP0532 122

39. The Electromagnetic Spectra of the Crab Nebula and the Pulsar NP0532, and the Calculated Compton-Synchrotrom radiation 123

Reproduced with permission of the copyright owner. Further reproduction prohibited without permission.

40. Coördinates Used in Monte Carlo Simulation 134

41. Calculation of New Trajectory Coördinates after Scattering . 135

42. Position of Center of Čerenkov Light Circle in Focal Plane . 137

43. Formation of Ring Image of Čerenkov Light Cone from Different Heights along the Trajectory of a Radiating Particle 138

44. Intersection of Čerenkov Light Circle and Photomultiplier Face 140

45. Flow Chart of Computer Program for Monte Carlo Simulation of Gamma Ray Detector 142

Reproduced with permission of the copyright owner. Further reproduction prohibited without permission.

INTRODUCTION

Reproduced with permission of the copyright owner. Further reproduction prohibited without permission.

INTRODUCTION

I. Gamma Ray Astronomy

Modern astronomy has for the past quarter century been probing new portions of the electromagnetic spectrum to gain knowledge about physical conditions in other parts of the universe. Optical observations, made first over three hundred years ago by Galileo, are now complimented and extended by observations of radio, infrared, ultraviolet, and X-ray photons. Starting about ten years ago, astronomers and nuclear physicists joined forces to extend the range of astronomical observations to gamma rays, the highest energy electromagnetic radiation.*

The first decade of gamma ray astronomy saw many cleverly-conceived, difficult experiments which succeeded in detecting only one definite source (Clark, et al., 1968) and produced a host of upper limits. Thus gamma ray astronomy has yet to join other branches of astronomy as a rich source of information about the cosmos. However, the sensitivities of gamma ray detectors have been continually improving [an order of magnitude every 2.3 years (Fazio, 1970)], and hopefully the long, dark gamma ray night will soon be ended.

---

*In nuclear physics, the distinction between X-rays and gamma rays is unambiguous, since the former are emitted in transitions of bound electrons between low-lying shells in atoms while the latter are emitted in nuclear transitions. Other processes which occur in space beside nuclear transitions can produce photons with the same and higher energies as those emitted during nuclear transitions, so the astrophysical distinction between X-rays and gamma rays is generally made on the basis of energy alone, with the cutoff being somewhat arbitrary but generally about 100 KeV.

Reproduced with permission of the copyright owner. Further reproduction prohibited without permission.

Gamma ray experimenters have been tempted by the rich rewards that will come from actual source identifications and measurements. Gamma rays carry information about nuclear interactions and other high energy processes occurring in space. Charged cosmic ray particles, of course, carry information about conditions at their sources and along their propagation paths, but they are so deflected by galactic and solar magnetic fields that their arrival directions cannot be unravelled to deduce their paths or places of origin. However, secondary processes in cosmic ray sources will produce gamma rays, which preserve their propagation directions during flight and which are hence a probe of the high energy nuclear and electron processes occurring in the source regions.

Because they are the most penetrating electromagnetic radiation, gamma rays can carry information from farther away than can any other type of radiation. Gamma rays coming from many distant sources may blend into a semi-uniform diffuse background radiation, which would be a powerful cosmological probe. Gamma rays between 0.5-5 MeV can bring information about element production in far-away supernovae (Clayton and Silk, 1969), testing theories of nucleosynthesis, or about cosmic ray activity at high red shifts (Stecker, 1969), testing theories about the formation and evolution of galaxies. Higher energy gamma rays carry information about magnetic field strengths and ambient interstellar and intergalactic photon, matter, and cosmic ray densities.

II. Production Mechanisms

A knowledge of gamma ray production mechanisms is necessary to derive astrophysical information from gamma ray observations. No attempt

Reproduced with permission of the copyright owner. Further reproduction prohibited without permission.

will be made here to provide a complete review of gamma ray source mechanisms. [Good reviews have been given by Fazio (1967) and Gresien (1969). Incomplete reviews may be found in many articles and theses about gamma ray astronomy.] We merely mention briefly the differences in the spectra produced by various source mechanisms in order to show the importance of observations in the 10-100 MeV energy range (the range of the gamma ray detector described in this thesis) for distinguishing among various source mechanisms. Spectra of high energy particles and photons often take the form of a power law:

$$\frac{dN(E)}{dE} = N_0 E^{-\Gamma}$$

N is the number of particles, E is the energy of the particles, and Γ is the differential spectral index. The measurement of this spectral index for gamma rays is critical in determining which source mechanism produces the observed radiation.

High energy protons with spectral index Γ_p will collide with ambient matter in a source and produce, among other things, neutral pions, which decay into gamma rays. The resulting gamma ray spectral index is somewhat dependent on the functional representation of the dependence of pion production multiplicity on incident proton energy, but the standard result* (multiplicity $\propto E_p^{1/4}$) gives a gamma ray spectral index (for $E_\gamma > 1$ GeV): $\frac{4}{3}(\Gamma_p - \frac{1}{2})$. At lower energies the gamma ray spectrum flattens (Stecker, 1970), with a maximum at $\sim$ 70 MeV for gamma rays produced near the observer. The spectrum is symmetric about its peak when plotted on a log-log graph (i.e., the differential spectral index of the radiation above the peak is the negative of the index below the peak). High energy proton collisions far away in the universe produce

*Gould and Burbidge, 1965

Reproduced with permission of the copyright owner. Further reproduction prohibited without permission.

gamma ray spectra whose peaks we observe redshifted to 70 MeV/(1+z), where z is the redshift corresponding to the distance at which the gamma ray production occurs. A pion-produced gamma ray spectrum is always recognizable by its peak at $\lesssim$ 70 MeV, unless cosmological production occurs at many redshifts, smearing out the peak. Pion-produced gamma rays provide information about the ambient matter density and high energy proton density in source regions.

High energy electrons can produce gamma rays through three processes. Electrons with spectral index Γ_e colliding with ambient matter produce bremsstrahlung gamma rays with the same spectral index Γ_e. If the electrons move in a magnetic field, they can emit synchrotron (magnetobremsstrahlung) gamma rays with spectral index $\frac{\Gamma_e + 1}{2}$. Electrons interacting with a flux of photons can Compton-scatter the photons up to gamma ray energies, giving a gamma ray spectral index $\frac{\Gamma_e + 1}{2}$, the same as for synchrotron radiation. For a given incident electron spectrum in a source, bremsstrahlung, synchrotron, and Compton-scattered gamma rays carry information about ambient source matter density, magnetic field strength, and photon density, respectively.

At energies > 100 MeV, the only way to determine the origin of gamma rays is through their spectral index — but this depends on knowing first the primary proton or electron spectral indices (which can sometimes be inferred from radio observations). At high energies, relatively few gamma rays are emitted, so the statistics in separating the observed gamma rays into energy bins to determine the spectral index are poorer than at lower energies, where the presence of more photons allows a more accurate determination of an energy spectrum.

Reproduced with permission of the copyright owner. Further reproduction prohibited without permission.

The main advantage of observing gamma rays with $E_\gamma < 100$ MeV is the ability to distinguish pion-produced gamma rays from electron-produced gamma rays by detecting excess radiation at $\sim$ 70 MeV, the peak of pion-produced gamma ray spectra. Measurements of synchrotron radio emission allow determination of the combined electron-magnetic energies in radio sources. Even if the magnetic field strength could be independently determined, allowing a determination of the total electron energy in a source, the source energetics would still be incompletely understood without a knowledge of the ratio of the total proton and other heavier cosmic ray energy to the total electron energy. Synchrotron radiation decreases as the mass of the radiating particle squared, so proton synchrotron radiation is not observed from radio sources. The observation of pion-decay gamma rays would, however, give information about proton energetics. A gamma ray source will probably be emitting synchrotron radiation or bremsstrahlung in the X-ray region, so a pion-decay gamma ray spectrum will appear as a bump on the high energy extension of the X-ray spectrum. If the X-rays are produced by bremsstrahlung, then the relative sizes of the pion-decay bump and the straight line spectrum provide a direct comparison of the proton and electron energy densities in the source, the ambient particle density being the same for both. If the X-rays are synchrotron radiation, the comparison is more difficult, since the ambient particle density does not enter into the synchrotron formula. Nevertheless, the assumptions needed to make models of radio and X-ray sources would be enormously reduced by gamma ray observations. The 10-100 MeV gamma ray energy range is the most critical for making these observations because of the location of the pion-decay peak.

Reproduced with permission of the copyright owner. Further reproduction prohibited without permission.

III. Experimental Techniques and Difficulties of the 10-100 MeV Region

An excellent review of experimental methods in gamma ray astronomy and the special difficulties encountered in various energy ranges can be found in Greisen (1969). Other good reviews are in Fazio (1967), Duthie (1968), Kraushaar (1969), and Gresien (1966). We will not duplicate these reviews here, but will rather concentrate on a few considerations relevant to the detector whose development, testing, and use is the subject of this thesis.

There are theoretically twelve ways for gamma rays to interact with matter (Evans, 1955). Most of these processes have extremely small cross sections and can be neglected compared to the three main interaction modes: the photoelectric effect, Compton scattering, and pair production. Gamma rays, being neutral photons, are not detected directly, rather through the secondary electrons they produce by the three processes just mentioned. Information desired about gamma ray energies and directions can be gotten only insofar as this information is preserved by the electrons. Figure 1 shows cross sections for the various interactions of gamma rays with air, which is similar in mean atomic number and hence gamma ray interaction cross sections to the hydrocarbon scintillator material (polystyrene) with which gamma rays interact in the detector described here. For energies above 200 KeV, the photoelectric effect is negligible. The energy region with the minimum total cross section lies between 10 and 100 MeV. This low gamma ray interaction probability makes high detection efficiency difficult to achieve in this energy region. At energies $\lesssim$ 20 MeV, Compton scattering is the predominant mode of gamma ray interaction with polystyrene scintillator material. Graphs of the Compton cross section $\sigma(E_\gamma,\theta)$ are usually plotted for different

Reproduced with permission of the copyright owner. Further reproduction prohibited without permission.

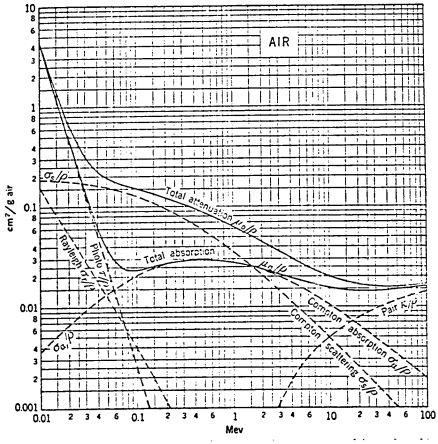

Figure 1

Gamma Ray Interaction Cross-Sections in Air

(Evans, 1955)

Reproduced with permission of the copyright owner. Further reproduction prohibited without permission.

values of E_γ, the incident gamma ray energy. But in uncollimated gamma ray experiments one sees only the energy and direction of the secondary electron. What is actually desired when analyzing Compton scattering in gamma ray detectors is the distribution of gamma rays which can produce an observed electron of a given energy and direction.

Figure 2 shows the results of inverting the normal Compton scattering formulae. The various curves represent different electron energies. The energy of a gamma ray Compton scattering an electron of given kinetic energy T_e at a given angle ψ to its incident direction is given by

$$E_\gamma = \frac{m_o c^2}{[1 + (2/T_e)]^{1/2} \cos \psi - 1} \qquad (1)$$

The lower curves show the energy of the gamma rays which would Compton scatter electrons of the energy specified for each curve at the angle to the incident gamma ray direction given by the abscissa. The upper curves show the cross sections for these interactions. Without observing the scattered gamma rays, there is an unavoidable ambiguity in determining the arrival directions and energies of incident gamma rays even if the directions and energies of the electrons can be determined exactly. (I.e., A 10 MeV electron can be scattered 0° by a 10 MeV gamma ray or 16° by a 50 MeV gamma ray. With a continuous incident gamma ray spectrum, there is no way to distinguish between these two cases.) The best one can do is to find, for a secondary electron of given energy and direction, the mean value of gamma ray energies and angles which could have produced the observed electron.

Reproduced with permission of the copyright owner. Further reproduction prohibited without permission.

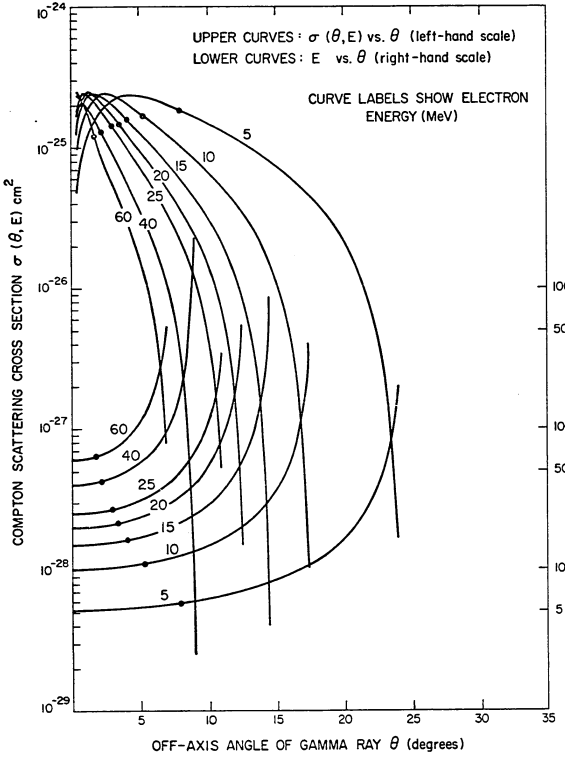

Figure 2

Inversion of Compton Scattering Formulae

Different curves show results for on-axis electrons of different energies.
Heavy points show mean angle and energy of gamma rays producing electrons of the given energy.

Reproduced with permission of the copyright owner. Further reproduction prohibited without permission.

The mean electron scattering angle $\langle\psi\rangle$, for a given secondary electron with kinetic energy T_e is given by

$$\langle\psi\rangle = \frac{\int_0^{\psi_{max}} \psi\sigma(\psi, E_\gamma(\psi)) E_\gamma^{-\Gamma}\, d\psi}{\int_0^{\psi_{max}} \sigma(\psi, E_\gamma(\psi)) E_\gamma^{-\Gamma}\, d\psi} \qquad (2)$$

$\psi_{max} = \arccos[(T_e/(T_e + 2))^{1/2}]$, (corresponding to $E_\gamma = \infty$); $E_\gamma(\psi)$ is the gamma ray energy which will give an electron of the specified energy scattered by an angle ψ, given by equation 1. All incident gamma ray energies are not equally probable. A power law incident gamma ray spectrum has many more low- than high-energy photons, and the number of incident gamma rays at a certain energy should be combined with the interaction probability at that energy in computing the mean Compton scattering angle. The factor $E_\gamma^{-\Gamma}$ in the integrals incorporates the dependence of $\langle\psi\rangle$ on the spectral index of an incident power law spectrum. The mean gamma ray energy for producing a given electron was calculated from $\langle\psi\rangle$ using equation 1. Figure 3 shows, for two separate incident gamma ray power law spectra, the mean gamma ray energy and off-axis angle for the Compton scattering of an electron of given energy observed moving along the detector axis. At 10 MeV, the mean electron Compton scattering angle is on the order of 5°. In most detectors, the loss of angular resolution caused by electron multiple scattering at these energies is far in excess of 5°; but even with no multiple scattering at all, a detector which measures the direction of Compton-scattered electrons to deduce the direction of incident gamma rays is limited by this intrinsic uncertainty. If the direction of the

Reproduced with permission of the copyright owner. Further reproduction prohibited without permission.

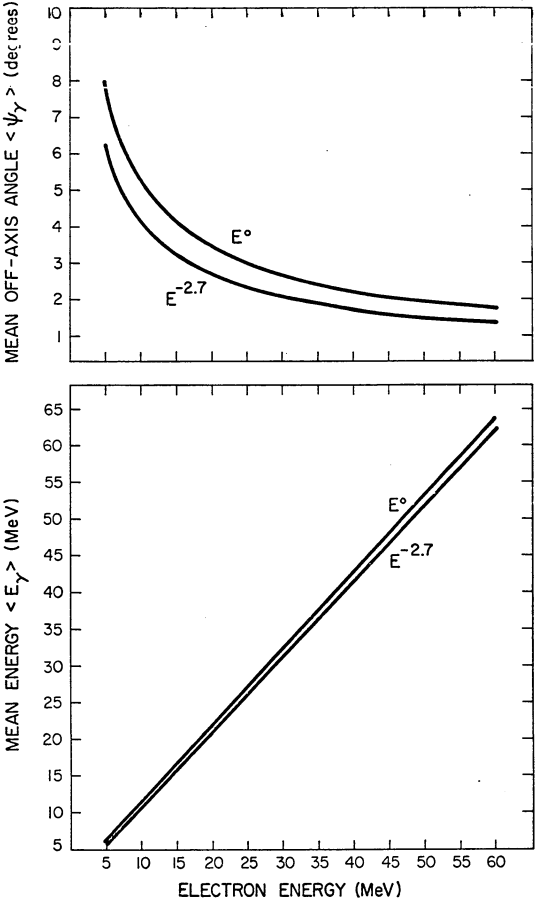

Figure 3

Mean Energy and Angle of Gamma Rays Producing Observed Electrons for Two Values of Incident Gamma Ray Spectral Index

Reproduced with permission of the copyright owner. Further reproduction prohibited without permission.

scattered gamma ray could be determined then this uncertainty would be eliminated; but this would essentially require a second gamma ray detector with a high angular resolution, since the scattered gamma ray angle is very sensitive to small changes in the scattered electron angle when the latter is small. If this gamma ray detector existed, it would be better to use it as the primary detector in the first place.

Pair produced electrons diverge from the incident gamma ray direction with a mean opening angle $\sim m_o c^2/E_\gamma$. For pair production, too, there is an ambiguity in reconstructing the original gamma ray direction and energy from that of the converted electrons, but this is much smaller than for Compton scattering at the same energies. Moreover, as mentioned above, all non-collimated detectors lose by far the most angular information from multiple electron scattering in the converting and detecting material. Low detection efficiencies and difficulty in obtaining good angular resolution are the two main problems plaguing gamma ray detectors in the 20 MeV energy range. These two problems are related, because without collimation, thickening the converting material to increase detection efficiency increases multiple scattering and destroys angular resolution. (The one exception is with nuclear emulsion detectors, where electron paths can be measured near the gamma ray interactions, before much multiple scattering occurs. Nuclear emulsion experiments, however, present monumental data reduction problems, and most research groups have abandoned their use.) If enough photons are detected from a gamma ray source, the angular response of the detector can be "unfolded" from the observations, allowing determination of the position and size of the source to an accuracy greater than the angular resolution of the detector.

Reproduced with permission of the copyright owner. Further reproduction prohibited without permission.

This is a standard technique in X-ray astronomy, where large fluxes have been observed from many objects. It is not yet a realistic technique for gamma ray astronomy, where detection thresholds are still being pushed down to try to observe any fluxes at all.

Additional angular resolution at gamma ray energies $\sim$ 20 MeV without loss in detection efficiency can only come from collimation, which is impractical with present balloon and satellite weight restrictions. Any passive collimation (e.g., lead) which could be carried aloft at present would actually increase the gamma ray background flux because of the gamma rays produced by cosmic ray interactions in the collimator. The use of active collimators has provided good collimation at energies up to several hundred KeV. An active collimator is a shield made of scintillator material thick enough so that almost all incident gamma rays produce electrons before reaching the block of detector scintillator which is encased in the center of the active collimator. Only in one direction is the shielding thin enough to let most gamma rays through, thus providing angular resolution. Any event signalled by the detector is acceptable only if unaccompanied by a pulse from the photomultipliers viewing the collimation scintillator. Since gamma ray interaction cross sections decrease to a minimum somewhere between 1 and 20 MeV for various scintillator materials ($\sim$ 5 MeV in NaI), active collimation for gamma ray detectors in the low-MeV range must be very thick and, regretably, so expensive as to be at present unfeasible.

A detector's angular resolution will be greatest if, once the gamma ray has interacted, the direction of the resulting electron can be determined in a material which causes minimal multiple scattering. The detector described in this thesis uses the Čerenkov radiation

Reproduced with permission of the copyright owner. Further reproduction prohibited without permission.

(electromagnetic "shock" waves produced when charged particles move through a medium faster than the speed of light in that medium) of electrons moving through a column of light gas to determine the directions of the electrons. The electrons suffer only slight multiple scattering in the gas and, since all the Čerenkov light is emitted in a narrow cone coaxial with the electrons' trajectories, a focusing optical system allows determination of their directions with an accuracy of several degrees, which is compatible with the uncertainty caused by multiple scattering in the converting material. Detection efficiency is kept low to prevent excessive multiple scattering in the converting material.

The Čerenkov detection technique minimizes a third problem plaguing gamma ray astronomy experiments — the cosmic ray charged particle background present in space. Since gamma ray experiments detect the electrons produced by gamma rays, they are also sensitive to cosmic ray electrons and especially heavier charged particles which are $\sim 10^2$ times as numerous as electrons. In X-ray astronomy experiments, charged particle radiation is only a small increment to the general background. In the gamma ray energy range, however, cosmic ray protons are $\sim 10^3$ times more numerous than gamma rays and will completely swamp any gamma ray signals unless extremely efficient charged particle rejection techniques are used. Charged particles only Čerenkov radiate if their velocities are greater than the speed of light in the ambient material, and this speed corresponds to a much higher energy for heavy than for light charged particles. If the Čerenkov threshold in the gas column of the detector is E_γ for gamma rays (i.e., for the electrons produced by the gamma rays), the corresponding threshold for protons would be $\frac{m_p}{m_e} E_\gamma$.

Reproduced with permission of the copyright owner. Further reproduction prohibited without permission.

Scintillator or spark chamber detectors would be sensitive to protons with energies down to E_γ, so the heavy charged particle background which a gas-Čerenkov gamma ray detector must guard against is much smaller than the background for other detectors at the same gamma ray energies.

The transition from "doing experiments" to "making observations", which Galileo accomplished for optical astronomy in the time it took him to lift his telescope to his eye, has taken many years for gamma ray astronomy. Gamma ray astronomers of the future will make their observations using huge, collimated detectors in space with 100% detection efficiency combined with excellent angular resolution. Perhaps there will even be gamma ray detectors on the moon, utilizing the lunar horizon to make occultation measurements far more accurate than any collimator would allow.

The detector described here is not the ultimate solution to the problems described above, but was designed to try to minimize to the greatest extent possible with present experimental techniques all the problems plaguing gamma ray astronomy in the energy region 10-100 MeV. The gas-Čerenkov technique, used before in several cosmic ray experiments (Webber and Chotkowski, 1967; May and Waddington, 1969) is new for gamma ray astronomy. This thesis describes the principles of the detector, its design, testing, and calibration, and reports the results of its first balloon flight.

Reproduced with permission of the copyright owner. Further reproduction prohibited without permission.

THE DETECTOR

Reproduced with permission of the copyright owner. Further reproduction prohibited without permission.

THE DETECTOR

I. Basic Operation

Figure 4 shows schematically the gamma ray telescope. Incident gamma rays pair produce or Compton scatter electrons in a 1" polystyrene scintillator slab, henceforth called the converter-scintillator (CS). The efficiency of this detector is inherently low, since a thicker converter would cause too much multiple scattering of the electrons, destroying the detector's angular resolution. Above 10 MeV, most of the electrons will be initially moving within 5° of the incident gamma ray direction (figure 3). Electrons with energy greater than the Čerenkov threshold will Čerenkov radiate after entering the gas, and the light from those moving downward and within 6° of the detector axis will be focussed by a mirror onto a 5" RCA 4522 photomultiplier tube. An event will be indicated by a time-delayed coincidence between the converter-scintillator and the 5" photomultipliers unaccompanied by a pulse from the anticoincidence shield. This coincidence signal will open the gate on a four-channel pulse-height analyzer which analyzes and digitizes the pulses from the 5" photomultiplier. All gamma rays with energy greater than a certain threshold can be detected, but since the energy threshold of the detector varies with pressure ($E_T \propto p^{-1/2}$), varying the pressure of the gas during a flight will allow measurements to be made of I_γ (> E) for several values of E.

The advantageous characteristics of the detector are: 1) a large sensitive area, 2) good angular resolution, 3) excellent rejection of charged particle background, and 4) simplicity of design.

Reproduced with permission of the copyright owner. Further reproduction prohibited without permission.

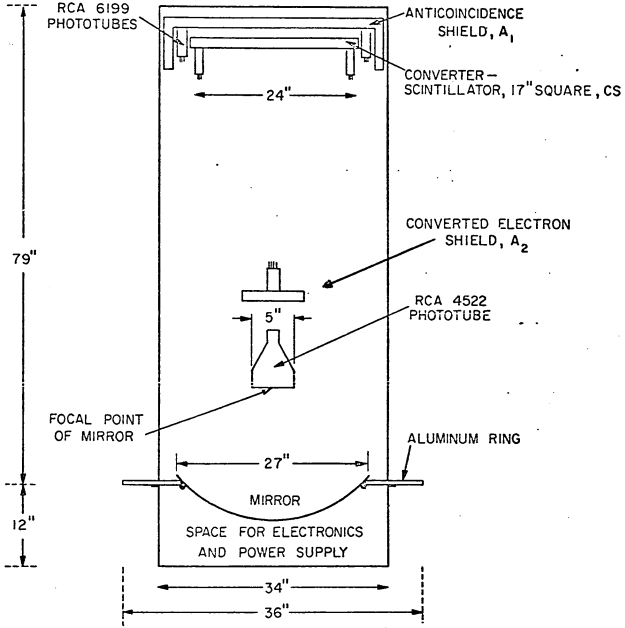

Figure 4

Schematic of Gamma Ray Telescope

Reproduced with permission of the copyright owner. Further reproduction prohibited without permission.

II. Detector Design

The main operational elements of the gas-Čerenkov telescope are the converter-scintillator plate at the top, the light-collecting mirror at the bottom, and the gas between the two. The whole assembly is supported by a tubular frame and surrounded by an aluminum cannister.

Converter-Scintillator

Most high energy gamma ray detectors use lead as the converting medium, with a thin slab or scintillator below the lead to signal the presence of a converted electron. Lead is an efficient converter for gamma rays because of its high Z, and the thin slab of scintillator below the lead causes negligible scattering of the high energy electrons produced by the gamma rays. Low energy electrons, however, suffer considerable multiple scattering in even a thin scintillator slab. The RMS multiple scattering angle for electrons is given by Rossi (1952):

$$\langle\theta^2\rangle^{1/2} \approx \frac{21.2}{E\,(\mathrm{MeV})} \sqrt{\frac{t\rho}{X_0}}, \qquad (3)$$

where E is the electron energy, and t, ρ, and X_0 are the linear thickness, density, and radiation length, respectively, of the scatterer. This predicts 8.5° RMS scattering for 20 MeV electrons in 1 cm of NE-102 polystyrene scintillator material. To keep reasonable angular resolution at low gamma ray energies the converter must be thin, with a resulting low efficiency. If lead is used as the converter, it would be inefficient to have the scattering in the scintillator greater than in the lead. At low gamma ray energies, it is most efficient to use the scintillator itself as the converter. 0.01 cm of Pb scatters 20 MeV electrons 8° RMS

Reproduced with permission of the copyright owner. Further reproduction prohibited without permission.

and gives a conversion efficiency of 0.6%. 1 cm of NE-102 also has a conversion efficiency of 0.6%, so a 2 cm NE-102 slab has the same conversion efficiency and scattering properties as 1 cm of NE-102 underneath 0.01 cm of Pb. The use of a lead converter at these energies clearly has no advantage, and the use of a thicker scintillator results in high light levels in the scintillator, allowing operation of the photomultipliers at relatively low noise levels.

Minimum ionizing electrons should emit about 10^4 photons cm^{-1} in polystyrene, which should be sufficient to preclude any problem in getting enough light into the photomultipliers viewing the scintillator slab. However, the constraints that the detector geometry placed on the location of the photomultipliers, both on the converter-scintillator and on the anticoincidence scintillator, resulted in less than ideal light collection. The best way for a photomultiplier to look at a large-area scintillator slab is edge-on via light guides (figure 5a), since a large fraction of the light is totally internally reflected and reaches the edge. The light from a pulse, after traversing the slab several times, is diffused sufficiently so that it may be considered to be isotropic. Thus, photomultipliers viewing the face of the slab as shown in figure 5b see a fraction of the light from the pulse approximately equal to the ratio of the area of the tube faces to the total surface area of the scintillator, which is much less light than the photomultipliers would see edge-on, where with proper light guides almost all the light can be collected onto the tube faces. Figure 4 shows the configuration of scintillators at the top of the detector. The detector had to be manufactured as much as possible from equipment already available, so we used scintillator slabs from previous experiments. The right angle in

Reproduced with permission of the copyright owner. Further reproduction prohibited without permission.

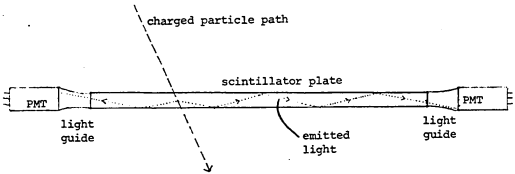

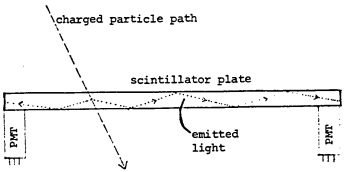

Figure 5

Placement of Photomultipliers for Viewing Scintillation Light from a Large Scintillator Plate

Reproduced with permission of the copyright owner. Further reproduction prohibited without permission.

the anticoincidence shield does not give total reflection. There was not enough room to install the tubes edge-on, so it was necessary to mount all the scintillator-viewing photomultipliers (RCA 6199's) looking at the large-area faces of the scintillator slabs. The resulting poor light collection necessitated operating the 6199's at high voltages, with consequent high noise levels and other problems which will be discussed in the section on anticoincidence efficiency.

Mirror

The ideal mirror for a balloon-borne detector must be light, cheap, resistant against landing shock, and should have a high ultraviolet reflectivity, since Čerenkov emission is peaked toward higher frequencies (Jelley, 1958):

$$\left(\frac{d^2N}{d\ell\, d\lambda}\right) \propto \frac{1}{\lambda^2} \qquad \begin{array}{l}\text{(number of photons per unit path length}\\ \text{per unit wavelength interval)}\end{array} . \quad (4)$$

Because of the large multiple scattering suffered by electrons in the converter-scintillator before emerging into the gas to Čerenkov radiate, the optical detection system must have a fairly large acceptance angle to avoid a loss of efficiency in detecting gamma rays from point sources. The larger the acceptance angle, however, the more background radiation is detected, with a consequent loss in signal-to-noise ratio. (This is true for a point source. When observing a diffuse source of gamma radiation such as the galactic center, a large acceptance angle has a less serious effect on the signal-to-noise ratio.) 20 MeV electrons on the average convert in the middle of the converter-scintillator and are scattered 8.5°. Since higher energy electrons will be scattered less,

Reproduced with permission of the copyright owner. Further reproduction prohibited without permission.

an optimum optical system will have an acceptance angle of slightly less than 8°. An RCA 4522 was chosen to detect the Čerenkov light because it is a fast tube (< 3 nsec risetime) with high amplification (14 stages) and good UV response (50% relative sensitivity at 2450 Å).

We had available some surplus metal searchlight mirrors which, while heavy (cast bronze), had focal lengths of 24", at which the RCA 4522 tube face subtends a half-angle of 6°. Mostly in the interest of time, we decided not to try to manufacture mirrors of ideal specifications but rather to use one of the surplus mirrors. The large acceptance angle avoids any aberration problems, and the metal construction of the mirror is strong enough so that, with reasonable support around the edges, bending will not change the focal length. The mirror is coated with rhodium, whose ultraviolet reflectivity has to our knowledge never been accurately measured. During testing, however, the amount of Čerenkov light reflected into the RCA 4522 was found to be high enough to generate pulses which triggered the discriminator (200 mv.) with no amplification.

Gas

The two requirements for the gas in which the electrons emit Čerenkov radiation are that it provide a high level of Čerenkov light emission and cause a minimum amount of multiple electron scattering. Jelley (1958) shows that the amount of Čerenkov radiation emitted by a particle in a gas of refractive index $n = 1 + \eta$ ($\eta \ll 1$) is proportional to η, which is in turn proportional to the gas pressure p. The threshold energy is given by

$$E_T = \frac{m_o c^2}{\sqrt{2\eta}} \propto \frac{1}{\sqrt{p}} . \qquad (5)$$

Reproduced with permission of the copyright owner. Further reproduction prohibited without permission.

Multiple scattering in the gas can be calculated using equation 3. The gas density ρ is proportional to the pressure p, so the RMS scattering angle will vary as $p^{1/2}$. Thus, increasing the gas pressure lowers the threshold energy and increases multiple scattering. The properties of various gases can be compared only if the pressures are adjusted to give the same energy thresholds for all the gases. Table 1 shows the Čerenkov radiation and multiple scattering properties of propane, air, and CO_2 for various pressures. With an energy threshold (for electrons) of 10.7 MeV, the light output in propane is 8% smaller than in air and 4% smaller than in CO_2. The RMS scattering in propane, however, is only 60% of the scattering in air and 55% of the scattering in CO_2. The small multiple electron scattering in propane makes it preferable to air, CO_2, and all of the other common gases considered for use in the gas-Čerenkov detector. The one gas whose light emission and multiple scattering properties are markedly superior to propane is diethyl ether, whose boiling point (34.6°C)prohibits its use, since it would be a liquid at the temperatures expected inside the detector at balloon float altitudes. A further advantage of propane is that a given threshold energy is obtained for a lower pressure than for most other gases, so a detector using propane does not have to hold as much pressure as if it used another gas and can thus be lighter and cheaper to build.

Cannister and Frame

The cannister which encloses the detector must be able to hold a positive differential pressure of at least 1 atmosphere, withstand a vacuum (for pumping out the air at sea level prior to filling with propane), be

Reproduced with permission of the copyright owner. Further reproduction prohibited without permission.

Čerenkov Threshold Energy E_T(MeV)	Gas Pressure (atmospheres) P			Čerenkov Light Level (photons/cm between 3500 Å and 5000 Å at $\beta = 1$) $dN/d\ell$			RMS Scattering Angle (10 MeV electrons, 100 cm path length) $\langle\theta^2\rangle^{1/2}$		
	Air	Propane	CO_2	Air	Propane	CO_2	Air	Propane	CO_2
10.7	3.7	1.0	2.3	.85	.78	.81	13.7°	8.2°	14.7°
20.6	1.0	.27	.63	.23	.21	.22	7.1°	4.2°	7.6°
30	.47	.13	.30	.11	.10	.10	4.9°	2.9°	5.2°
40	.26	.071	.17	.061	.056	.058	3.7°	2.2°	3.9°
50	.17	.045	.11	.037	.036	.037	2.9°	1.7°	3.1°

Table 1

Čerenkov Radiation and Multiple Scattering Properties of Various Gases

Reproduced with permission of the copyright owner. Further reproduction prohibited without permission.

lightweight, and be completely opaque to light. Both fiberglass and aluminum were considered in designing the cannister. Fiberglass offered some weight advantage, but the cost was so much greater that aluminum was chosen as the structural material. For a time, we considered using sewer culvert for the cannister, to which vacuum flanges could be welded. Ramsey Welding Research, Inc., which did the actual construction, preferred to roll their own cannister out of 3/64" sheet aluminum. Since the price and weight were similar, this method was chosen. (Nevertheless, it was quite instructive for a Ph.D. candidate who had previously had little contact with the business world to have to learn the intricacies of investigating, pricing, and ordering sewer culvert.)

The detector stood 9' high under our lab's 13' ceiling, so the cannister had to be made in three sections in order that it could be put on and taken off without laying the detector on its side. The added expense of two extra sets of flanges proved more than worthwhile in the time saved not only in the laboratory but especially during calibration and preflight preparations.

The base section of a previous balloon-borne experiment served as the base of this detector. The mirror was mounted on the base, and the bottom section of the cannister was welded on. The electronics were mounted on a flat aluminum plate which was bolted onto the bottom of the base. Four tubular aluminum support rods formed the basic skeleton of the frame supporting the scintillators at the top of the detector and the RCA 4522 in the middle. Figures 6 and 7 show the outside of the cannister, the inner support structure, and the mirror.

Reproduced with permission of the copyright owner. Further reproduction prohibited without permission.

Photographs on following pages:

Figure 6: Lower Section of Cannister, Base, and Inner Support Structure of the Detector

Figure 7: RCA 4522 Support Structure and Čerenkov Light-Collecting Mirror

Reproduced with permission of the copyright owner. Further reproduction prohibited without permission.

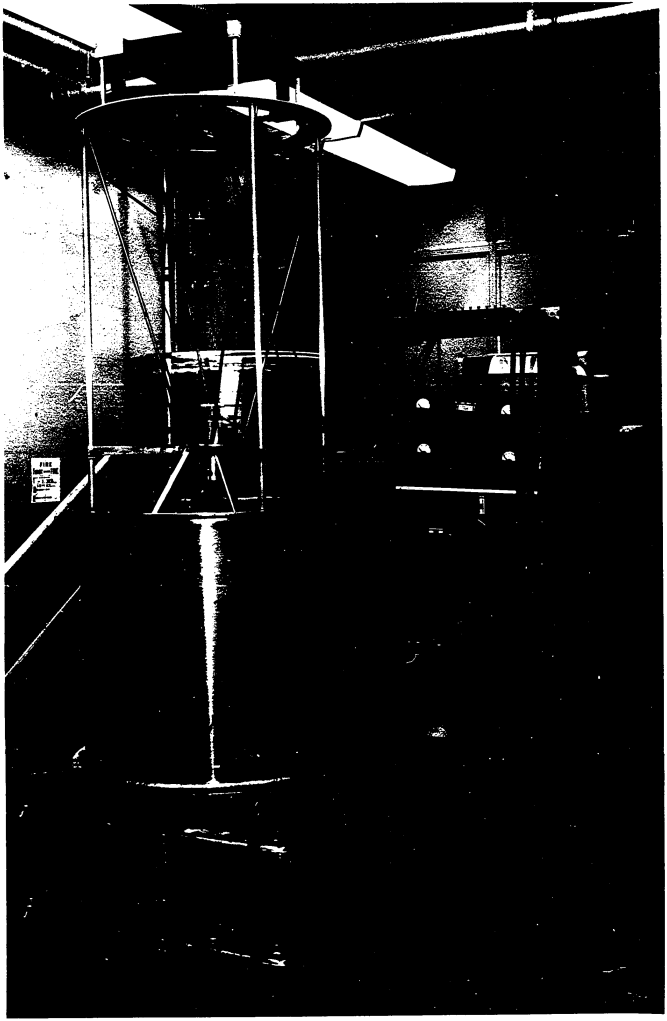

Reproduced with permission of the copyright owner. Further reproduction prohibited without permission.

Reproduced with permission of the copyright owner. Further reproduction prohibited without permission.

III. Electronics

The electronics in the experiment must be able to 1) detect gamma rays, 2) veto charged particle events, 3) pulse-height analyze the Čerenkov light from gamma ray events, and 4) monitor the rates of all the photomultiplier tubes. Figure 8 is a block diagram of the entire electronics circuitry.

Detection of Gamma Rays

12 nanoseconds separate the conversion of a gamma ray in the converter-scintillator and the arrival of Čerenkov light at the 4522 photomultiplier tube; so an event is signalled by a coincidence between a pulse from the converter-scintillator, delayed 12 nanoseconds, and a pulse from the 4522. All the fast-timing electronics were commercially available units in the EGG 200 MHz series. Pulses from the 6199 photomultipliers were mixed as shown in figure 8 (EGG AN100), amplified (EGG AN 201/N), and put into a quad, zero-crossing discriminator (EGG T140/N). Pulses from the 4522 were large enough to trigger the discriminator (threshold ≈ 200 mV) without additional amplification. The discriminator outputs were then put into the coincidence module (EGG C144/N) to determine when gamma ray events took place. The coincidence module has an adjustable output width, which was useful for interfacing with the slower integrated circuit logic. It also has a veto input, which we had originally planned to use to veto charged particle events. The problems in achieving high veto efficiency and the reasons for not using the C144 veto input are described below, in the section on testing.

Reproduced with permission of the copyright owner. Further reproduction prohibited without permission.

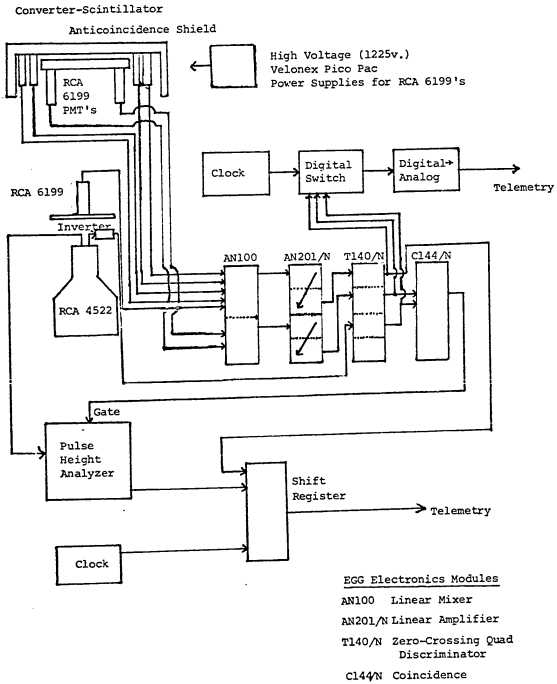

Figure 8

Block Diagram of Detector Electronics

Reproduced with permission of the copyright owner. Further reproduction prohibited without permission.

The coincidence pulse gates a pulse from the RCA 4522 into an integrated circuit four-channel pulse height analyzer, shown in figure 9, which was built in our laboratory. The key components are the Motorola MC1440P sense amplifiers, which have excellent temperature stability ($\sim$ 14μV/°C), ensuring that the pulse height analyzer calibration will not change much during a flight. Adjusting R_1 through R_4 determines the input pulse level required to trigger each successive sense amplifier (nominal threshold $\sim$ 20 mV.). The four pulse height levels are encoded as two bits and, together with one bit containing veto information and one additional bit needed for pulse identification, are parallel-fed into a four-bit shift register (Texas Instruments: SN 7495) and shifted out serially into one channel of the telemetry transmitter. The expected count rate (from charged particles as well as gamma rays) is less than 2 sec^{-1} at float altitude; with a readout time of 6 milliseconds, no pileup problems are expected. An event which occurs before the previous event is read out is rejected without destroying the information for the first event. The first bit of the readout pulse train occurs at a fixed time interval (1.9 msec) after the event, so recording the telemetry signal on magnetic tape along with accurate time information (1 part in 10^8) allows accurate analysis for any periodic gamma ray emission from pulsars.

Housekeeping

Besides receiving information about gamma ray events, the experimenters must be able to monitor the operation of various parts of the detector to make sure that it is functioning properly. Measurements of the pressure and temperature inside the detector, the battery voltages, and the counting

Reproduced with permission of the copyright owner. Further reproduction prohibited without permission.

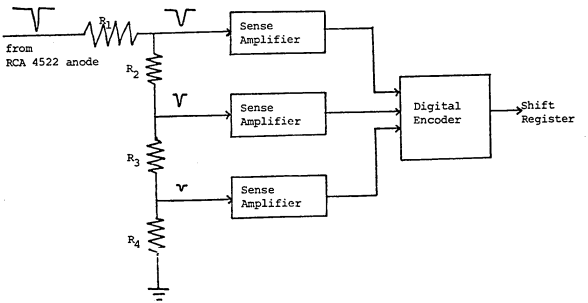

Figure 9

Pulse Height Analyzer

Reproduced with permission of the copyright owner. Further reproduction prohibited without permission.

rates of all the photomultiplier tubes must be telemetered to ground, as must information about the detector's orientation.

One half of the output of each discriminator goes into the coincidence logic circuitry and one half into the photomultiplier rate-monitoring circuit. With this system, only the summed outputs of the converter-scintillator tubes and the anticoincidence shield tubes are monitored, since the individual tube outputs are mixed before entering the discriminators; but this is sufficient for the present experiment, since any large scale change in count rates will be detected. The pulses from each of the discriminator units are stretched and put into different inputs of a digital switch (National Semiconductor: DM 8210) which is driven by an IC clock, sequentially sampling and feeding the outputs of each discriminator into a logarithmic digital-to-analog converter (Solid State Radiations: Model 1015) whose output voltage varies from 0-5 V. logarithmically with the pulse rate. This output voltage drives a voltage-controlled oscillator whose output is transmitted continuously on one of the telemetry channels. Other information transmitted continuously are the outputs of the two pointing system magnetometers. The pressure gauge and thermistor outputs, the battery voltages, and the pointing system outputs from the sun sensor and the elevation-sensing potentiometers are fed into a mechanical cycloswitch commutator and telemetered to ground.

IV. Pointing System

Since the half-angle of the detector is about 6°, only several degrees accuracy is required for the pointing system. The gamma ray astronomy group at the University of Southampton has developed a light,

Reproduced with permission of the copyright owner. Further reproduction prohibited without permission.

relatively simple and inexpensive pointing system for use with their balloon-borne spark chamber. We used their design,with slight modifications, for our detector. Figure 10 is a schematic diagram of the azimuth drive unit of our pointing system. A twenty-four volt d.c. motor (Globe, Inc.) turns the detector via a series of thrust bearings against the suspension lines hanging down from the parachute which is suspended under the balloon. Hanging from the azimuth drive is an aluminum spreader bar on which are located the magnetometers and sun sensor, used to supply orientation information, and the elevation drive motor. The cannister has support arms coming up from the base, which are connected through ball bearings by cables to the spreader bar, allowing the cannister to be tilted away from the vertical. The weight of the cannister is distributed so that the neutral portion is vertical; the elevation drive motor then pulls a cable attached to the base of the detector to tilt the cannister down toward the horizon. This cable can be seen in figure 11, which shows the detector and the pointing system.

Telemetry signals from the ground activate relays onboard the detector to control the pointing system. We chose to use temporary-closing rather than latching relays, since the former gave a better "feel" for the ground controller. This "feel" was quite important, since controlling the pointing system was a delicate task. The tendency to overcompensate for pointing errors had to be suppressed. With practice, we found we could achieve 3° accuracy with no trouble and 1° accuracy with effort and a bit of luck. Figure 12a shows a section of the magnetometer readout from the flight, demonstrating how steady the detector could be held. The two main problems in steering the detector were counteracting the overall rotation of the balloon and oscillations

Reproduced with permission of the copyright owner. Further reproduction prohibited without permission.

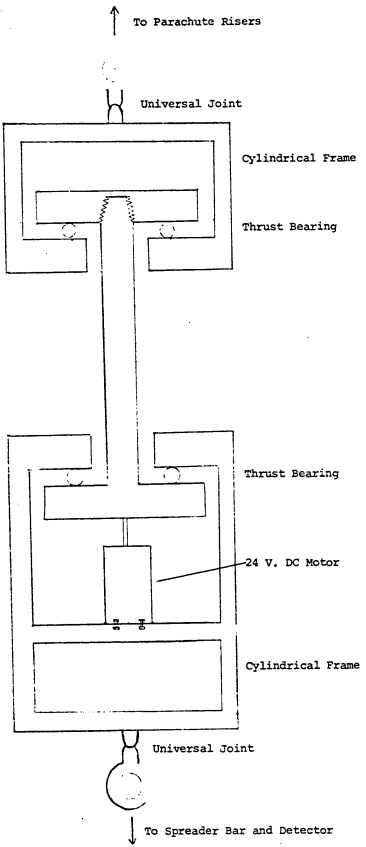

Figure 10

Azimuth Drive Unit

Reproduced with permission of the copyright owner. Further reproduction prohibited without permission.

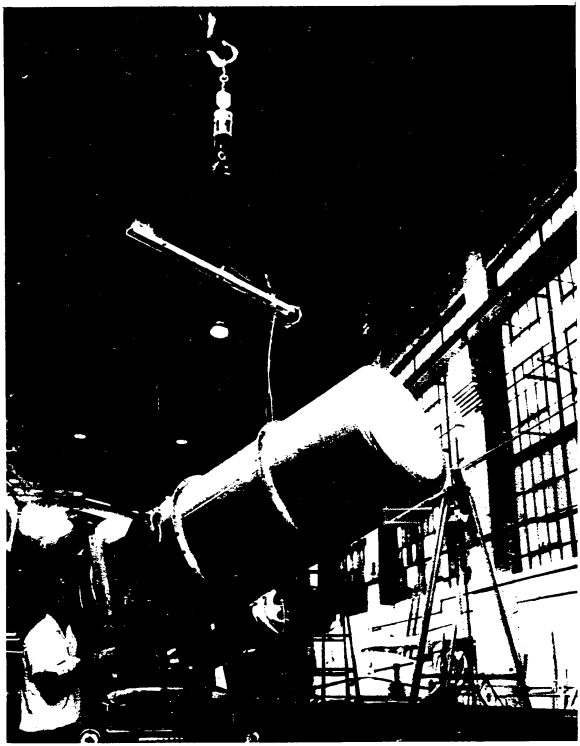

Figure 11. Detector suspended from pointing system.

Reproduced with permission of the copyright owner. Further reproduction prohibited without permission.

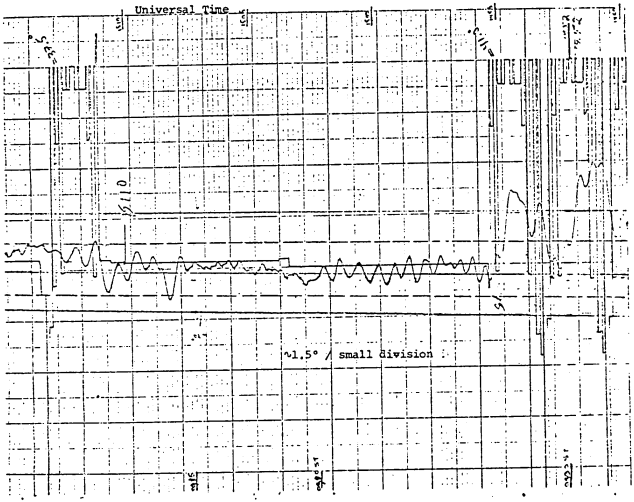

Figure 12a

Pointing System Stability

Reproduced with permission of the copyright owner. Further reproduction prohibited without permission.

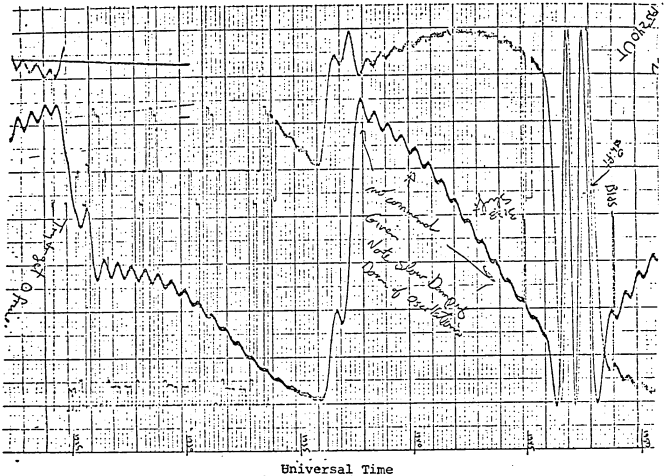

Figure 12b

Damped Suspension Line Oscillations
Superimposed on Balloon Rotation

Reproduced with permission of the copyright owner. Further reproduction prohibited without permission.

in the suspension lines. The magnetometer trace in figure 12b shows relatively fast suspension line oscillations (note the damping) superimposed on a slow rotation of the balloon. (No pointing corrections were applied here, since the detector was making background measurements.)

The magnetometers (Schoenstedt, Inc.) were capable of better than 1° accuracy. Two magnetometers crossed at right angles assured unambiguous quadrant determination. Figure 13 illustrates the sun sensor. The azimuth reading from the magnetometers is used to identify a given peak or trough in the sun sensor output curve, allowing in-flight calibration of the magnetometers to a fraction of a degree.

The vertical position of the gondola was measured by suspending a pendulum bob from the shaft of a rotary potentiometer mounted to the frame inside the cannister. A constant 5 volts was kept across the outer pins of the pot, and the varying voltage from the center pin was put into a VCO and telemetered to ground.

In post-flight analysis, we found that the only real defect of the pointing system was its resemblence to an agricultural tractor hitch. Its thrust-bearing swivel, long spreader bars, and steel cables would make it ideal for pulling heavy farm tools. Recovery of the detector was delayed until nearly twenty-four hours after it was cut down from the balloon, and some local farmer who got to it first is now the proud possessor of a tractor hitch worth as much as his tractor.

V. Monte-Carlo Study of the Detector

Analytical formulae have been developed which describe the physical processes occurring when a gamma ray interacts with the detector

Reproduced with permission of the copyright owner. Further reproduction prohibited without permission.

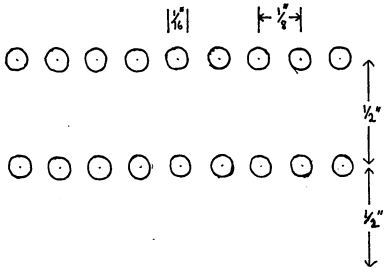

(Top View)

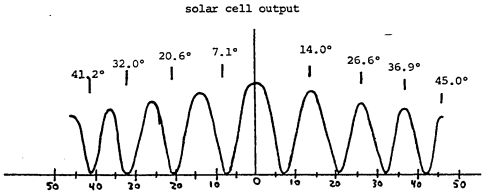

Figure 13

Sun Sensor Schematic and Output

Reproduced with permission of the copyright owner. Further reproduction prohibited without permission.

and the resulting electron moves through the detector material: pair production and Compton scattering by gamma rays (Rossi, 1952), ionization and radiative energy loss by electrons (Rossi, 1952), electron multiple scattering (Scott, 1963), and emission of Čerenkov radiation (Jelley, 1958). However, folding together the angular distributions of all these processes to predict the response of the detector to gamma rays of a given energy and direction is intractable analytically. The random nature of gamma ray interactions and electron multiple scattering make this problem well-suited for Monte-Carlo simulation.

A computer program was developed to simulate the interaction of gamma rays within the detector. The energy and angle with respect to the detector axis of an incoming gamma ray were specified, and the program randomly chose the point at which the gamma ray entered the 17" × 17" × 1" converter-scintillator. It allowed the gamma ray to Compton scatter or pair produce and followed the electrons through the converter and the 80" long column of gas, calculating the energy losses and multiple scattering. The type of gas and the gas pressure could be specified for each simulation. By determining the Čerenkov light emission of the electrons in the gas and calculating the light paths of the photons as they are reflected off the 24" focal length mirror, the program could predict what fraction of gamma rays with a given energy and direction would cause a detectable number of photons to hit the face of the phototube. This gives the efficiency of the detector vs. gamma ray energy and direction.

The various parts of the program are described in detail in Appendix 1, at the end of which can be found a flow chart of the entire program (figure 45).

Reproduced with permission of the copyright owner. Further reproduction prohibited without permission.

Results

The calculations simulated 500 gamma ray interactions (not incident gamma rays) for each specified gamma ray energy, direction, and set of detector characteristics (refractive index of gas, mirror size).

Early results showed that any increase in efficiency for detecting on-axis gamma rays obtained by making the mirror size much larger than the converter-scintillator (to pick up the light from electrons scattered far off-axis) was offset by the corresponding increase in background noise coming from the increased acceptance angle of the detector. All later runs were made to simulate the 27" diameter mirror actually used in the detector.

For each converted gamma ray, the Monte-Carlo results show the number of photons incident on the face of the photomultiplier tube at the focal point of the mirror. Some converted electrons have too little energy to Čerenkov radiate or are multiply scattered out of the optical acceptance angle before emerging from the converter, so photon number distributions for different gamma ray energies and directions typically show a large peak at zero photons. Aside from these zero-photon events, very few events give fewer than thirty photons (when the detector is filled with propane at 1 atm.). The RCA 4522 has a quantum efficiency of $\sim$ 20% and was operated at a sufficiently high voltage and low discriminator threshold to detect single photoelectrons. The probability that n photons striking a photocathode with 20% efficiency will produce no photoelectrons is

$$P_0 = \frac{(n/5)^0}{0!} e^{-n/5} = e^{-n/5} = 2.5 \times 10^{-3} \qquad (n = 30) \ . \qquad (6)$$

So assuming that all events giving any photons at all on the tube face are detected results in a good estimate of the detector's sensitivity.

Reproduced with permission of the copyright owner. Further reproduction prohibited without permission.

The efficiency calculated for detecting converted gamma rays is multiplied by a statistical factor described in the appendix to transform the result to an efficiency for detecting all incident gamma rays. This factor includes the actual conversion probability and the probability that at least one resulting electron has energy greater than the Čerenkov production threshold energy E_T (since to save computer time, the program was constrained to have gamma rays produce only electrons with energy $\geq E_T$).

Gas Pressure

The energy threshold for production of Čerenkov light is inversely proportional to the square root of the gas pressure inside the cannister. Figure 14 shows efficiency vs. angle curves for 50 MeV incident gamma rays at two different pressures of propane gas. The shapes of the curves are basically the same for 1 atm. and 1/8 atm. pressures ($E_{T_{e^-}}$ = 10.7 MeV and 30 MeV, respectively). The main cause of decreased efficiency at the lower pressure is that with a higher Čerenkov threshold, a smaller fraction of 50 MeV gamma rays produce electrons with $E \geq E_T$. A low gamma ray threshold energy is desirable because the background atmospheric gamma ray spectrum is harder than the anticipated spectra of most suspected sources. At lower energies, the source/background ratio is maximized.

Energy Response

Figure 15 shows efficiency vs. angle curves for incident gamma rays of various energies with 1 atm. of propane gas in the detector. As expected, the curves are flatter and lower in absolute magnitude at

Reproduced with permission of the copyright owner. Further reproduction prohibited without permission.

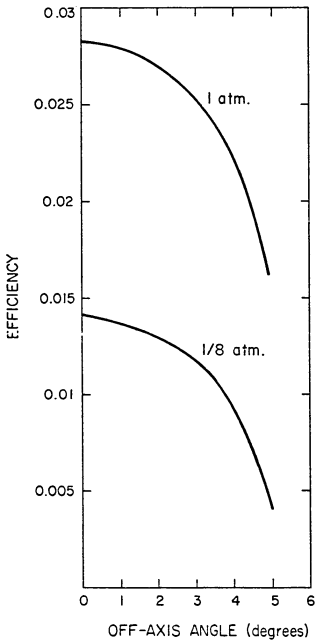

Figure 14

Differential Efficiency vs. Off-Axis Angle for 50 MeV Gamma Rays with Different Pressures of Propane

Reproduced with permission of the copyright owner. Further reproduction prohibited without permission.

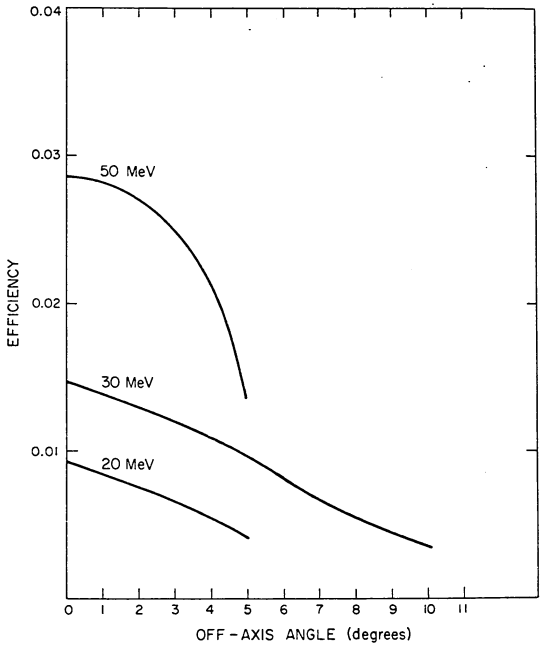

Figure 15

Detector efficiency vs. off-axis angle for various incident gamma ray energies.

Reproduced with permission of the copyright owner. Further reproduction prohibited without permission.

lower energies. The figure shows, however, that the half-angle at 20 MeV is less than the half-angle at 30 MeV (5° vs. 6 1/2°), whereas clearly the detector's angular response should be broader at lower energies, since wide-angle Compton scattering and multiple electron scattering are more prevalent at lower energies. This effect is caused by the restriction set by the Čerenkov threshold on the permissible Compton scattering angles for a given incident gamma ray energy. Figure 2 shows that electrons of a given energy are produced by Compton scattering at larger angles by higher energy gamma rays. Electrons Compton scattered by gamma rays with energies only slightly above the Čerenkov threshold for the gas inside the detector will have energies greater than this threshold only if the Compton scattering angles are small. Higher energy incident gamma rays can Compton scatter electrons at larger angles and still give the electrons enough energy to Čerenkov radiate. Thus for a given Čerenkov threshold energy the directions of incident gamma rays and their Compton scattered electrons will be better correlated for lower energy gamma rays. This correlation will be degraded by increased multiple scattering at lower energies, but in some instances (e.g., the 20 and 30 MeV curves in figure 15) this does not compensate for the first effect. The increased correlation at lower energies unfortunately cannot be used to improve the sensitivity of the detector for point sources, since a necessary consequence of the failure of increasingly large fractions of Compton scattered electrons to Čerenkov radiate is decreased detection efficiencies for gamma ray energies approaching the Čerenkov threshold energy, offsetting the gain in sensitivity from the increased angular correlation.

Reproduced with permission of the copyright owner. Further reproduction prohibited without permission.

Integral Efficiency

The calculated efficiencies $\varepsilon(E)$ are for gamma rays of specific energies. The detector, on the other hand, detects all gamma rays with higher than a certain threshold energy — so an "integral efficiency" is necessary to describe the detector's response to an incident gamma ray spectrum. If $I_\gamma(E)$ is the gamma ray intensity spectrum being observed, then we can define an effective integral efficiency

$$\varepsilon_{eff}(> E_\gamma) = \frac{\int_{E_\gamma}^{\infty} \varepsilon(E) I_\gamma(E)\, dE}{\int_{E_\gamma}^{\infty} I_\gamma(E)\, dE} \qquad (7)$$

$\varepsilon_{eff}(> E)$ depends on the spectrum being observed; since $\varepsilon(E)$ increases at higher energies, $\varepsilon_{eff}(> E)$ at any energy will decrease for steeper spectra. Figure 16 shows the integral efficiency of the detector (with propane gas at 1 atm.) vs. energy, calculated for spectral indices 1.1,1.5 [atmospheric background (Fichtel, et al., 1969)], and 2.1 (extrapolation of the hard X-ray spectrum of the Crab nebula). This integral efficiency, it should be noted, is non-zero even for E_γ below the Čerenkov threshold, since it includes the detection of many gamma rays above this threshold. In carbon, which is the main constituent of the polystyrene scintillator, electron shielding is effectively complete for $E_\gamma >> 137 m_0 c^2 Z^{-1/3} = 38.6$ MeV, so the pair production cross section and hence the detector efficiency are constant at high energies.

Reproduced with permission of the copyright owner. Further reproduction prohibited without permission.

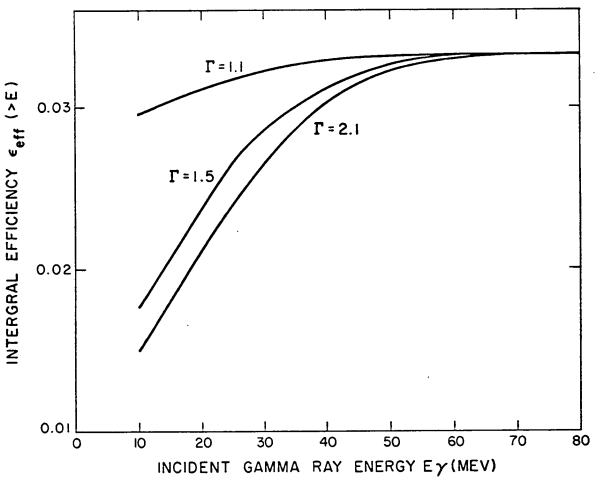

Figure 16

Integral Efficiency vs. Incident Gamma Ray Threshold Energy for Different Incident Gamma Ray Spectral Indices (Detector Filled with Propane at 1 Atm.)

Reproduced with permission of the copyright owner. Further reproduction prohibited without permission.

Corrections to Monte Carlo Results

The Monte Carlo program did not simulate the use of the 8" × 8" scintillator shield (A2) placed above the RCA 4522 to veto electrons passing through the tube face. This would eliminate a fraction of gamma ray events equal to the ratio of the A2 scintillator to the cross-sectional area of the cannister,9.6%. For a gamma ray to be detected, the Čerenkov light circle of a gamma ray-produced electron must intersect the 4.5"-diameter RCA 4522 photocathode, rather than the 5"-outer diameter tube face simulated in the Monte Carlo program. For the gas pressures at which the detector will be operated, the size of the Čerenkov light circle at the focal plane of the mirror is small compared to the photocathode. This reduces the calculated efficiencies by $(4.5/5)^2 = 0.81$. Because of these two effects not considered in the Monte Carlo simulation the calculated efficiencies plotted in figures 14,15,16, and 18 should all be reduced by $0.90 \times 0.81 = 0.73$.

Reproduced with permission of the copyright owner. Further reproduction prohibited without permission.

Energy Discrimination

Gamma rays with $E_\gamma > 2(E_T + m_0c^2)$, where E_T is the Čerenkov threshold energy, can pair-produce two Čerenkov radiating electrons, giving pulses in the RCA 4522 large enough to be distinguished by pulse height analysis from single-electron pulses. Since pair production becomes increasingly dominant over Compton scattering at high ray energies (figure 1), a hard gamma ray spectrum will produce a higher percentage of two-electron events than a soft spectrum; thus the relative number of large pulses among the detected gamma ray events will give some spectral information about the source. Table 2 shows for various gamma ray energies the percentage of gamma rays pair producing and Compton scattering and the fraction $t_2(E)$ of detected events giving two light-producing electrons. For a power law gamma ray spectrum with differential spectral index Γ, the total fraction of detected events with two light-producing electrons for a given threshold energy E_γ is

$$T_2(>E_\gamma) = \frac{\int_{E_\gamma}^{\infty} \varepsilon(E)\, t_2(E)\, E^{-\Gamma}\, dE}{\int_{E_\gamma}^{\infty} \varepsilon(E)\, E^{-\Gamma}\, dE} . \qquad (8)$$

Figure 17 is a plot of T_2 vs. Γ with $E_\gamma = 10.7$ MeV, the Čerenkov threshold of electrons in propane at 1 atm. If the four-channel pulse height analyzer is set to accept only two-electron pulses in its highest channel, it should be possible to get at least an estimate of the spectral index of the observed sources. If the source has a much steeper spectrum than the background, eliminating all the pulses in the highest channel will improve the signal-to-noice ratio, increasing the sensitivity of the detector by a factor $[(1-T_s)/(1-T_b)]^{1/2}$, where T_s and T_b are the

Reproduced with permission of the copyright owner. Further reproduction prohibited without permission.

Gamma Ray Energy (MeV)	Compton Scattering	Pair Production	Two-Electron Events
30	.45	.55	0
50	.31	.69	0.19
100	.20	.80	0.51

Table 2

Monte Carlo Results Showing for Various Incident Gamma Ray Energies the Relative Fractions of Compton Scattering and Pair Production Interactions and the Fraction of Detected Events Giving Čerenkov Light Levels Corresponding to Two Čerenkov-Radiating Electrons.

Reproduced with permission of the copyright owner. Further reproduction prohibited without permission.

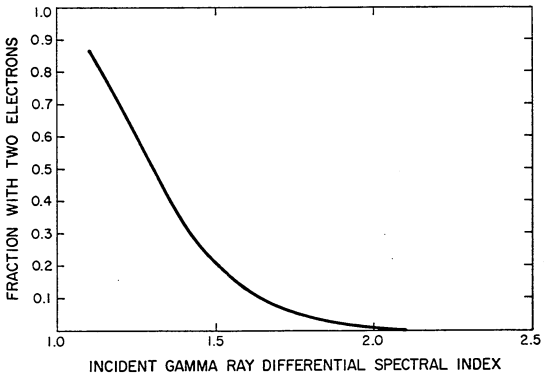

Figure 17

Fraction of Detected Gamma Ray Events Producing Two Light-Producing Electrons vs. Gamma Ray Differential Spectral Index (Detector Filled with Propane at 1 Atm.)

Reproduced with permission of the copyright owner. Further reproduction prohibited without permission.

fractions of detected events from the source and background, respectively, giving two-electron pulses.

Energy Threshold

As figure 16 shows, the detector has no sharp energy cutoff, so there is a certain ambiguity in the energy for which an integral flux measurement is reported.

If a detector with energy response $\varepsilon(E)$ observes a source with differential spectral index Γ, the integral flux for energies $> E_\gamma$ is calculated from the observed count rate by

$$F(> E_\gamma) = \frac{\text{count rate}}{\varepsilon(> E_\gamma)} = \frac{\text{count rate} \times E_\gamma^{-(\Gamma-1)}}{(\Gamma-1)\int_{E_\gamma}^{\infty} \varepsilon(E) E^{-\Gamma}\, dE} \quad . \tag{9}$$

$\varepsilon(> E_\gamma)$ increases with increasing E_γ, so using a higher E_γ in reporting a measurement will result in reporting a smaller flux; but for power law spectra, the flux is smaller at higher energies, so the error introduced by the choice of E_γ will be a second order effect.

A rational choice of the reported energy threshold should consider both the shapes of the integral detector efficiency curves (figure 16) and the most probable gamma ray interaction energies for various incident spectral indices (figure 18). Figure 18 shows the product of the detector efficiency and an incident power law flux for different gamma ray energies. This product shows the relative number of gamma rays detected at different energies. The maxima of the curves for the different spectral indices indicate the most probable gamma ray detection energy — i.e., when the detector with a given Čerenkov threshold registers a gamma ray event,

Reproduced with permission of the copyright owner. Further reproduction prohibited without permission.

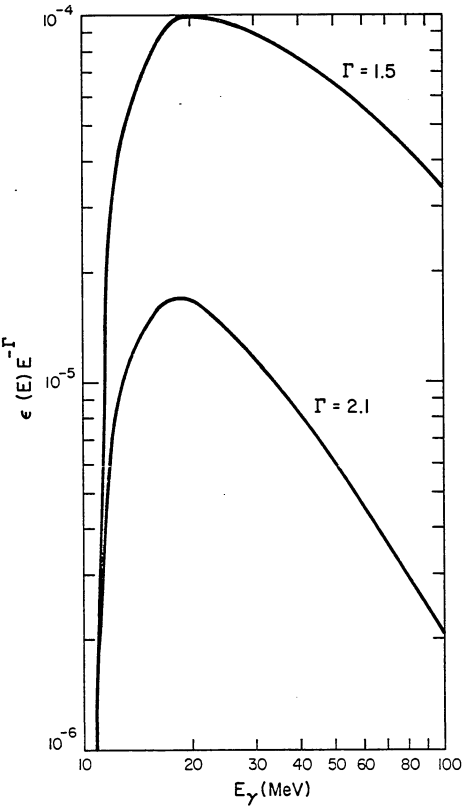

Figure 18

Folding of Detector Efficiency and Incident Power Law Gamma Ray Spectra for Two Incident Gamma Ray Spectral Indices (Detector Filled with Propane at 1 Atm.)

Reproduced with permission of the copyright owner. Further reproduction prohibited without permission.

the gamma ray energy most likely to have caused the event is that corresponding to the maximum of the curve in figure 18. The spectral index of a gamma ray source is not necessarily known, but figure 18 shows that the energy at which $\varepsilon(E)E^{-\Gamma}$ is a maximum is fairly insensitive to Γ. For spectral indices from 1.5 to 2.1, this energy is between 17 and 20 MeV. For the same range of spectral indices, the half-maximum efficiencies in the curves in figure 16 occur at energies between 10 and 15 MeV. Considering these two criteria, we chose to report our integral flux measurements or upper limits above a threshold energy of 15 MeV.

The largest error in the reported flux comes from the value assumed for the incident gamma ray spectral index, which appears in the denominator of equation 9. Measurements with a single detector of $I_\gamma(> E_\gamma)$ for several values of E_γ will be able to determine the spectral index, allowing a self-consistent determination of the flux without reliance on previous measurements.

VI. Predicted Noise, False Events, and Charged Particle Rejection

For a balloon-borne gamma ray experiment, the background noise from atmospheric gamma rays, a function of the altitude and geomagnetic location of the balloon and the angular response of the detector, is a limiting factor for the signal-to-noise ratio of the experiment; to achieve maximum sensitivity, all other sources of noise must be small compared to the atmospheric gamma ray background rate.

The downcoming atmospheric gamma ray background at 3.5 mb over Palestine, Texas is (Fichtel, et al., 1969)

$$I(> E) = 0.03\ E(\text{MeV})^{-.5}\ \gamma\ \text{cm}^{-2}\text{sec}^{-1}\text{sr}^{-1}\ .$$

Reproduced with permission of the copyright owner. Further reproduction prohibited without permission.

The threshold energy for Čerenkov light production by electrons in propane at STP is 10.7 MeV. Monte Carlo calculations, discussed below, indicate an effective efficiency for $E_\gamma > 10$ MeV of $\varepsilon \approx 0.02$ with an acceptance half-angle of $\sim 6°$. Thus for an area of 1.45×10^3 cm^2, the expected gamma ray background count rate is

$$B_\gamma = I\varepsilon A\Omega \approx 10^{-2} \text{ sec}^{-1} = 0.6 \text{ min}^{-1} . \quad (10)$$

The problem of background gamma rays generated locally by cosmic ray interactions in the detector was considered by Albats, et al. (1970). They found a background flux above 50 MeV of 2.9×10^{-5} γ cm^{-2}sec^{-1}sr^{-1} and then repeated the measurements with a magnesium block above the veto shield of their spark chamber to simulate the pressure of local detector material. The additional background was $\sim 10^{-7}$ γ cm^{-2}sec^{-1}sr^{-1}gm(Mg)$^{-1}$. Because of its proximity to the converter-scintillator, the aluminum cap on the shell of our detector will be the most serious source of local background production. The results for Mg should be roughly valid for Al and indicate that the cap (3.91×10^3 gm) should produce a background flux of $\sim 3.9 \times 10^{-4}$ γ cm^{-2}sec^{-1}sr^{-1}, more than an order of magnitude below the atmospheric gamma ray background flux.

The background singles noise rate in the CS photomultipliers (not necessarily in coincidence with the 4522) caused by upward-moving electrons stopping in the converter-scintillator (not triggering the anti-shield) was calculated using the electron albedo measurements of Verma (1967) modified as suggested by Israel (1969):

Splash Albedo: $dJ/dE \approx 2.2\ E^{-1.3}$ particles m^{-2}sec^{-1}sr^{-1}MeV^{-1} .

(10 MeV $\leq E \leq$ 1100 MeV)

Reproduced with permission of the copyright owner. Further reproduction prohibited without permission.

The geometrical factor of the converter-scintillator (over only one hemisphere, since electrons coming from overhead will be rejected by the anticoincidence shield) is 1.2×10^4 $cm^2 sr$. Since low energy electrons lose $\sim$ 1.8 MeV cm^{-1} in polystyrene, electrons between 1 MeV and 10 MeV may not penetrate the 1" thick converter-scintillator to produce an anti-coincidence pulse. Electrons below 1 MeV will not penetrate the aluminum cannister. From extrapolation of Verma's results, the expected singles noise count rate in the scintillator from albedo electrons is $\sim$ 240 sec^{-1}. Protons contribute negligibly to the noise counts. Phototube dark noise in the RCA 6199's has been measured to be $\sim$ 30 sec^{-1}. The mean thickness of the converter to background gamma radiation, integrated over all angles, is 4.75 cm. The linear attenuation coefficient in polystyrene at low-MeV gamma ray energies is $\sim$ 0.04 cm^{-1}, so about 17% of the gamma rays with $E > 1$ MeV will produce noise pulses. This gives a rate of 40 sec^{-1}. Thus, the total random rate in the converter-scintillator is 310 sec^{-1}, with the largest contribution coming from the electron background.

Phototube dark noise in the RCA 4522 was also found to be on the order of 30 sec^{-1}. Background singles pulses will be caused by the Čerenkov light of charged particles traversing the face of the tube and by particles directly knocking electrons from the photocathode. The expected noise rate from these causes is $\sim$ 50 sec^{-1}, using the splash and reentrant albedo measurements extrapolated to 1 MeV. In addition, approximately 65 gamma rays sec^{-1} will cross the tube face, but < 10 sec^{-1} will produce electrons. Thus, the total noise rate in the 4522 is expected to be 90 counts sec^{-1}, with about one third coming from the dark current.

With 310 counts sec^{-1} from the converter-scintillator and 90 counts sec^{-1} from the 4522, and with discriminator pulse widths set at 6 nsec,

Reproduced with permission of the copyright owner. Further reproduction prohibited without permission.

the random background count rate at balloon float altitude will be:

$$B_{random} = 2\tau R_1 R_2 \simeq 0.02 \text{ min}^{-1} . \quad (11)$$

These random, "false" events will increase the background by only $\sim$ 3%. It was not possible to lower the random count rate by reducing the high voltage on the photomultipliers, lowering the singles noise rates, because this caused a decrease in tube sensitivity which lowered the counting rate for real particles (as measured with sea level muons in the laboratory). A detection logic system requiring a triple coincidence would reduce random counts to near-zero. One possible method to accomplish this would be to replace the 5" RCA 4522 with a cluster of three 2" photomultipliers at the mirror focus, demanding a two-out-of-three voter coincidence, the output of which could then be put into coincidence with the converter-scintillator pulse. The electronics for this were not available when the experiment was constructed, but this is a possible improvement for future flights.

Any charged particles which do not trigger the anticoincidence counter and have energy greater than the Čerenkov production threshold will be recorded as gamma rays. In propane at STP, $\gamma_{threshold} = 21$. The reentrant electron albedo flux greater than 10.7 MeV is 0.019 electrons cm^{-2} $sec^{-1}sr^{-1}$. The calculated solid angle-area of the detector is 42.3 cm^2sr, giving an electron count rate, assuming 100% detection efficiency and with no anticoincidence, of 0.8 sec^{-1}. The reentrant albedo flux of protons with energy greater than 19.7 GeV is negligible compared to the electron flux.

The cosmic ray proton flux above this threshold is 2×10^{-2} particles $cm^{-2}sec^{-1}sr^{-1}$ (Meyer, 1970) giving a count rate of 0.8 sec^{-1}. The primary electron flux above the rigidity cutoff (4.6 GeV/c over Palestine, Texas) is < 10% of the proton flux above 20 GeV. Thus, the expected charged

Reproduced with permission of the copyright owner. Further reproduction prohibited without permission.

particle count rate at float altitude with no anticoincidence is 1.6 counts sec^{-1} (assuming 100% detection efficiency for charged particles). An efficiency of 0.1% in the anticoincidence counter will give a count rate of 0.1 min^{-1}, which is small compared to the atmospheric gamma ray background rate.

Reproduced with permission of the copyright owner. Further reproduction prohibited without permission.

TESTING AND CALIBRATION

Reproduced with permission of the copyright owner. Further reproduction prohibited without permission.

TESTING AND CALIBRATION

I. Laboratory Testing

After the detector was assembled it was necessary to make sure that 1) the timing circuitry was working correctly, 2) the random coincidence rate was no higher than anticipated, 3) the detector was responding to the Čerenkov light of the detected particles rather than some other effect, and 4) the detector had the proper response in the laboratory to sea level cosmic ray muons.

Coincidence Plateau

The adjustable discriminator outputs (5-15 nsec) were set at minimum width to reduce the random coincidence rate. Figure 19 shows a timing plateau curve for coincidence between the converter-scintillator and the RCA 4522 Čerenkov photomultipliers, with the A2 tube in anticoincidence to eliminate counting muons traversing the 4522 tube face. The half-width is 6 nsec, which is consistent with the discriminator output width. Timing curves like this were used to determine the proper lengths of delay lines to put into the circuits.

Random Coincidence Rate

The random coincidence rate at a balloon float altitude of 3.5 mb was calculated using the photomultiplier tube singles noise rates expected at this altitude, which were largely caused by charged particles. Only 1/10 of the CS noise counts and 1/3 of the 4522 noise counts were

Reproduced with permission of the copyright owner. Further reproduction prohibited without permission.

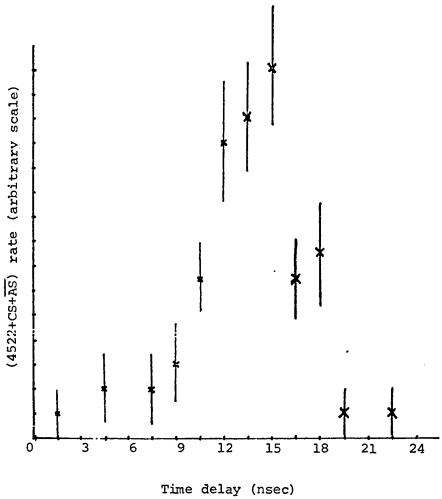

Figure 19

Coincidence timing plateau between RCA 4522 and converter-scintillator photomultipliers

Reproduced with permission of the copyright owner. Further reproduction prohibited without permission.

estimated to come from dark noise, which will be the only important source of noise at sea level. The change with altitude in singles rates for the photomultipliers is discussed below in the section on the balloon flight results. The expected random coincidence rate when only the intrinsic tube noise is considered is $\sim$ 1 count day^{-1}. This is consistent with measurements taken in the laboratory.

Shutter and A2 Shield

To check that the pulses from the RCA 4522 were really caused by Čerenkov radiation, a shutter was installed which could cover and uncover the tube face during laboratory testing. Any signals not caused by the light in the gas would be unaffected by closing the shutter, whereas Čerenkov light reflected from the mirror would be blocked from entering the tube. Preliminary tests showed that despite the timing circuitry some muons crossing the tube face were causing coincidences between the 4522 and the CS tubes even with the shutter closed.

If gamma rays are detected by the direct interaction of their secondary electrons with the 4522 phototube face rather than by the detection of the Čerenkov light emitted by these electrons, the acceptance angle will be the solid angle subtended at the 4522 tube face by the converter-scintillator, which is six times as large as the proper acceptance angle determined by the detector's optical geometry and the characteristics of Čerenkov radiation in the detector gas. This was the reason for installing the A2 shield. When the A2 photomultiplier was put into anti-coincidence with the 4522 and the CS tubes, counts with the shutter closed were reduced to the random coincidence rate. The shutter was removed before the balloon flight.

Reproduced with permission of the copyright owner. Further reproduction prohibited without permission.

Detector Count Rate vs. Čerenkov Threshold Energy.

A further test that the 4522 photomultiplier tube was really detecting Čerenkov light and that the detector was responding properly to charged particles was to measure the sea level detector count rate vs. the Čerenkov threshold energy, which was varied both by changing the air pressure inside the detector and by replacing the air with propane. These measurements are plotted on a log-log graph in figure 20 along with the sea-level integral muon spectrum (Sandström, 1965).

Formula 4 shows the dependence of the Čerenkov threshold index on the refractive index of the gas and hence on the gas pressure. Jelley (1958) also shows that, for particles with $\beta = 1$, the rate of emission of Čerenkov light per unit path length is proportional to the refractive index of the gas. Knowing a particle's pathlength in the gas, the refractive index, the photocathode efficiency and wavelength response of the photomultiplier collecting the Čerenkov light, one can calculate the number of photoelectrons ϕ_0 expected on the average from a particle with $\beta = 1$. ($\phi_0 = 23$ for the present detector filled with air at 1 atmosphere, which gives a threshold energy for muons of 4.3 GeV.) With Poisson statistics, the probability of not detecting an event, when the external circuitry accepts single photoelectron pulses, is $\exp(-\phi_0)$, which is negligible for $\phi_0 = 23$. For particle energies near E_T, however, the light output markedly decreases, and there is a non-negligible probability of not detecting a particle with energy only slightly above the threshold. Damle (1968) discusses this problem at length. The number of photoelectrons (ϕ) produced when $E = E_T$ compared to the number (ϕ_0) produced when $E >> E_T$ is given by

Reproduced with permission of the copyright owner. Further reproduction prohibited without permission.

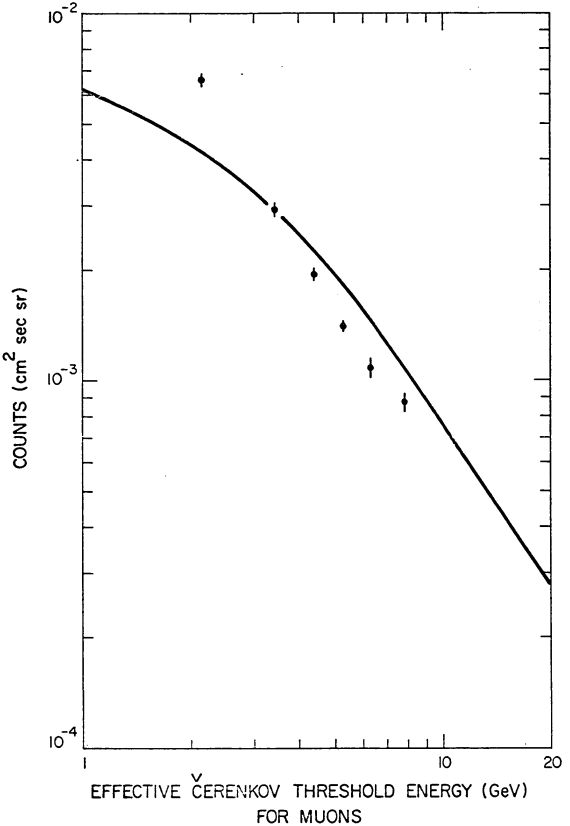

Figure 20

Points. Sea Level Count Rates vs. Effective Cerenkov Threshold Energy for Muons

Line: Sea-Level Integral Muon Spectrum (Sandström, 1965)

Reproduced with permission of the copyright owner. Further reproduction prohibited without permission.

$$\frac{\phi}{\phi_0} = 1 - E_T^2/E^2 \ . \qquad (12)$$

Since the efficiency for detecting muons at the single photoelectron level is

$$\varepsilon(E) = 1 - \exp[-\phi(E)] \ , \qquad (13)$$

the efficiency near the threshold may be expressed in terms of the particle energy:

$$\varepsilon(E) = 1 - \exp[-\phi_0(1 - E_T^2/E^2)] \ . \qquad (14)$$

Using formula 14 an effective energy threshold E_{eff} can be defined at which $\varepsilon(E_{eff}) = \frac{1}{2}\,\varepsilon(E >> E_T)$. Damle gives this as

$$E_{eff} = E_T\left[\frac{1}{1 - 0.69/\phi_0}\right]^{1/2} \ . \qquad (15)$$

This effective energy is plotted in figure 20 rather than the actual Čerenkov threshold energy corresponding to each different gas pressure. (This correction assumes the 20% photocathode efficiency reported by the manufacturers for the RCA 4522 and is thus somewhat uncertain. For example, if the efficiency were 15% rather than 20%, the data point at 7.8 GeV would be shifted to 7.95 GeV.)

Muon trajectories through the detector are essentially straight line continuations of their paths through the atmosphere, since no production by gamma rays is involved and the muons suffer little multiple scattering. The solid angle of acceptance calculated by the Monte Carlo program for gamma ray detection is therefore not valid for muons, whose acceptance angle will be determined almost entirely by the optical

Reproduced with permission of the copyright owner. Further reproduction prohibited without permission.

geometry of the detector. In converting the observed count rates to muon intensities, the acceptance angle was assumed to be the angle subtended by the photocathode at a distance of one focal length from the mirror. This angle should be a good estimate for muons crossing the converter-scintillator near the central axis of the detector but probably is an overestimate when particles are near the outer edge, since then many particles nominally within the optical acceptance angle will hit the cannister walls before producing enough light to be detected. The correction for this effect would shift the whole curve up uniformly at all energies. It has not been included in figure 20 because its exact magnitude is unknown. Rough geometrical calculations indicate its approximate magnitude is between 1.2 and 1.5, which would bring the observed points up to the plotted curve, indicating that the detector is recording muons with 100% efficiency. This geometrical uncertainty and the uncertainty in determining E_{eff} make it impossible to make any more rigorous a determination of the efficiency than $80\% < \varepsilon_{\mu} \leq 100\%$. The slope of the observed points, however, is independent of these corrections and can be compared to the slope of the integral muon spectrum to see if the detector is functioning properly.

For the higher muon energies, the slope of the observed points in figure 20 agrees with what would be expected for proper operation of the detector in observing the integral atmospheric muon spectrum. At lower muon energies, a definite excess was observed in the count rate, caused almost certainly by the soft component of sea-level cosmic radiation (Wolfendale, 1963; Leprince-Ringuet, 1950). This soft component is composed of slow muons and secondary electrons generated by energetic muons in collisions and by bremsstrahlung-initiated electromagnetic cascades.

Reproduced with permission of the copyright owner. Further reproduction prohibited without permission.

The spectrum of the soft component will be one power steeper than the hard muon spectrum plotted in figure 20 since most of the secondary electrons are produced by low- rather than high-energy muons, which lose most of their energy by ionization (Leprince-Ringuet, 1950). This soft component, composing ~ 25% of the sea-level cosmic ray spectrum, is generally considered "noise" for muon measurements and can be eliminated by shielding with 6" of lead. The behavior of the detector was shown to be correct for the higher energy muons. Since this was the object of the measurements rather than an actual determination of the muon spectrum, no attempt was made to shield the detector, which would have been extremely difficult with the laboratory setup in which the present sea-level measurements were obtained.

II. LINAC Calibration

Introduction

The efficiency of the detector, $\varepsilon(E_\gamma,\theta)$, was calculated by the Monte Carlo simulation described above, but before the detector is used to measure celestial gamma rays this calculation must be checked experimentally by observing the response of the detector in a gamma ray beam of known intensity and direction. This can best be done with a particle accelerator, producing gamma rays by interactions of the accelerated charged particles. In an ideal calibration of a gamma ray telescope, a monochromatic gamma ray beam should be used to measure the efficiency $\varepsilon(E_\gamma,\theta)$ for many values of E_γ and θ, the incident gamma ray energy and angle, respectively. The angular response of the detector is determined by the gamma

Reproduced with permission of the copyright owner. Further reproduction prohibited without permission.

ray conversion process, electron multiple scattering, and the geometry of the detector. Once a gamma ray has converted, the telescope is mainly an electron detector — and much can be learned about multiple scattering and detector geometry by examining the angular response of the detector in an electron beam. The efficiency of gamma ray production in the Naval Research Laboratory LINAC electron beam, where the calibration was carried out, is small ($\sim 10^{-2}$) usable gamma rays per electron) so the time required for a complete calibration with gamma rays is prohibitive. Doing as much of the calibration as possible with electrons gives a great saving in time. At high energies, both conversion probabilities and electron production angles are well-known, the latter being small. High energy (50-60 MeV) electrons can be used to check the optical acceptance geometry of the detector. The high energy results can be extrapolated to lower energies using theory and Monte-Carlo calculations. The predicted response to gamma rays can then be checked against a few actual LINAC beam runs with gamma rays.

Since a major advantage of the present gamma ray detector is its ability to detect gamma rays at energies as low as 15 MeV, the most important parts of the Monte Carlo calculations to test experimentally are the low energy results. Unfortunately, the LINAC was not working at maximum energy resolution and it was impossible to get a good gamma ray beam at 30 MeV, which we had originally planned on. We decided to spend most of our beam time making measurements with electrons and to make only one gamma ray calibration, at 50 MeV. A future calibration will be carried out at lower gamma ray energies.

Reproduced with permission of the copyright owner. Further reproduction prohibited without permission.

Experimental Setup

Figure 21 shows schematic diagrams of the beam-detector layout in various test configurations. The LINAC produced a 60 MeV electron beam pulsed at 360 Hz with a variable number of electrons in each pulse. A vacuum breakdown during the previous week forced the removal of one of the slit collimators, reducing the nominal ± .5% electron energy spread to ± 2.5%.

Gamma rays are produced by electron bremsstrahlung in a disc of lead foil .040" thick placed between the beam tube and the beam counter scintillator, as shown in figure 21a. Most electrons either do not bremsstrahlung in the lead or produce sufficiently low-energy gamma rays that they still emerge from the disc and trigger the beam counter. Only when an electron produces a gamma ray with nearly its own original energy does it lose enough energy that it is likely to stop in the lead or be backscattered away from the beam counter; the gamma rays produced by these electrons are used for calibration.

Each time the electron beam is pulsed in the LINAC, a timing signal is generated at the beam control console and is sent to the experimenters' electronics panel, where it can be used in coincidence timing circuits to ensure that all measurements are taken only when the beam is on. Possible gamma ray events are indicated by a signal from the beam control console, indicating a beam pulse, unaccompanied by a count from the beam counter scintillator. It is essential that only one electron be in the beam at a time, since if there are two electrons and one produces a gamma ray, the other will trigger the beam counter, negating the event. The probability of both producing gamma rays is negligible, and few gamma ray events will be seen. For this reason, beam rates were kept around 200 electrons

Reproduced with permission of the copyright owner. Further reproduction prohibited without permission.

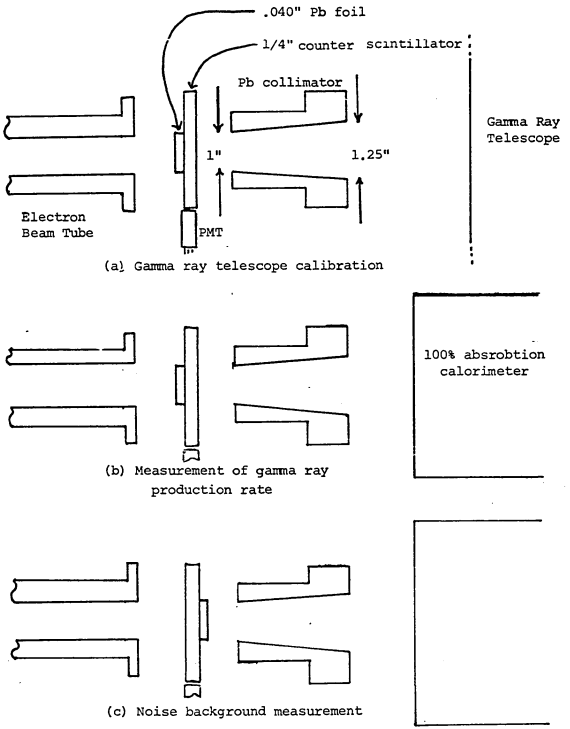

Figure 21

Various Beam-Detector Configurations

Reproduced with permission of the copyright owner. Further reproduction prohibited without permission.

sec^{-1}. The experience of the gamma ray astronomy group at NRL with the LINAC showed this rate to be near-optimum. Higher rates reduce the number of detected gamma rays because of the increasing number of two-electron pulses,and lower rates intrinsically produce fewer gamma rays. Each pulse is relatively independent of the other pulses and the electrons are fairly evenly distributed among the pulses, so Poisson statistics should describe the electron distribution among the pulses. With 360 pulses sec^{-1} and 200 electrons sec^{-1}, the probability of a pulse having two or more electrons is only 0.11. The pulse distribution statistics cannot be exactly Poisson, since if they were, 360 electrons sec^{-1} would give the maximum single electron (and hence detected gamma ray) rate instead of the experimentally determined 200 electrons sec^{-1}.

Some electrons may fail to trigger the beam counter without producing gamma rays, and an accurate detector calibration requires a precise knowledge of the number of gamma rays hitting the detector. For this reason, the beam is measured by a 100% efficient lead-glass gamma ray calorimeter prior to the calibration (as shown in figure 21b). The ratio of (console + $\overline{\text{counter}}$ + calorimater) (i.e., beam console pulses unaccompanied by beam counter pulses and in coincidence with the calorimeter pulses) to (console + $\overline{\text{counter}}$) shows the fraction of "indicated" gamma rays which are truly gamma rays. A noise background measurement is obtained by using the calorimeter in the same configuration only with the lead on the opposite side of the beam counter from the beam tube (figure 21c). The background is subtracted from all other measurements before any ratios are calculated. The fraction of "indicated" gamma ray events detected by the telescope must be divided by the fraction detected by the calorimeter to give the true efficiency of the detector.

Reproduced with permission of the copyright owner. Further reproduction prohibited without permission.

The absence of the collimation slit produced a 5% uncertainty in the electron energy. The statistical processes involved in electron energy loss in the lead spread out the low energy gamma ray cutoff (gamma ray energy below which the radiating electrons are left with enough energy to escape from the lead and trigger the beam counter). Dr. G. Share of NRL (Private Communication) estimates from his calculations and past measurements that the spectrum should have approximately the form shown in figure 22: peaked at ~ 50 MeV with a slight skew towards the higher energies and a low energy tail. This rather large energy spread would be even worse if the calibration were carried out at lower gamma ray energies, since statistical fluctuations in electron energy loss in the lead are greater at lower energies. Also, the efficiency of gamma ray production is lower at lower energies; so for a fixed time on the LINAC, fewer gamma rays would be produced, increasing the statistical uncertainty of the detector efficiency calibration. These drawbacks, plus the likelihood of a future low energy calibration with a high-resolution positron-produced gamma ray beam that the NRL group is working on, made us decide to make only one on-axis efficiency calibration of the detector, with 40-60 MeV gamma rays, and to use electrons for the other measurements.

Electron Results

A gamma ray conversion will occur, on the average, in the middle of the 1" thick converter-scintillator, which is where a collimated electron beam should originate to simulate most closely real gamma ray events. Before getting there, however, the electrons must pass through the 1/4" beam counter scintillator, the 1" anticoincidence scintillator, 1/2" of

Reproduced with permission of the copyright owner. Further reproduction prohibited without permission.

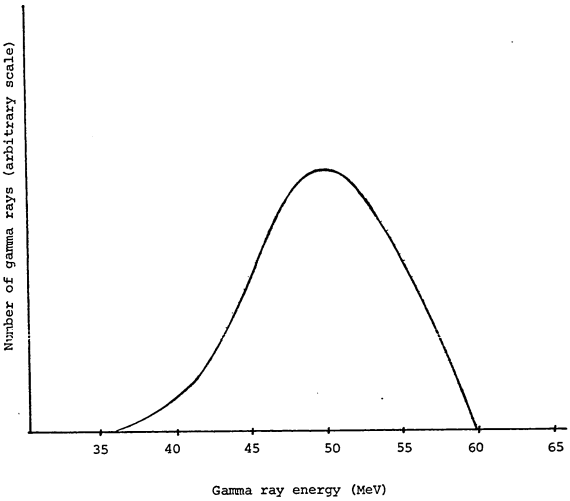

Figure 22

Energy distribution of gamma rays used in LINAC calibration

Reproduced with permission of the copyright owner. Further reproduction prohibited without permission.

the converter scintillator, and the 1/8" aluminum detector cap. Thus the electron beam used for making angular measurements unfortunately has a non-zero angular spread.

When RMS scattering angles in the various layers of polystyrene and aluminum are combined the same way as standard deviations in a Gaussian distribution

$$\langle \theta^2 \rangle = \sum_{i=1}^{n} \langle \theta_i^2 \rangle \qquad (16)$$

the mean scattering angle of an electron turns out to be 7.5°. This must be considered in determining the detector's angular response from the electron beam measurements.

Efficiency vs. Horizontal Position:

Figure 23 shows the efficiency of the detector in detecting electrons entering the detector parallel to but removed at various distances horizontally from the detector axis. The response is what is expected, with a sharp falloff outside the converter-scintillator and a falloff on-axis because of the 8" × 8" guard scintillator (A2). The on-axis efficiency is non-zero because the incident electrons have an angular spread (7.5°) and some miss the guard scintillator while still emitting enough Čerenkov light to cause a signal in the 4522 photomultiplier.

Efficiency vs. Off-Axis Angle and Interpretation for Gamma Ray Detection:

Figure 24 shows the efficiency of the detector in detecting 60 MeV electrons vs. the off-axis electron angle. The apparent half-angle (HWHM) from this graph is 9°, but this is a combination of the real angular

Reproduced with permission of the copyright owner. Further reproduction prohibited without permission.

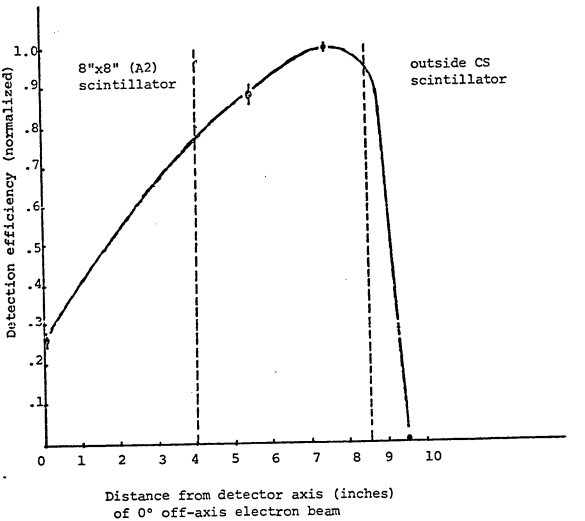

Figure 23

Efficiency of Detector for 60 MeV on-axis electrons
vs. horizontal distance from axis

Reproduced with permission of the copyright owner. Further reproduction prohibited without permission.

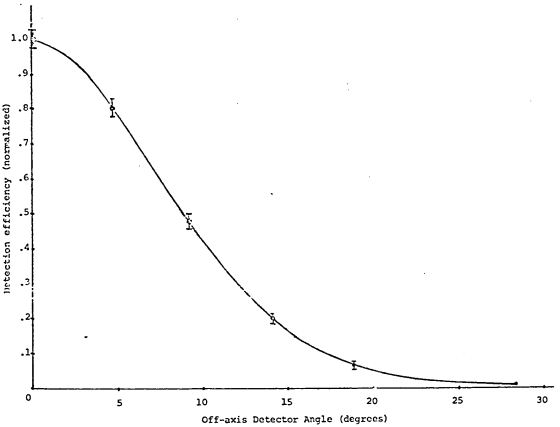

Figure 24

Efficiency of gamma ray detector in detecting 60 MeV electrons vs. off-axis angle

Reproduced with permission of the copyright owner. Further reproduction prohibited without permission.

response of the detector and the intrinsic angular spread of the beam (7.5°). Using formula 16 to "decombine" these two angles gives $\theta_{1/2 \text{ detector}} = 4.9°$. Using figure 3 to get the mean Compton scattering electron angle and $\theta_{pp} = m_0c^2/E_\gamma$ to estimate the pair production opening angle, an energy-dependent mean "interaction angle" can be calculated as the mean of the pair production and Compton scattering results weighted by the relative probability of each type of interaction at a given energy. This is only 0.5° at 60 MeV, so the half-angle response of the detector to gamma rays with $E_\gamma = 60$ MeV will be $\sim 4.9°$, representing almost entirely multiple scattering and detector geometry. To extrapolate the 60 MeV results to lower energies, we assume that all the angular spread comes from multiple scattering rather than detector geometry and, using formula 3, derive

$$\theta_{1/2}(E) = \theta_{1/2}(60)_{\text{measured}} \times \frac{60}{E} \quad . \tag{17}$$

This electron scattering angle is folded together with the mean interaction angle to give the mean half-angles for the detector response at lower energies. The results are plotted in figure 25. These are worst-case calculations, since if more of the angular spread at 60 MeV comes from detector geometry and less from multiple scattering, then the increase in the angular spread at lower energies will be less.

At 50 MeV, figure 25 agrees with the Monte-Carlo calculations of the detector half-angle (5°), but at lower energies gives larger half-angles. Besides the worst-case nature of the present calculation, a reason for the seemingly too small half-angles predicted by the Monte-Carlo simulation has been discussed above in the section on Monte Carlo calculations.

Reproduced with permission of the copyright owner. Further reproduction prohibited without permission.

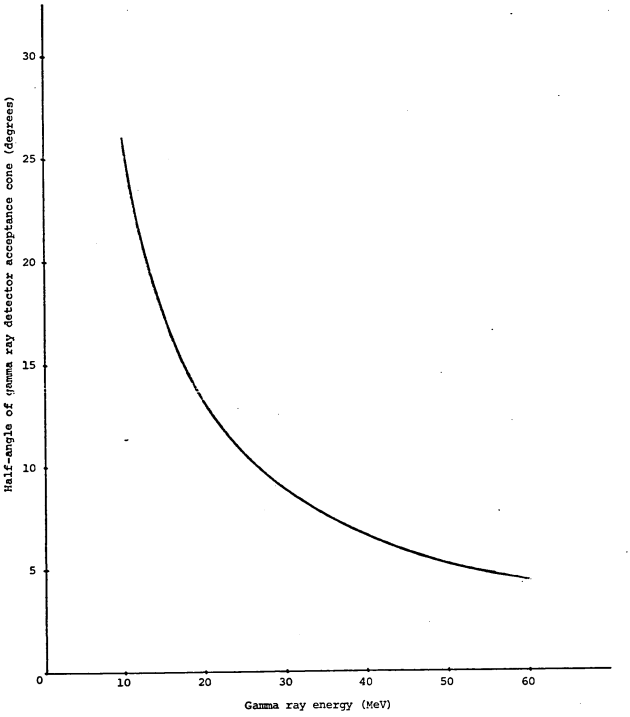

Figure 25

Half-angle of gamma ray detector acceptance cone vs. incident gamma ray energy

Reproduced with permission of the copyright owner. Further reproduction prohibited without permission.

Gamma Ray Results

The intrinsic energy spread of the gamma rays produced by the LINAC has already been discussed. A lead pipe collimated the gamma ray beam (figure 21b) to a 4.8° half-angle. We thus measured not the on-axis efficiency but an average efficiency ε_{ave} for gamma rays from 0° to 4.8° off-axis angle. ε_{ave} can be estimated by:

$$\varepsilon_{ave} \int_{0°}^{4.8°} \sin\theta \, d\theta = \int_{0°}^{4.8°} \varepsilon(\theta) \sin\theta \, d\theta \qquad (18)$$

where $\varepsilon(\theta)$ is the angular response function of the detector, normalized so that $\varepsilon(0°) = 1$. This gives $\varepsilon_{ave} = 0.76$.

The measured gamma ray detection efficiency was 1.4 ± .3%. Divided by ε_{ave} to correct for the angular spread of the incident gamma ray beam, this becomes the equivalent of 1.8 ± .4% efficiency for on-axis gamma rays. 50 MeV gamma rays should be detected with an efficiency of 2.0%, according to the Monte Carlo results modified as desciibed earlier for the actual RCA 4522 photocathode size, for the presence of the A2 scintillator shield, and also for the interaction of ∿ 3% of the incident gamma rays with the anticoincidence shield and the aluminum cannister cap, not considered in the Monte Carlo program. The measured efficiency is within one standard deviation of the calculated efficiency. The large spread in the energy spectrum of the gamma rays used for calibration makes it difficult to compare exactly the calibration results with the calculated efficiency. Still, we shall assume that the calibration value is correct for 50 MeV gamma rays and multiply all modified Monte Carlo efficiency predictions by a factor of 0.9 when translating actual measurements into source strength estimates and upper limits.

Reproduced with permission of the copyright owner. Further reproduction prohibited without permission.

III. Anticoincidence Efficiency

Laboratory Testing

The efficiency of the anticoincidence scintillator in rejecting charged particles was measured using sea-level cosmic rays and two auxiliary 5" x 5" scintillators arranged as shown in figure 26a. The photomultiplier pulses from the anticoincidence shield are fed into the veto input of the EGG C144/N coincidence module. The inefficiency is given by the ratio $(c1 + c2 + \overline{AS})/(c1 + c2)$.

The limitations placed by the outer cannister dimensions on light collection efficiency in the anticoincidence shield have been discussed above. The photomultiplier tubes had to be run at peak voltage (1250 v.) to achieve maximum sensitivity. A voltage divider network equalized the tube count rates with a Co^{60} source in the center of the anti-shield; the noise rates were not equal. The four anticoincidence 6199 photomultiplier signals were originally fed into a passive resistive mixer. If N inputs are mixed in a passive network with impedance matching, as shown in figure 27, the signal voltage coming out is attenuated to $1/N^2$ its source value. The signals were fed into a discriminator with preset threshold, and this severe attenuation in the mixer caused a loss of 1/2 the counts from the photomultipliers. Charged particle rejection efficiency increased as the tube voltages were increased (as high as 1300 v.) and up to two stages of the EGG AN201/N linear amplifier were used; but the rejection efficiency was never better than 85%. A plateau was never reached in the efficiency vs. high voltage curve, indicating that the problem was weak signals coming into the discriminator. When an EGG AN100

Reproduced with permission of the copyright owner. Further reproduction prohibited without permission.

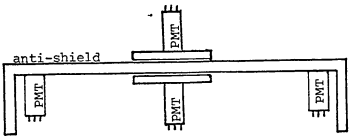

(a)

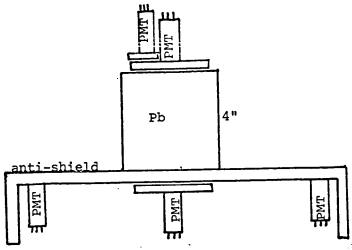

(b)

Figure 26

Scintillator configurations for measuring anticoincidence inefficiency

Reproduced with permission of the copyright owner. Further reproduction prohibited without permission.

N sources with impedance R_1

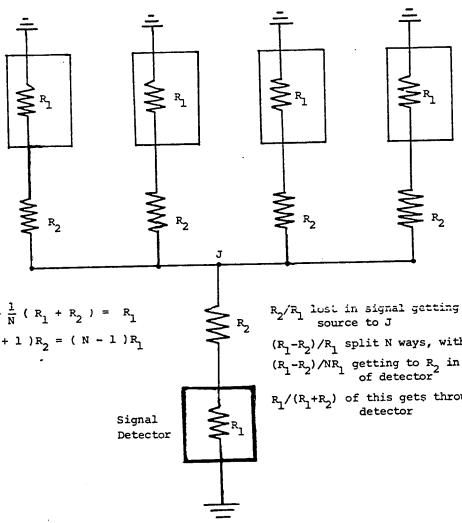

$R_2 + \frac{1}{N}(R_1 + R_2) = R_1$

$(N + 1)R_2 = (N - 1)R_1$

R_2/R_1 lost in signal getting from source to J

$(R_1-R_2)/R_1$ split N ways, with

$(R_1-R_2)/NR_1$ getting to R_2 in front of detector

$R_1/(R_1+R_2)$ of this gets through to detector

Fraction of original signal reaching detector:

$$f = \frac{R_1}{R_1+R_2} \times \frac{R_1-R_2}{NR_1} = \frac{1}{N}\left(\frac{R_1-R_2}{R_1+R_2}\right) = \frac{R_1\left(1 - \frac{N-1}{N+1}\right)}{NR_1\left(1 + \frac{N-1}{N+1}\right)} = \frac{1}{N^2}$$

Figure 27

Passive Mixing of N inputs with Internal Impedance R_1

Reproduced with permission of the copyright owner. Further reproduction prohibited without permission.

active linear signal mixer was substituted for the passive mixer, eliminating resistive losses, the rejection efficiency immediately increased to 98%.

The EGG T140/N discriminator has a dead time equal to its output pulse width; however, a reflection line whose length corresponds to half the discriminator output pulse width was attached to the anticoincidence discriminator output, so that the dead time was "covered" by the reflected veto pulse, giving effectively zero dead time. The zero-crossing discriminators are designed to accept clipped pulses (figure 28a); however, clipping attenuates the anticoincidence pulses, reducing considerably the number of pulses triggering the fixed-threshold discriminator. This was responsible for some of the observed inefficiency. Even without clipping, a photomultiplier pulse has sufficient overshoot to fire the discriminator. Removing the clipping from the anticoincidence pulses decreased the rejection inefficiency to < 1%.

To discover the cause of the remaining inefficiency, the unrejected (i.e., C1 + C2 + $\overline{AS}$) pulses were examined on an oscilloscope. Without clipping, many pulses were extremely wide (figure 28b), so that zero-crossing of the pulse overshoot did not occur until 50-100 nsec after the event (figure 28b), allowing the coincidence to be registered before the veto pulse arrived. To check the possibility that these large pulses were the soft electron component of large air showers rather than single muon pulses, lead shielding was used in a 3-way counter configuration (figure 26b) designed to prevent soft electrons from triggering a coincidence. The rate of large pulses was reduced but was still not zero, so the possible production of large pulses by single charged particles had to be guarded against, since these pulses would not be vetoed. A pulse inverter was

Reproduced with permission of the copyright owner. Further reproduction prohibited without permission.

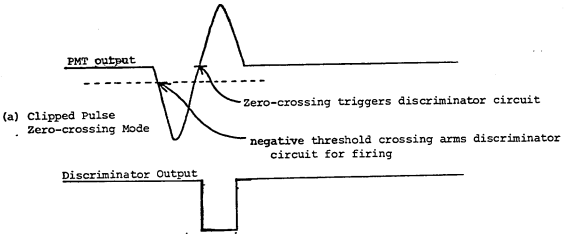

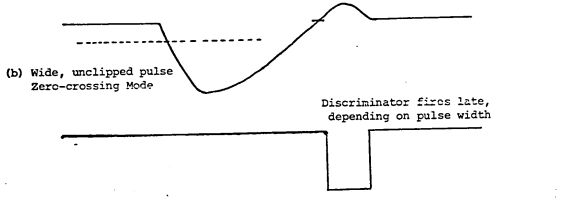

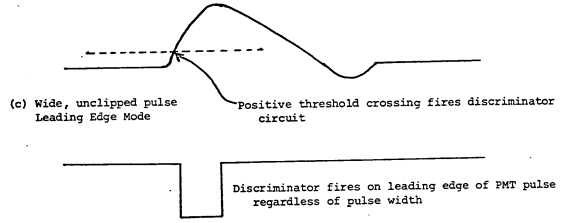

Figure 2R

Various Pulse Shapes and Discriminator Firing Modes

Reproduced with permission of the copyright owner. Further reproduction prohibited without permission.

put on the anticoincidence amplifier output and the anticoincidence discriminator was switched to leading edge mode (figure 28c) — thus ensuring that the veto pulse occurs within a few nanoseconds after the particle traverses the scintillator. The timing is not quite as accurate as in the zero-crossing mode, but by timing the 30 nsec-long discriminator veto pulse to arrive several nanoseconds before the other pulses, a slight jitter would be no problem. This reduced the rejection inefficiency to $\lesssim 10^{-3}$, which was shown earlier to be acceptable.

LINAC Anticoincidence Inefficiency Tests

When the detector was calibrated with gamma rays, the anticoincidence shield was turned on, so the detector should have recorded no counts at all except for gamma rays and an occasional random coincidence. Gamma rays were indicated by a double coincidence between the detector output and the beam console signals with an absence of any pulse from the beam counter electron monitor. The triple coincidence rate, with the presence of an electron monitor pulse, was far in excess of the expected gamma ray random rate, indicating that the detector was counting electrons as well as gamma rays. The implied inefficiency rate was nearly two orders of magnitude greater than what had been measured in the laboratory. The electron count rate with the anti-shield on (i.e., the anticoincidence inefficiency rate) was then measured for different beam rates to try to determine the cause of the anticoincidence inefficiency. Figure 29 shows a marked, non-linear increase in inefficiency rates with higher beam rates. At the lowest beam rate, 15 electrons sec^{-1}, the anticoincidence inefficiency was only slightly higher than when measured in the laboratory. The inefficiency

Reproduced with permission of the copyright owner. Further reproduction prohibited without permission.

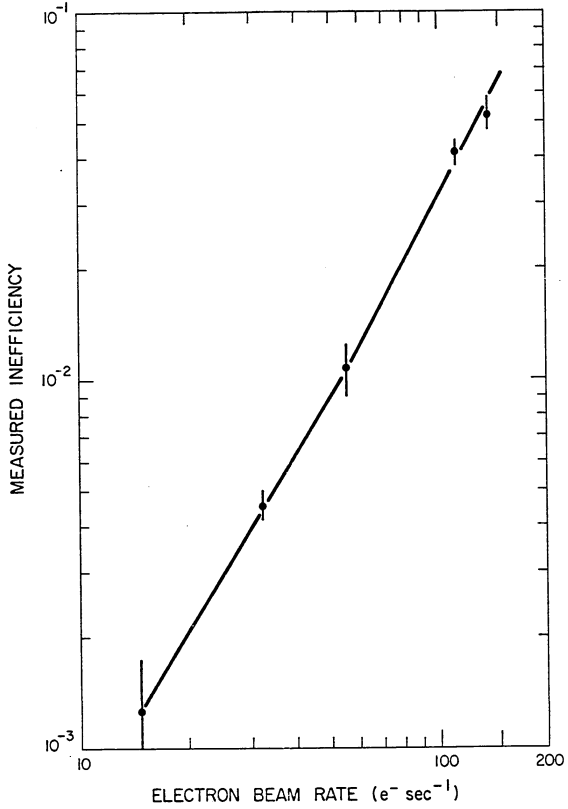

Figure 29

Increase in Anticoincidence Inefficiency with Electron Beam Rate. 60 MeV Electrons from NRL LINAC

Reproduced with permission of the copyright owner. Further reproduction prohibited without permission.

measurements were repeated with the detector turned 180° in the beam, so that the electrons entered through the mirror; this should have reduced the count rate to zero, since the coincidence timing would be out of phase by ∿ 25 nsec. However, table 3 shows that although low beam rates gave no detected events, counts were still recorded at high beam rates. Moving the detector out of the beam reduced the count rate to zero, eliminating the possibility that room background, possibly increasing with higher beam rates, was causing the inefficiency counts.

The NRL beam counter electron monitor scintillator rejected electrons with an inefficiency of less than 1 part in 250,000, so any apparent inefficiencies in the detector were not caused by the presence of unmonitored electrons. If some anticoincidence photomultiplier pulses were failing to trigger the discriminator, changes in the beam rate would have had little effect on the measured inefficiency. The dependence of the inefficiency on the beam rate seemed to indicate either a dead time problem or a random count effect. The 15 nsec anticoincidence discriminator output followed by its own reflection should give zero dead time 30 nsec veto pulses. The singles rates in the individual photomultipliers are increased negligibly by a high beam rate, since the singles rate from real electrons is much less than the intrinsic tube noise. So if the electron pulse distributions were completely random, then the random coincidence rate should be unaffected by the beam rate.

When the converter-scintillator photomultiplier pulses were viewed in an oscilloscope, they showed a pronounced bunching in 1 μsec intervals following the principal electron pulses (figure 30). These afterpulses could have been caused by multiple pulsing or oscillations in the tubes. The effective singles count rate, for 1 μsec after each real electron

Reproduced with permission of the copyright owner. Further reproduction prohibited without permission.

Electron Beam Rate (sec^{-1})	Anticoincidence Inefficiency
8.8	0
28	$(1.8 \pm .7) \times 10^{-3}$
158	$(9.8 \pm 1.0) \times 10^{-3}$

Table 3

Anticoincidence Inefficiency vs. Electron Beam Rate with Detector Turned 180° in LINAC Beam.

Reproduced with permission of the copyright owner. Further reproduction prohibited without permission.

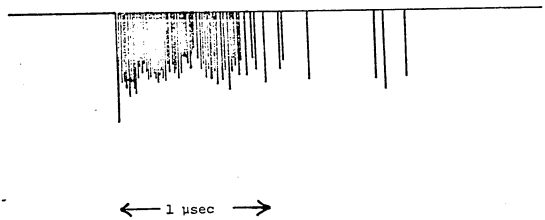

Figure 30

Pulse Bunching after Principal Electron Pulse

Reproduced with permission of the copyright owner. Further reproduction prohibited without permission.

entered the detector, became extremely high, and random coincidences between the normal Čerenkov photomultiplier pulses and the converter-scintillator afterpulses could occur frequently, since only the first 30 nsec of the 1 μsec was protected by the veto pulse. These false events would be strongly dependent on the electron beam rate, as was observed. They would also be observed when the detector was turned 180° in the beam, since the 25 nsec effective timing delay in the RCA 4522 pulses would not prevent their random coincidences with the converter-scintillator afterpulses lasting 1 μsec.

The converter-scintillator photomultiplier tubes were operated off the same high voltage supply as the anticoincidence shield tubes. The voltage was set near the maximum level for the tubes (1250 v.) to ensure minimum charged particle rejection inefficiency by the anti-shield. However, whereas .5% inefficiency is too high for the anti-shield, 99.5% detection efficiency for the converter-scintillator is more than sufficient. Reducing the voltage on the converter-scintillator photomultipliers would stop their oscillations and multiple pulsing. For future flights, a separate power supply or a voltage divider network can be used to operate the converter scintillator photomultipliers at a lower voltage than the anticoincidence tubes. Also, a better light collection arrangement will allow lower voltages on all tubes.

"Random" events occurring during the afterpulsing can be completely eliminated by effectively "shutting off" the detector for $\sim$ 2 μsec after each electron event, waiting until afterpulsing subsides before allowing any more events to be registered. This modification was incorporated into the detector before its first balloon flight.

Reproduced with permission of the copyright owner. Further reproduction prohibited without permission.

The 30 nsec anticoincidence discriminator output, which had previously gone into the coincidence veto input, was inverted, stretched to 2 μsec, and run directly into the pulse height analyzer circuitry, where it fired a flip-flop whose state governed one of the output bits. Without any veto input, the coincidence unit registered charged particle events as well as neutral events. The coincidence output pulses gated the pulse height analyzer, as before. The two pulse height bits, along with one more used for event identification, were combined with the bit indicating whether or not a veto pulse had occurred during the event and were fed into a four-bit shift register to be read out into the telemetry. Since the veto pulse is stretched to 2 μsec, the telemetered pulse train for all events, real or random, occurring within 2 μsec after the anti-shield has been triggered will include a veto bit. In addition to giving better protection against detecting charged particles, this system allowed charged particle rates as well as gamma ray rates to be monitored throughout the flight.

This rebuilding was done in Palestine, Texas, so we could not retest the detector's anticoincidence inefficiency in a high-rate electron beam. However, during the flight both the gamma ray and charged particle count rates at float were near what was expected, assuming $\lesssim$ 0.1% veto inefficiency. An inefficiency such as was found at high electron beam rates during the LINAC testing would have resulted in an apparent gamma ray rate at float at least ten times higher than was observed.

Reproduced with permission of the copyright owner. Further reproduction prohibited without permission.

BALLOON FLIGHT AND RESULTS

Reproduced with permission of the copyright owner. Further reproduction prohibited without permission.

BALLOON FLIGHT AND RESULTS

I. Flight Description

The experiment was launched from the National Center for Atmospheric Research scientific balloon base at Palestine, Texas at 1100 UT (0600 CDT) 29 September, 1970. The net weight, including telemetry and a piggy-back experiment, was 600 lbs. The balloon (5×10^6 cu. ft.) reached an altitude of 116,100 ft. (5.4 mb) at 1320 UT, gradually rose to 117,800 ft. (5.0 mb) at 1630 UT, and remained above 117,000 ft (5.2 mb) until the flight was terminated at 2300 UT. No data was collected after 2115 UT, when battery power ended, but FAA clearance problems delayed cutdown nearly two hours. Telemetry contact was strong throughout the flight: the data were marked by only a few noise bursts, and the pointing system responded to all ground commands.

The package landed on top of the highest hill in the Indian reservation near Hobart, Oklahoma. Dense outcroppings of vertical rock strata made access by even four-wheel drive vehicle impossible, and cacti and rattlesnakes made approach on foot difficult. Despite a valiant helicopter rescue effort carried out by the U. S. Army, our pointing system was lost to a band of scavenging locals. The F.B.I. was called in but decided that the theft was not sufficiently connected with left-wing subversion to warrant further investigation.

Reproduced with permission of the copyright owner. Further reproduction prohibited without permission.

II. Background Radiation

Ascent

Power was switched on before launch so that the Pfotzer maximum could be observed during ascent. Although this meant two hours less battery power at float altitude, it provided a check on the operation of the detector during its first flight.

Figure 31 shows the coincidence count rates of charged and neutral radiation during ascent and the first 1 1/2 hours at float altitude. A clear maximum is evident between 40,000 ft. and 50,000 ft (180 - 120 mb) which agrees with previous measurements (Rossi, 1948).

The calculations described earlier for predicted noise and random events assumed that the ratio of dark noise (sea-level photomultiplier singles rates) to the combined dark noise and charged particle-induced noise (singles rates at float) was 1/3 for the RCA 4522 and 1/10 for the converter-scintillator tubes. This is in agreement with the monitored singles rates as shown in figure 32. Figure 33 shows the gamma ray count rate as a function of overlying air pressure. The ascent was rapid enough so that only a small number of counts were recorded in each height interval. The resulting statistical errors are too large to prevent an accurate linear extrapolation to 0 pressure, but inspection shows that the atmospheric gamma ray background rate during the flight was at least an order of magnitude larger than the extrapolated rate above the atmosphere. This residual non-atmospheric background would be the extraterrestial gamma ray events caused by random coincidences in the detector, which are thus shown to be negligible.

Reproduced with permission of the copyright owner. Further reproduction prohibited without permission.

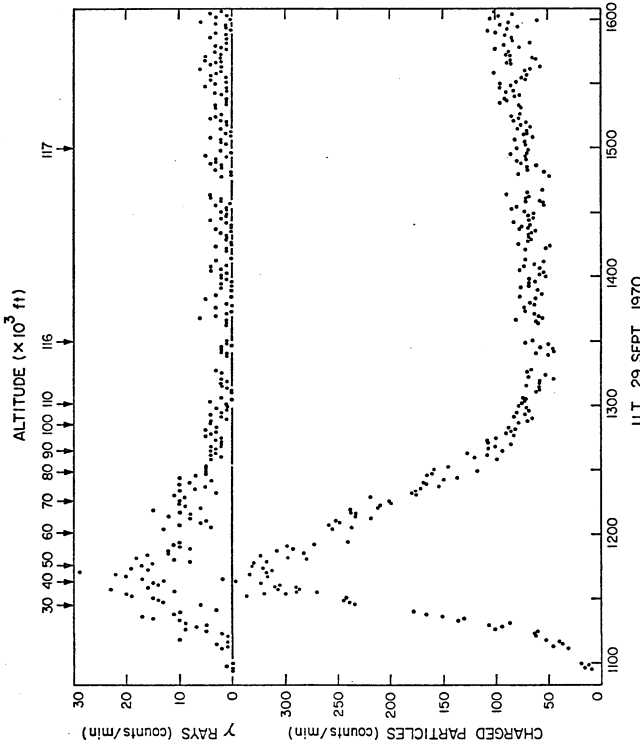

Figure 31

Gamma Ray and Charged Particle Coincidence Rates
vs. Altitude (0° Zenith Angle)

Reproduced with permission of the copyright owner. Further reproduction prohibited without permission.

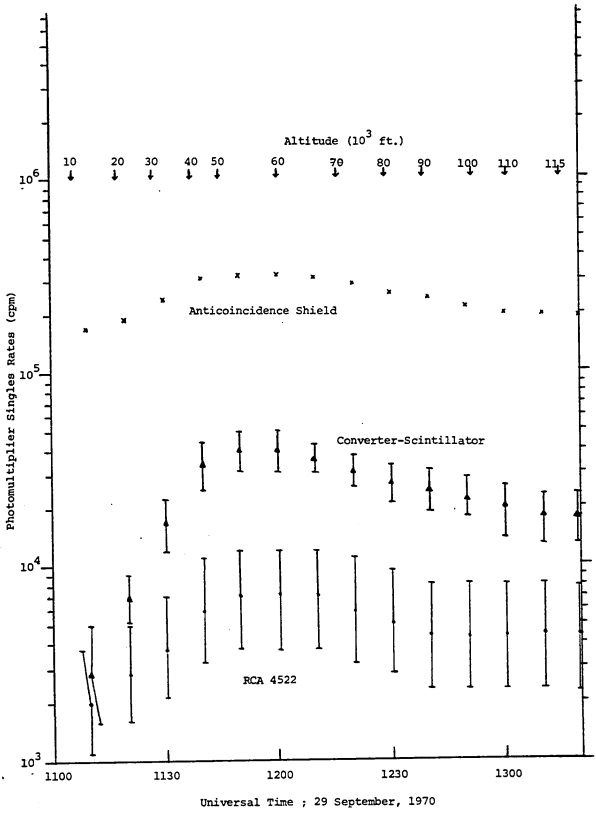

Figure 32

Photomultiplier Singles Rates vs. Altitude, Time

Reproduced with permission of the copyright owner. Further reproduction prohibited without permission.

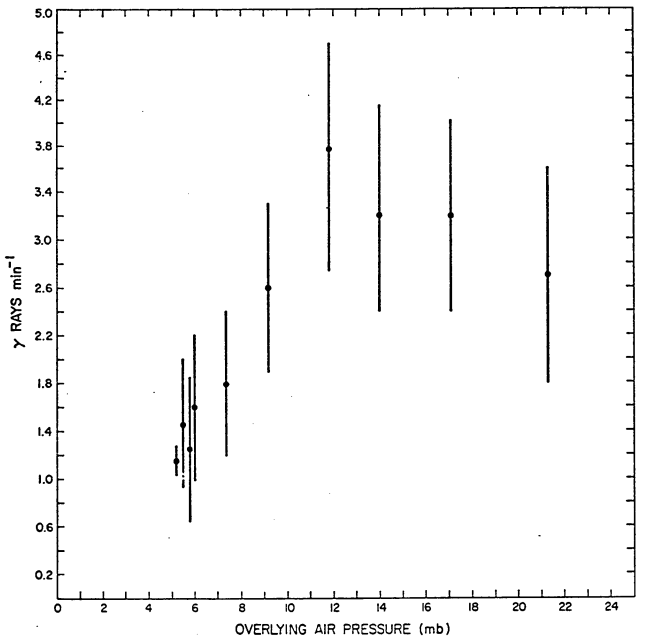

Figure 33

Gamma Ray Count Rate vs. Overlying Air Pressure

Reproduced with permission of the copyright owner. Further reproduction prohibited without permission.

At 1330 UT the detector, which had previously been pointed at the zenith, was pointed to 30° zenith angle to start tracking the Crab nebula; the increase in the gamma ray count rate at this time is mostly due to the sec z (z = zenith angle) factor for atmospheric gamma ray production, which is discussed below.

Zenith Angle Dependence

In order to get maximum observing time on the Crab nebula, which had already transitted when observations began, the source was tracked continuously from 30° down to 60° zenith angle. Background measurements were then made both before and after the observing period for M87. Previous experiments (Fichtel, et al., 1969) have shown that the gamma ray background at balloon altitudes varies as sec z. The explanation for this is simply the near-linear increase with sec z of the length of the path through the atmosphere along which cosmic rays produce secondary gamma rays.

Figure 34 shows the angular dependence of gamma ray intensity in the atmosphere as measured by this experiment. The statistical uncertainty for most of the points are large, since only the measurements at the highest and lowest zenith angles were made specifically to determine the background; the rest were short measurements taken when the detector was inadvertently pointed off-source. The measurements are consistent with a pure sec z dependence, which would be represented by a horizontal line on the graph.

Except for a small increase in atmospheric absorption, there should be no change with z in the flux from a source. Therefore, in

Reproduced with permission of the copyright owner. Further reproduction prohibited without permission.

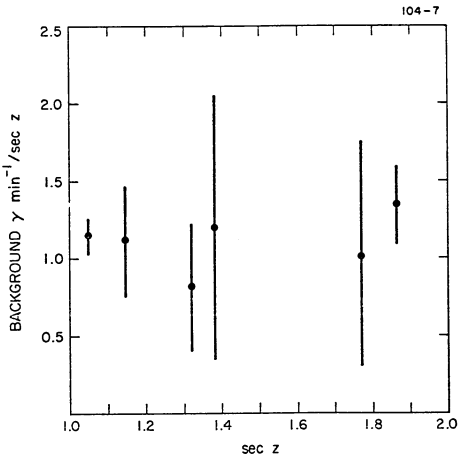

Figure 34

Angular Dependence of Background Gamma Rays in the Atmosphere

Reproduced with permission of the copyright owner. Further reproduction prohibited without permission.

comparing source and background measurements, there must be compensation for the variation of the background with zenith angle. If an on-source measurement at high z is compared to a background measurement at low z, there will be a spurious "source" excess which is nothing more than background enhancement at high z. The average vertical background flux was calculated from off-source measurements by dividing each measurement by the appropriate sec z. Then the source observations were divided into small segments of time, in each of which z was fairly constant; for each time segment an effective background B(z) was computed by $B(z) = \sec z \, B(0)$. This effective background was then added up over all on-source times, just as were the real source measurements, and the two were compared to see if a flux from the source had been detected.

Measured Atmospheric Gamma Ray Intensity

Table 4 shows results of atmospheric gamma ray integral flux measurements at 50 MeV and below by various groups. The integral spectral index for atmospheric gamma rays between 50 MeV and 100 MeV is 0.5 (Fichtel, et al., 1969; Frye and Wang, 1969). The average measurements at 50 MeV and 30 MeV show an integral spectral index of 0.4. The flattening of the spectrum below 50 MeV is predicted by theoretical studies of atmospheric gamma radiation (Cavrak, 1971; Puskin, 1970). The superposition of a pion-produced gamma ray spectrum, with a peak at 70 MeV, onto a power law bremsstrahlung spectrum is responsible for this flattening.

In converting the observed background count rate from the present experiment into an atmospheric flux, it is necessary to consider the angular response of the detector. If B is the background flux, ε the

Reproduced with permission of the copyright owner. Further reproduction prohibited without permission.

Threshold Energy (MeV)	Atmospheric Depth (mb)	Gamma Ray Flux ($\times 10^{-3}$ γ cm^{-2} $sec^{-1}sr^{-1}$) measured	per mb	Investigators
> 15	5.2	8.9 ± .9	1.7 ± .2	Present Results
> 30	3.5	5.2 ± .5	1.5 ± .1	Frye and Smith (1966)
> 30	2.3	3.7 ± .4	1.6 ± .2	Frye and Wang (1968)
> 30	3.0	5.7 ± .6	1.9 ± .2	Fichtel, et al. (1969)
> 50	3.0	4.8 ± .5	1.6 ± .2	Fichtel, et al. (1969)
> 50			1.2 ± .1	Frye and Wang (1969)
> 50			1.3 ± .2	May and Waddington (1969)
> 50			1.3 ± .3	Frye, et al. (1971)

Table 4

Atmospheric Gamma Ray Measurements

Reproduced with permission of the copyright owner. Further reproduction prohibited without permission.

detector efficiency, A the detector area, and Ω the detector solid angle, then the background count rate is $B\varepsilon A\Omega$. However, both Ω and ε vary with energy E_γ and off-axis angle θ. In a background spectrum of the form $B = B_0 E_\gamma^{-\Gamma}$, the count rate will be

$$\int_{E_\gamma}^{\infty} \int_{0}^{\pi} AB_0 E^{-\Gamma} \varepsilon(\theta,E) 2\pi \sin\theta \, d\theta \, dE \ .$$

We can define an effective $\overline{\varepsilon\Omega}(> E_\gamma)$ such that

$$\frac{1}{\Gamma-1} A \, \overline{\varepsilon\Omega}(> E_\gamma) B_0 E_\gamma^{-(\Gamma-1)} = AB_0 2\pi \int_{E_\gamma}^{\infty} \int_{0}^{2\pi} E^{-\Gamma} \varepsilon(\theta,E) \sin\theta \, d\theta \, dE \ .$$

This can be integrated numerically, using for $\varepsilon(\theta,E)$ the results of the Monte Carlo calculations and the LINAC calibration. $\Gamma = 1.4$ for $E_\gamma < 50$ MeV and 1.5 for $E_\gamma > 50$ MeV. The result is $\overline{\varepsilon\Omega}(> 15 \text{ MeV}) = 1.48 \times 10^{-3}$ sr, whence $A\,\overline{\varepsilon\Omega}(> 15 \text{ MeV}) = 2.15$ cm^{2}sr. The flux which would produce the observed (reduced to 0° zenith angle) count rate of $1.15 \pm .12$ γ min^{-1} is

$$F_\gamma(> 15 \text{ MeV}) = (8.9 \pm .9) \times 10^{-3} \ \gamma \ \text{cm}^{-2}\text{sec}^{-1}\text{sr}^{-1} \ .$$

With an integral spectral index of 0.4, the equivalent flux at 30 MeV is $(6.8 \pm .7) \times 10^{-3}$ γ cm^{-2}sec^{-1}sr^{-1}. These measurements were taken with an average overlying air pressure of $\sim$ 5.2 mb. The vertical gamma ray flux near the top of the atmosphere is proportional to the overlying residual pressure (Frye and Wang, 1959). The present measurement thus reduces to an equivalent flux of $F_\gamma(> 30 \text{ MeV}) = (1.3 \pm .1) \times 10^{-3}$ cm^{-2}sec^{-1}sr^{-1}mb^{-1}, which is 22% smaller than the average of the reported fluxes > 30 MeV shown in Table 4. The difference is 2σ and may not be statistically significant.

Reproduced with permission of the copyright owner. Further reproduction prohibited without permission.

The statistical error of 21% in the measured efficiency of the detector could account for some of this discrepancy.

The Monte Carlo calculations of the angular response of the detector were only checked using 60 MeV electrons. Several Gaussian approximations of angular distributions were folded together to transform the electron measurements into a gamma ray response curve. Because the solid acceptance angle is calculated from the square of the "measured" angle, the discrepancy between the measured flux and the extrapolation from higher energies could be caused by a 13% overestimate of the half-angles plotted in figure 25. The possible causes for overestimates of these angles were discussed earlier. The uncertainties in the angular response measurements require that the present atmospheric background results be treated with caution. An accurate angular response calibration with gamma rays is necessary to determine the response of the detector to a diffuse incident gamma ray spectrum. Despite the uncertainties, the results of this flight definitely show that the atmospheric gamma ray spectrum below 30 MeV is flatter than at higher energies.

Note that the uncertainties do not affect the accuracy of point-source measurements. If the detector is pointed at a source, only the on-axis efficiency need be known. In an analysis of observations of a source, the background is not calculated, it is measured independently of any calibration. Only if a source is allowed to drift across the detector's field of view or if a source is diffuse must the detector's angular response be known to interpret the measurements.

Reproduced with permission of the copyright owner. Further reproduction prohibited without permission.

Pulse Height Analysis

Table 5 shows the fraction of background events, both neutral and charged, falling into the various pulse height bins. The original RCA 4522 photomultiplier was replaced shortly before the flight because of noise problems and the high voltage was lowered. The calibration of the pulse height analyzer, putting the maximum pulse level for single converted electrons in bin 3, was therefore uncertain. If the pulse height analyzer were working as originally planned and calibrated, no single-particle, singly-charged events would be counted in the highest energy bin. At energies above the heavy particle Čerenkov threshold ($\sim$20 GeV/nucleon) He is $\sim$ 10% as abundant as H in cosmic radiation (Meyer, 1969). The primary cosmic ray count rate was estimated earlier to be 0.8 sec^{-1}, of which $\sim$ 0.08 sec^{-1} would be He. Albedo electrons give $\sim$ 0.8 counts sec^{-1}, so the expected fraction of events with charge $\geq$ 2 is 0.08/1.6 = 0.05. The emission rate of Čerenkov radiation varies as the square of the charge, so these He events produce at least four times as much Čerenkov light as singly-charged particle events and should be recorded in bin 4. Given the uncertainty in the level of the singly-charged particle threshold, the fraction of charged particle events in bin 4 is consistent with the interpretation that these are mostly He nuclei. Regardless of the interpretation, the increased fraction of high light level events for the neutral over the charged particle events shows that the neutral events are indeed different from the charged particle events. If the anticoincidence veto system had been inefficient and a large fraction of the recorded neutral events were merely unvetoed charged particle events, the neutrals' pulse height spectrum would be the same as the

Reproduced with permission of the copyright owner. Further reproduction prohibited without permission.

	Neutral	Charged
BIN1	0.38 ± .05	0.34 ± .02
BIN2	0.33 ± .04	0.40 ± .02
BIN3	0.19 ± .03	0.23 ± .01
BIN4	0.10 ± .02	0.03 ± .01

Table 5

Pulse Height Distribution of Atmospheric Radiation

Reproduced with permission of the copyright owner. Further reproduction prohibited without permission.

charged particles'. The enhanced count rate in the highest energy bin for the neutral events is consistent with the production of electron-positron pairs by gamma rays. Since the exact pulse height threshold for single particle events is uncertain, there is a corresponding uncertainty in using figure 17 to estimate the background gamma ray spectral index. However, with the threshold in bin 3, as is consistent with the H-He interpretation for the charged events, the neutral two-particle fraction 0.10 ± 0.2 corresponds to a differential spectral index $\Gamma_\gamma = 1.64 \pm .04$, which for the accuracy of this method of spectral determination is not in bad agreement with the value 1.4 measured by the other investigators.

III. Reduction of Pointing Information

Preflight Testing

The magnetometer, sunsensor, and vertical potentiometer outputs were all calibrated through an r.f. telemetry link before the flight.

The response of the magnetometers should have the form $v = a + b \cdot \cos\theta$, where v is the output voltage, θ is the angle between the magnetometer probe and magnetic north, b is determined by the gain of the electronics and the telemetry, and 'a' is a bias level which can be monitored during the flight. Preflight testing showed that the mean voltage of one of the magnetometers differed from its bias voltage. This deviation was compensated for in making the calibration curves used for steering the package during the flight but left an uncertainty in how much confidence could be placed in the readings of that magnetometer.

Reproduced with permission of the copyright owner. Further reproduction prohibited without permission.

The two magnetometers are crossed at 90° to facilitate quadrant determination. Because of the cosine response function, when one magnetometer is aligned with the field its output is relatively insensitive to small rotations. At these times, only one magnetometer can be used for steering. For intermediate angles with respect to the field, both magnetometers are sensitive. At these times during the flight, the magnetometer with bias problems was recalibrated against the properly functioning magnetometer.

Post-Flight Analysis

After the flight, the procedure used to determine the proper pointing settings for the detector was reversed to deduce the orientation of the detector from the telemetry data. Obtaining the vertical angle was straightforward, using the simple preflight calibration curves for the vertical potentiometers with hanging bobs. The readings obtained from the two pots agreed to within a degree, the differences being caused mainly by backlash. The raw magnetometer readings were converted into angles with respect to the local magnetic field, using the calibration curves obtained from preflight ground measurements on the normal magnetometer. The other magnetometer's mean voltage differed from its bias voltage, and this magnetometer was calibrated inflight against the properly functioning

Reproduced with permission of the copyright owner. Further reproduction prohibited without permission.

instrument. The magnetic declination for the balloon's location at all times was found from a U. S. Coast and Geodetic Survey Isogonic Chart of the United States (1970.0). This was used to convert the magnetometer angles into azimuth readings.

The latitude and longitude of the balloon at all times was supplied after the flight by the National Center for Atmospheric Research. This allowed determination of the position of the sun at the time of each maximum and minimum in the output of the sunsensor. The azimuth of the detector was determined from the magnetometer data, and the difference between the solar azimuth and detector azimuth was calculated for each maximum and minimum in the output patterns produced as the detector swept past the sun. The angular difference between the solar and detector azimuths should correspond to the off-center angle of one of the maxima or minima. These are separated by > 10° (out to the fourth order), so identification of the specific maximum or minimum is unambiguous.

Once the specific maximum or minimum is identified, its angular separation from the central maximum of the output pattern can be combined with the solar azimuth to give an extremely accurate determination of the detector azimuth. The mean difference in the magnetometer- and sun sensor-determined detector azimuths was 0.9°, which is entirely adequate for this experiment, given the $\sim$ 6° half-angle of the detector.

The errors are attributable to several causes. Most important were the difficulties in the preflight ground calibration of the magnetometers. The staff at Palestine told us that many groups had found significant local magnetic anomalies in the area, which confused magnetometer calibrations. We used a sensitive surveyor's compass,

Reproduced with permission of the copyright owner. Further reproduction prohibited without permission.

which should have been accurate to 1/2°, to check the alignment of the magnetometers; this should have eliminated any local anomalies, but this may still have been a problem. For future flights, it would be wise to calibrate the magnetometers before going to Palestine and merely check the calibration down there. The temperature stability of the magnetometers is given as ± 3%, which corresponds to azimuth deviations of up to 1°, depending on the angle between the magnetometer and the magnetic field.

Another possible source of systematic error may be a deviation of the isogonic lines at float altitude from their sea level position (the observed errors were predominately in the same direction). We were unable to find any data to confirm or deny this possibility. Changes with altitude of the horizontal and vertical magnetic field components should not affect the pointing accuracy of the magnetometers. As the balloon drifted during the flight its local magnetic declination changed. During the flight, new balloon position measurements were given to us by the ground controller several times an hour, and we used these to correct the declination estimates. Changes in the balloon's position also necessitated making corrections for changes in the local sidereal time of the detector with respect to the local sidereal time at the balloon base. In post-flight reconstruction of the detector's position the corrections for drift are limited by the accuracy of the interpolation between successive position determinations, which should be better than 0.1°. The actual pointing during the flight was accurate only to several tenths of a degree, since each balloon position had to be used until a subsequent position was made available. The vagaries of the wind would have made extrapolation fruitless.

Reproduced with permission of the copyright owner. Further reproduction prohibited without permission.

IV. M87

Results of 29 September, 1970 Flight

The total exposure time on M87 was 115.5 minutes. M87 transitted during the observations, with a maximum elevation of 71°. 145 gamma rays were counted during the observing period. The expected background, corrected for changing zenith angle during the observations, was 145 counts, so no source excess at all was observed. Using the maximum likelihood method described by Hearn (1968), the 95% confidence upper limit on the number of counts which could have come from the source is 31 gamma rays. The corresponding source flux upper limit is $F(> 15 \text{ MeV}) \leq 31/t\varepsilon(> 15 \text{ MeV})AT$ $\gamma \text{ cm}^{-2}\text{sec}^{-1}$. $t = 0.89$, the transmission of gamma rays through the overlying atmosphere, the aluminum detector cap, and the anti-shield. $A = 1.45 \times 10^3 \text{ cm}^2$, the detector's area. $T = 6.93 \times 10^3$ sec, the exposure time. $\varepsilon(> 15 \text{ MeV}) = 0.013$, the integral detection efficiency. Figure 35 shows the 95% confidence upper limit source flux from M87,

$$F_\gamma(> 15 \text{ MeV}) \leq 2.7 \times 10^{-4} \ \gamma \text{ cm}^{-2}\text{sec}^{-1} ,$$

along with results from other recent X-ray and gamma ray experiments, plotted on a graph of the entire electromagnetic spectrum of M87 (NGC4688, 3C294, Virgo A).

Comparison with Other Detectors and Interpretation

There has been some controversy about the magnitude of the X-ray flux from M87. Haymes, et al. (1968, 1970) claim to have seen a positive flux between 40 KeV and 100 KeV, while Peterson (1970) and McClintock,

Reproduced with permission of the copyright owner. Further reproduction prohibited without permission.

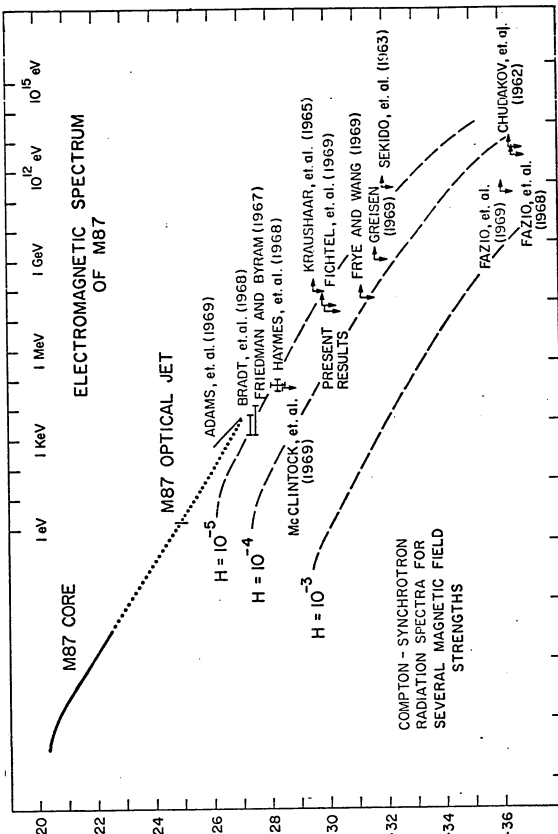

Figure 35

Electromagnetic Spectrum of M87 with Present and Previous High-Energy Observations

Reproduced with permission of the copyright owner. Further reproduction prohibited without permission.

et al. (1969) report upper limits lower than Haymes' reported flux. Measurements by Bradt, et al. (1967) of 1.5 - 6 KeV X-rays indicated a source strength nearly three times lower than that reported by the group at the Naval Research Laboratory (Byram, et al., 1966; Friedman and Byram, 1967) and the group at the University of Leicester (Adams, et al., 1969). To avoid the *ad hoc* assumption of source variability, explanations for the discrepancies centered around the methods of measuring background. However, Byram, et al. (1971) have recently reported results of positive observations, all taken with the same detector, which indicate real source variability.

The upper limit for the flux of gamma rays with E > 50 MeV set by Frye and Wang (1969) must be treated carefully when comparing it with results of other gamma ray experiments, since that detector failed to see the galactic center gamma ray source reported by Clark, et al. (1968, 1970) and by Kniffen and Fichtel (1970).

The structure of M87 (Felton, 1968) is complicated by its jet, whose length is $\sim$ 20" and width $\sim$ 2" — too small to be resolved from the central core by present X-ray detectors. The radio source Virgo A has a core-halo structure. The optical and X-ray observations all fall on a power law spectrum of index 0.67. Shklovskii (1967) argues for the likelihood of the radio core being identical with the optical jet, which is a synchrotron emitter; the X-rays in this model are the high-energy continuation of the jet's synchrotron spectrum. DeVaucouleurs (1969) has shown that most of the jet's optical radiation comes from 3 clumps with diameter $\sim$ 0.3". The Compton-synchrotron gamma radiation from such a source was calculated and is plotted as dashed lines in figure 35 for different values of the average magnetic field in the core-jet.

Reproduced with permission of the copyright owner. Further reproduction prohibited without permission.

The (interpolated) assumed spectrum between the radio, optical, and X-ray observations is shown as a dotted line. None of the balloon experiments carried out so far, including the present one, has been able to set as limiting a constraint on the magnetic field as have the ultra-high energy ground based gamma ray results of Fazio, et al. (1969): $H > 3 \times 10^{-4}$ gauss. As Felton (1967) shows, fields of this strength require *in situ* acceleration of electrons throughout the jet, but, combined with gamma ray upper limits, do not allow secondary electron production by the decay of mesons resulting from proton-proton collisions.

V. Crab Nebula

Search for Steady Emission

The total exposure time on the Crab Nebula was 116 min., following the Crab after transit from an elevation of 60° down to 30°. 212 gamma rays were counted during the observing period. The expected background, corrected for changing zenith angle and balloon elevation during the observations, is 195 counts.

The 17 indicated source counts would correspond to a source flux of 1.4×10^{-4} γ cm^{-2}sec^{-1}, but the likelihood of this result is only 49%. The upper limit on the source flux, with 95% confidence, is

$$F_\gamma(> 15 \text{ MeV}) \leq 4.7 \times 10^{-4} \ \gamma \text{ cm}^{-2}\text{sec}^{-1} .$$

No claim can be made for having observed the source with a 49% confidence result. However, it is interesting to plot the hypothetical flux, along with the derived upper limit, on a graph of other observations

Reproduced with permission of the copyright owner. Further reproduction prohibited without permission.

of the Crab Nebula (figure 36). The upper limit lies a factor of 3 above the straight line extrapolation of previous lower energy results, while the flux corresponding to the observed source count excess lies on the extrapolation. Two additional cuts of the present data are of interest. The data from the first third of the Crab observations, taken when the Crab was highest and hence the observed background gamma radiation was lowest, show a source detection with 76% likelihood. The background spectrum is harder than the expected Crab spectrum, so eliminating the counts in the highest energy bin of the pulse height analyzer should increase the signal to noise ratio if the source is real. This was described in the section on Monte Carlo results. With counts in the high energy PHA bin eliminated, the data from the entire period during which the detector was pointed at the Crab Nebula indicated a 74% likelihood of having observed a source. Effects of around 75% likelihood are not evidence for an observed source. But the increased likelihood of a possible effect when the data are cut in the two ways just described is consistent with having observed a real source flux and suggests that a second, improved flight might be able to observe a 3σ effect. This makes it worthwhile to investigate the ways of improving the detector's sensitivity for a second flight.

Search for Pulsed Gamma Rays from NP0532

Pulsed X-radiation has been observed from NP0532 with the same period ($\sim$ 33 msec) as the optical and radio pulses [Fritz, et al., 1969, 1971; Bradt, et al., 1969; Ducros, et al., 1970; Boldt, et al., 1969; Floyd, et al., 1969; Fishman, et al., 1969]. If the X-rays are synchrotron radiation, synchrotron gamma rays could be produced by the high energy

Reproduced with permission of the copyright owner. Further reproduction prohibited without permission.

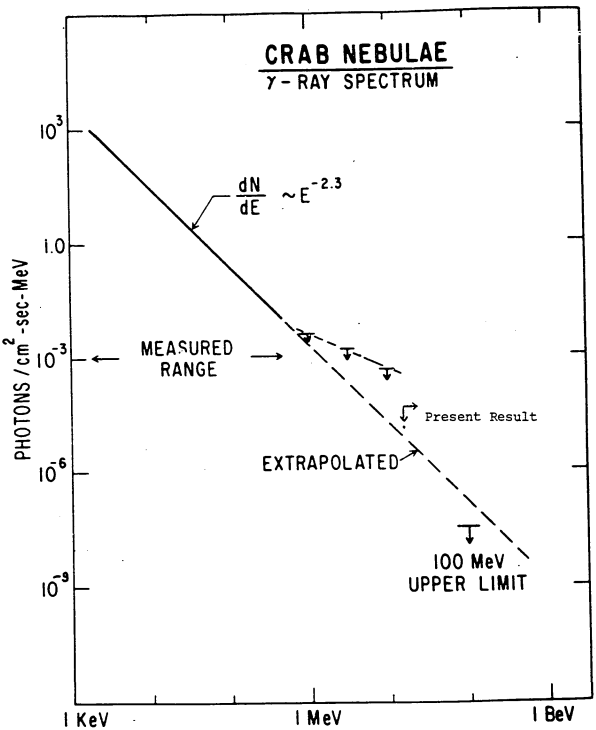

Figure 36

The hard X-ray spectrum of the Crab Nebula (Peterson, 1969).

Reproduced with permission of the copyright owner. Further reproduction prohibited without permission.

tail of the radiating electrons. These electrons could also scatter lower energy photons up to gamma ray energies. If protons as well as electrons are accelerated by the pulsar, proton-proton collisions could produce pion-decay gamma rays. These gamma rays might be absorbed by pair production in the electromagnetic field of the pulsar or in the material surrounding the pulsar if the proton acceleration occurs near the pulsar surface. So little is known about the nature of pulsar radiation that this possibility should not discourage a search for gamma rays from NP0532.

All the data on the Crab Nebula from the 29 September, 1970 balloon flight of the present detector were phase analyzed for a period of 33.1128966 msec, with barycentric corrections applied and updated throughout the flight. Each gamma ray event was placed in a 3 msec bin corresponding to its time of arrival with respect to the pulsar phase, as determined from optical observations by Drs. P. Horowitz, C. Papaliolios, and N. P. Carleton. The resulting phase distribution of gamma rays from this flight is shown in figure 37. No pulse structure is evident. A χ^2 analysis shows a 63% probability that a random pulse distribution would produce larger fluctuations in the pulsar phase diagram than were observed here.

An upper limit for possible pulsed gamma ray emission from NP0532 was set by finding the number of gamma rays necessary to give 3σ peaks in the two bins corresponding to the primary and secondary optical peaks. This number was converted into a source flux using the detector's time-area-efficiency factor, as was done in the previous analysis of non-pulsed gamma radiation. The resulting upper limit

Reproduced with permission of the copyright owner. Further reproduction prohibited without permission.

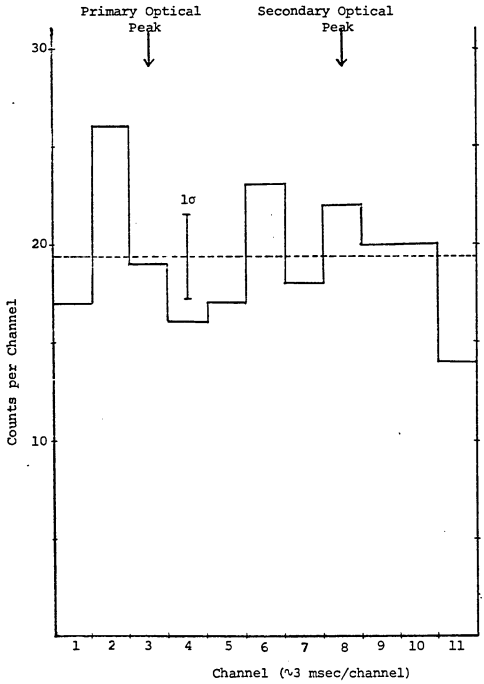

Figure 37

Gamma Rays from the direction of NP0532
Phase-Analyzed for a Period of 33.1129 msec

Reproduced with permission of the copyright owner. Further reproduction prohibited without permission.

$$1.7 \times 10^{-4} \ \gamma/cm^2 sec$$

is plotted in figure 38, along with other X-ray and gamma ray observations of NP0532. Kinzer, et al. (1971) and Vasseur, et al. (1970) have reported positive observations of pulsed gamma rays from NP0532 with energies above 10 MeV and 100 MeV, respectively. Fichtel, et al. (1971) and Frye and Wang (1969) have reported upper limits at a 95% confidence level which lie below the reported observed fluxes. The present upper limit also falls below the NRL result. Their result was reported simply as a gamma ray flux between 10 MeV and 150 MeV. The conversion of this result into a differential energy flux as plotted in figure 38 is highly dependent on the assumed energy spectrum. The results shown here assume an $E^{-2.1}$ differential photon spectrum between 10 MeV and 150 MeV. The present upper limit is consistent with the low energy gamma ray observations of Kurfess (1971).

Figure 39 (Apparao and Hoffman, 1970) is a plot of the calculated Compton-synchrotron gamma radiation from NP0532, calculated for different values of the magnetic field in the emission zone, with the assumption that the radiation is emitted isotropically from the speed of light circle. The present results set no constraint on the magnetic field further than those already set by previous results. Compton-synchrotron gamma radiation from the nebula (Rieke and Weekes, 1969; Grindlay and Hoffman, 1971) would be 2-3 orders of magnitude below the sensitivity of this detector.

The closeness of the present upper limit to the pulsed flux level reported by Kinzer, et al. (1971) suggests that if the flux is real, a small increase in sensitivity would enable this detector to measure a statistically significant effect. Ways of improving the detector's sensitivity for future balloon flights are discussed in the next section.

Reproduced with permission of the copyright owner. Further reproduction prohibited without permission.

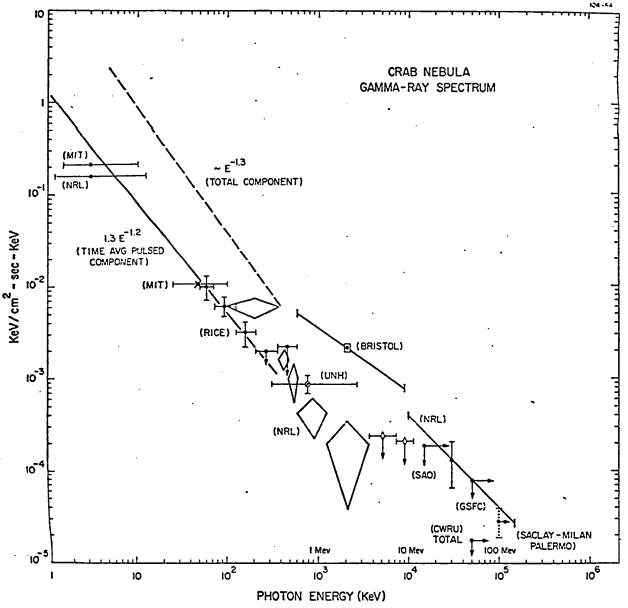

Figure 38

X-Ray and Gamma Ray Observations of NP0532

Reproduced with permission of the copyright owner. Further reproduction prohibited without permission.

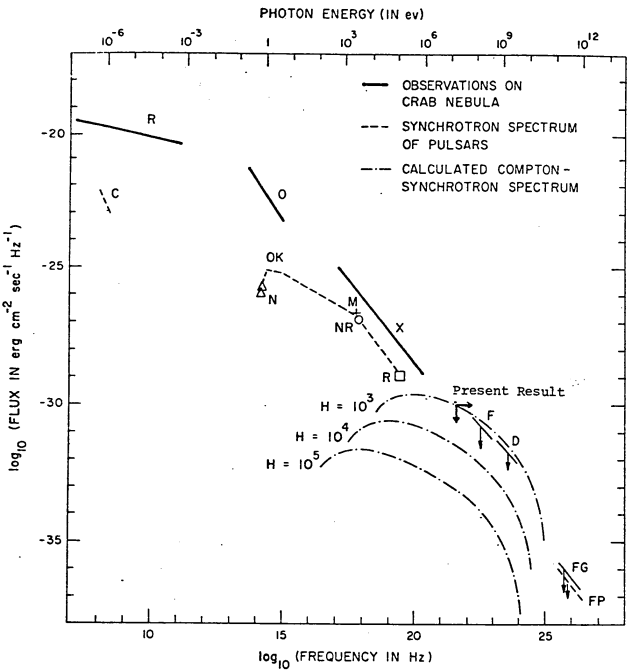

Figure 39

The electromagnetic spectra of the Crab nebula and the pulsar NP 0532, and the calculated Compton-synchrotron radiation.

Reproduced with permission of the copyright owner. Further reproduction prohibited without permission.

VI. Expected Sensitivity with Improvements in the Detector

The present flight did not take full advantage of the detector's potential sensitivity in observing the Crab Nebula because of 1) the short exposure time, 2) the relatively low float altitude, and 3) the low elevation of the Crab Nebula during the observations. The last two factors caused high background noise, and the first caused poor statistics.

A flight with a 10.6×10^6 ft^3 balloon would take the detector to 3.5 mb. An 8 hour flight centered on the Crab's transit would give 240 minutes of on-source time (half-time off-source) with an average sec z = 1.26 ($\overline{\sec z}$ = 1.46 for the present flight). The minimum detectable source flux is proportional to $\sqrt{B/AT}$, where B is the gamma ray background flux, A is the detector area, and T is the exposure time. The ideal flight described above would decrease the minimum observable flux by a factor of 2.1.

We are planning to replace the present converter-scintillator ($A = 1.45 \times 10^3 cm^2$) with a larger one ($A \simeq 3.43 \times 10^3$ cm^2). This larger area, combined with the improved exposure in a better flight, would increase the detector's sensitivity by a factor of 3.2.

Switching on the power before the launch meant using 2 1/2 hours of battery power before useful observations began. (Actually, the drain was somewhat less than during the same amount of observing time, because the pointing system motors were not activated during ascent.) For future flights, a telemetry-controlled power switch will be installed in the detector's electrical system, extending by $\sim$ 25% the observing time for each flight.

If preliminary tests with our electronics are successful, the single RCA 4522 5" photomultiplier will be replaced by a cluster of three

Reproduced with permission of the copyright owner. Further reproduction prohibited without permission.

RCA 8850 Quanticon photomultipliers, requiring a 2-out-of-3 voter coincidence to signal the detection of Čerenkov light. This will completely eliminate the problem of random coincidences as background noise. The attachment of light guides will allow the anti-shield and the converter-scintillator to be viewed edge-on, giving better light collection than with the present configuration. The photomultipliers can then be run at lower voltages, with less noise than at present — avoiding the problems described above in the section on anticoincidence inefficiency.

The heavy metal mirror can be replaced by a light, strong, molded fiberglass mirror with honeycomb backing. This would considerably reduce the weight of the detector, allowing greater balloon float altitudes to be reached. A scintillator plate behind the mirror (or a mirror constructed of scintillator material) could detect the gamma ray-produced electrons after they traverse the gas-Čerenkov counter. Including this in the coincidence logic would eliminate all random events even without changing the photomultiplier configuration at the focal point of the mirror.
At present, no more can be determined about the energies of the Čerenkov-radiating electrons except that they are higher than the Čerenkov threshold. If the proposed scintillator were thick enough to totally absorb a significant fraction of these electrons, it could provide a rough electron energy spectrum. This could be unfolded statistically from the gamma ray interactions which produce the electrons, giving some information about the form of the incident gamma ray spectrum. This possibility must be studied further, especially by inclusion in a Monte Carlo simulation, to see whether these stated advantages of a mirror-scintillator can be realized in practice.

Reproduced with permission of the copyright owner. Further reproduction prohibited without permission.

As a final improvement, one of the coexperimenters plans to accompany the recovery crew in the spotting plane, equipped with sky-diving gear and commando equipment, to protect the gondola after landing from marauding locals.

Reproduced with permission of the copyright owner. Further reproduction prohibited without permission.

APPENDIX I: DESCRIPTION OF MONTE CARLO PROGRAM FOR SIMULATION OF THE DETECTOR

Reproduced with permission of the copyright owner. Further reproduction prohibited without permission.

DESCRIPTION OF MONTE CARLO PROGRAM FOR SIMULATION OF THE DETECTOR

I. Gamma Ray Interactions

Techniques for Monte Carlo simulation of pair production and Compton scattering have been developed (Tamura, 1965; Zerby and Moran, 1963; Butcher and Messel, 1958, 1960) for investigations of electromagnetic cascade showers. (At energies above 10 MeV, photoelectric absorption of gamma rays can be neglected.) The total Compton cross section is (Bethe and Ashkin, 1953)

$$\sigma_{cs}(E) = \frac{\pi r_0^2}{E}\left\{\left[1 - \frac{2(E+1)}{E^2}\right] \ln (2E+1) + \frac{1}{2} + \frac{4}{E} - \frac{1}{2(2E+1)^2}\right\} ,$$

where E is the incident gamma ray energy, measured in units of m_0c^2. The differential pair production probability per radiation length is (Rossi, 1952)

$$\phi_{pp}(E,v) = \frac{1}{\ln(183\ z^{-1/3})}\left\{\left[v^2 + (1-v)^2\right]\left[\frac{1}{4} h_1(\delta) - \frac{1}{3} \ln z\right] + \frac{2}{3} v(1-v)\left[\frac{1}{4} h_2(\delta) - \frac{1}{3} \ln z\right]\right\} ,$$

where $\delta = 100\ z^{-1/3}\ \frac{1}{E}\ \frac{1}{v(1-v)}$ (screening parameter) and $E_e^- = vE$, $E_e^+ = (1-v)E$. Butcher and Messel's (1958, 1960) approximation for $h_1(\delta)$ and $h_2(\delta)$ were used:

$$h_1(\delta) = 20.867 - 3.242\ \delta + 0.625\ \delta^2$$

$$h_2(\delta) = 20.209 - 1.903\ \delta - 0.086\ \delta^2 \ ; \ \delta \leq 1$$

$$h_1(\delta) = h_2(\delta) = 21.120 - 4.184 \ln (\delta + 0.952) \ ; \ \delta > 1 .$$

Reproduced with permission of the copyright owner. Further reproduction prohibited without permission.

This differential cross section was integrated numerically over v to give the total pair production cross section σ_{pp}.

If the thickness of the converter is T, then the total conversion probability is

$$P_{conv} = 1 - e^{-\sigma_{tot}T}$$

where $\sigma_{tot} = \sigma_{cs} + \sigma_{pp}$. To save computer time, the program assumes that all incident gamma rays interact in the converter; thus the efficiency eventually calculated after simulating many gamma ray interactions must be multiplied by P_{conv} to give the true detector efficiency.

The depth of interaction is chosen by

$$t = -\frac{\ell n(1 - \sigma_{tot}T\xi)}{\sigma_{tot}}$$

where ξ is a random number in (0,1).

The interaction process is chosen as follows:

$$\zeta < \frac{\sigma_{cs}}{\sigma_{tot}} \qquad \text{Compton scattering}$$

$$\zeta \geq \frac{\sigma_{cs}}{\sigma_{tot}} \qquad \text{Pair production}$$

where ζ is a random number in (0,1). The program then samples the differential cross section distribution functions for the chosen interaction process to determine the energy and direction of the electron (and positron). Intrinsic pair production opening angles ($\sim m_e c^2/E$) are much smaller than typical electron multiple scattering angles (Rossi, 1952) ($\sim \frac{21.2}{E}\sqrt{x/X_0}$) and are ignored.

Reproduced with permission of the copyright owner. Further reproduction prohibited without permission.

The azimuthal Compton scattering angle is chosen randomly between 0 and 2π. The Compton scattering angle of an electron is taken with respect to the gamma ray trajectory, so the program must calculate the coordinates of the electron's new trajectory with respect to the detector axis. The geometrical transformations are described below.

Some gamma ray events produce electrons whose energy is below the threshold for Čerenkov light production in the gas and will not be detected. To save computer time, the "random" sampling of electron energies was constrained always to produce an electron with energy above the Čerenkov threshold. This constraint leaves only a fraction f_{cs}, f_{pp} of the distribution functions available for sampling, so a factor

$$f = \frac{f_{cs}\sigma_{cs} + f_{pp}\sigma_{pp}}{\sigma_{tot}}$$

must be multiplied into the calculated detector efficiency.

II. Electron Energy Loss

After the electron is produced, the program calculates its energy loss in traversing the converter-scintillator, using the formula (Evans, 1955)

$$\frac{dT}{ds} = 4\pi r_0^2 \frac{m_e c^2}{\beta^2} NZ\left[\ln \beta\left(\frac{T + m_0c^2}{I}\right)\left(\frac{T}{m_0c^2}\right)^{1/2} - \frac{1}{2}\beta^2\right] \quad \text{MeV/cm}$$

where T = kinetic energy of the electron, I = ionization energy of the medium, NZ = electrons/cm^3, and r_0 = electron radius. The detector is designed primarily to detect gamma rays below 50 MeV, whose pair-produced and Compton scattered electrons will lose energy mainly by ionization. The bremsstrahlung loss for a 50 MeV electron in 1" of NE-102 scintillator

Reproduced with permission of the copyright owner. Further reproduction prohibited without permission.

is $\sim$ 1.5 MeV whereas the ionization loss is $\sim$ 5.4 MeV. At lower energies, radiation loss per unit energy decreases while ionization loss per unit energy increases. Hence the program neglects bremsstrahlung losses.

Ionization losses will dominate once the electron has emerged into the gas, as they did in the converter-scintillator. A 10 MeV electron loses only $\sim$ .9 MeV in traversing the entire 2 meter gas column (propane at 1 atm.). This has only a small effect on multiple scattering; the only important effect might be a change in the rate of production of Čerenkov light in the gas, which depends on the velocity of the electron. If R is the rate of Čerenkov emission

$$R \propto 1 - \frac{1}{\beta^2 n^2} = 1 - \frac{1}{[1-(1/\gamma^2)]\,(1+\eta)^2}$$

where $n = 1 + \eta$ = index of refraction of the gas and $\eta \ll 1$.

$$\gamma_T = \frac{1}{\sqrt{2\eta}}$$

where $m_0c^2\gamma_T$ is the threshold energy for production of Čerenkov light. Taking the derivative of R with respect to γ, we can show that for $\gamma, \gamma_T \gg 1$,

$$\frac{dR}{R} \approx 2\,\frac{d\gamma}{\gamma}\left[\left(\frac{\gamma}{\gamma_T}\right)^2 - 1\right]^{-1}.$$

If $\gamma/\gamma_T = 1.05$ and the electron energy decreases by 10%, then the light emission decreases by a factor of 2. If all the electrons were near the threshold energy, this would be important, but only a small fraction have energies this low. Furthermore, at higher energies, the fractional energy losses are lower. A 50 MeV electron loses $\sim$ 1 MeV, causing a 1% change in light emission if the threshold energy is 10 MeV.

Reproduced with permission of the copyright owner. Further reproduction prohibited without permission.

In deciding whether or not a refinement will substantially increase the accuracy of a Monte Carlo program, it is necessary to consider not only the added accuracy which the refinement directly introduces, but also the effect of the increased computer time it requires. A Monte Carlo simulation requires a great many events to build up statistically significant results, and if computer time is limited, the improved accuracy from small refinements is often offset by a decrease in statistical accuracy resulting from running fewer trial events.

Continuous recalculation of the electron energy as it moves through the gas would require continuously recalculating the multiple scattering distribution functions (described below), which would require a lot of computer time. Because of this, the program did not consider energy loss in the gas.

III. Multiple Scattering

The program originally incorporated the accurate treatment of multiple scattering given by Scott (1963); however, this took so much computer time that Scott's angular distribution function was replaced by a simple Gaussian with a single-scattering large angle tail, as described by Rossi (1952). The loss of accuracy is small, and the increased number of trial gamma ray events made possible by the savings in computer time (factor of 10) improves the statistical accuracy of the simulation.

If $f(E,\theta)$ is the normalized probability that an electron of energy E will be scattered an angle θ in travelling a certain distance, then θ is sampled by the formula

$$\int_0^{\theta} f(E,\theta')d\theta' = \xi$$

Reproduced with permission of the copyright owner. Further reproduction prohibited without permission.

where ξ is a random number in (0,1). The program calculates a scattering matrix for different values of E and θ to avoid having to recalculate and reintegrate $f(E,\theta)$ for each new gamma ray event.

One sampling is performed to find the electron scattering in the converter; when the electron is in the gas, scattering is sampled after predetermined lengths of trajectory, usually 40 cm. After each scattering, an azimuthal scattering angle was chosen randomly between 0 and 2π, and the program calculated the new coördinates of the electron's trajectory in the detector reference frame.

IV. Angular Transformation for Scattering

Figure 40 shows the definition of the coördinates (r,θ,ϕ) used to describe the trajectory. As an electron moves along a straight line, ϕ changes. This is a disadvantage of using cylindrical coördinates; however, the ray tracing of Čerenkov light, described below, was easier to handle with cylindrical rather than rectangular coördinates and actual rather than projected angles, so the scattering was also treated this way.

The electron scatters into a cone of half-angle ϕ_s about its initial trajectory (figure 41a); ϕ_s, the azimuthal scattering angle, is chosen randomly. Figure 41b shows the geometry of the angular transformation. The apexes of the spherical triangle are the intersections of the electron's initial and final trajectories and a line parallel to the detector's axis.

If the portion of trajectory considered has length t, then the height increment Δh and horizontal increment Δr are given by

$$\Delta h = t \cos \theta_2$$
$$\Delta r = t \sin \theta_2 .$$

Reproduced with permission of the copyright owner. Further reproduction prohibited without permission.

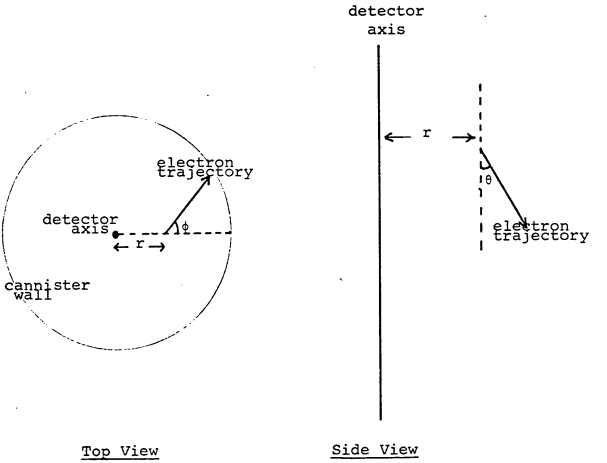

Figure 40

Coordinates used in Monte Carlo simulation

Reproduced with permission of the copyright owner. Further reproduction prohibited without permission.

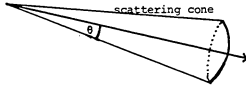

(a)

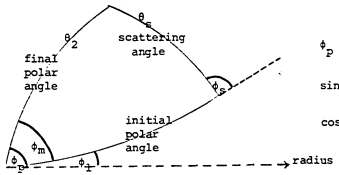

(b)

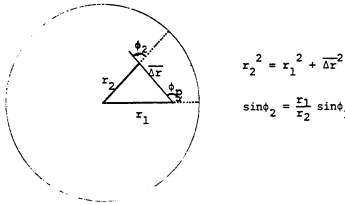

(c)

Figure 41

Calculation of new trajectory coordinates after scattering

Reproduced with permission of the copyright owner. Further reproduction prohibited without permission.

Figure 41c shows the calculation of the new radial and azimuthal coordinates r_2 and ϕ_2. The program contained provisions to avoid divergences if the trajectory passed through the detector axis ($r = 0$).

V. Čerenkov Radiation in the Gas

Since the energy of the electron and the refractive index of the gas are known, the program can calculate the rate and angle of emission of Čerenkov light by the electron. The spectral range of Čerenkov emission considered was determined by the response of the RCA 4522 phototube, 2200 Å - 5800 Å. The emission rate per centimeter in the gas is then $1290 \sin^2 \theta_c$. θ_c, the half-angle of the Čerenkov light cone, is (Jelley, 1958)

$$\cos \theta_c = 1/\beta n$$

where $\beta = v/c$ and n is the refractive index of the gas. The program allowed the simulation of different gases at varying pressures.

After calculating the coördinates of each portion of an electron's trajectory following multiple scattering, the program traced the trajectory, which is the axis of the Čerenkov light cone, down to the mirror and reflected it back towards the phototube located at the mirror's focal point.

Figure 42 shows the geometry of the ray tracing, which determines the location of the center of the Čerenkov light cone in the focal plane. With a paraboloidal mirror, the light cone intersects an equal-sized area on the focal plane regardless of the height at which the light is emitted (figure 43). This is roughly true for the central portion of a spherical mirror and was assumed in the calculations.

Reproduced with permission of the copyright owner. Further reproduction prohibited without permission.

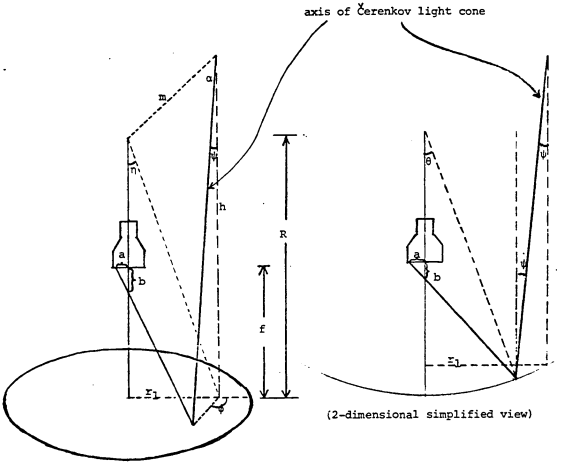

$R = 2f$

$\sin\eta = r_1/R$

$m = \left(h^2 + R^2 - 2hR\cos\eta\right)^{\frac{1}{2}}$

$\sin\alpha = r_1/m$

$\sin(\theta-\psi\cos\phi) = \frac{m}{R}\sin(\alpha+\psi\cos\phi)$

$b = \frac{R}{2}\left\{\frac{2\sin(\theta-\psi\cos\phi)}{\sin(2\theta-\psi\cos\phi)} - 1\right\}$

$a = b\cdot\tan(2\theta-\psi\cos\phi)$

a is the distance from the detector axis of the center of the Čerenkov light cone's intersection with the focal plane.

Figure 42

Position of center of Čerenkov light circle in focal plane

Reproduced with permission of the copyright owner. Further reproduction prohibited without permission.

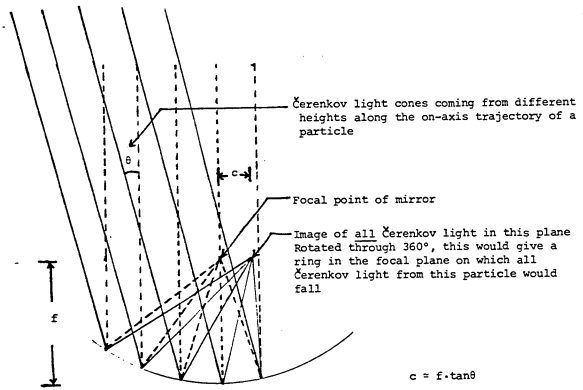

Figure 43

Formation of ring image of Čerenkov light cone from different heights along the trajectory of a radiating particle

Reproduced with permission of the copyright owner. Further reproduction prohibited without permission.

The Čerenkov cone will generally intersect an ellipse on the focal plane. The orientation of the major axis of the ellipse will follow the random distribution of electron azimuthal angles; the statistical averaging over many Monte Carlo trial events justifies treating the ellipse as a circle.

Figure 44 shows the geometry for calculating the fraction of the light cone falling on the phototube face. Multiplying the total light emission from a given part of the electron's trajectory by this fraction gives the number of photons entering the phototube from each section of the trajectory. Since the tube face is convex, the photons enter nearly normal to the surface; about 5% will be reflected (Rossi,1957) for angles of incidence up to about 30°. The program did not consider absorption or scattering of photons by the gas or the mirror surface.

VI. Efficiency Calculation

To save computer time, the program stopped following electrons which were scattered off-axis more than a predetermined angle, generally set at three times the acceptance angle of the detector optics. Otherwise, it followed each electron until it either hit the mirror or the side of the cannister or until its energy was below the threshold for Čerenkov radiation in the gas. When it finished following an electron, it checked whether or not a second electron from pair production still had to be followed. If not, it added up all the photons which had hit the phototube face for the gamma ray event being considered.

After many trial gamma ray events, the program gave the distribution of the number of photons incident on the phototube vs. the gamma

Reproduced with permission of the copyright owner. Further reproduction prohibited without permission.

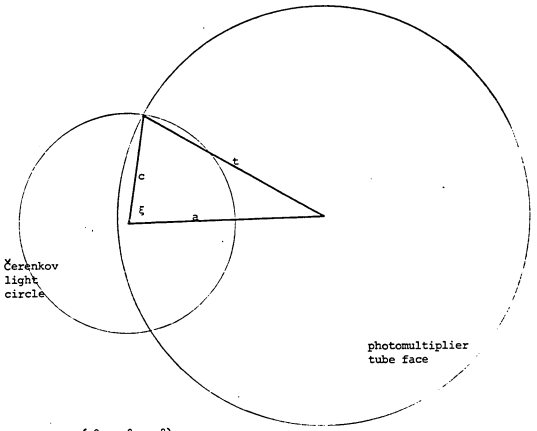

$$\xi = \arccos\left(\frac{a^2 + c^2 - t^2}{2ac}\right)$$

Fraction of light falling on tube face $= \xi/\pi$

If $|a-c| > t$, no light hits the tube face.
If $|a+c| \leq t$, all the light hits the tube face.

Figure 44

Intersection of Čerenkov light circle and photomultiplier face

Reproduced with permission of the copyright owner. Further reproduction prohibited without permission.

ray energy and direction. If the light detection threshold of the phototube is known, it is then easy to determine the detection efficiency for different energies and off-axis angles.

Figure 45 is a flow chart of the entire Monte Carlo simulation program.

Reproduced with permission of the copyright owner. Further reproduction prohibited without permission.

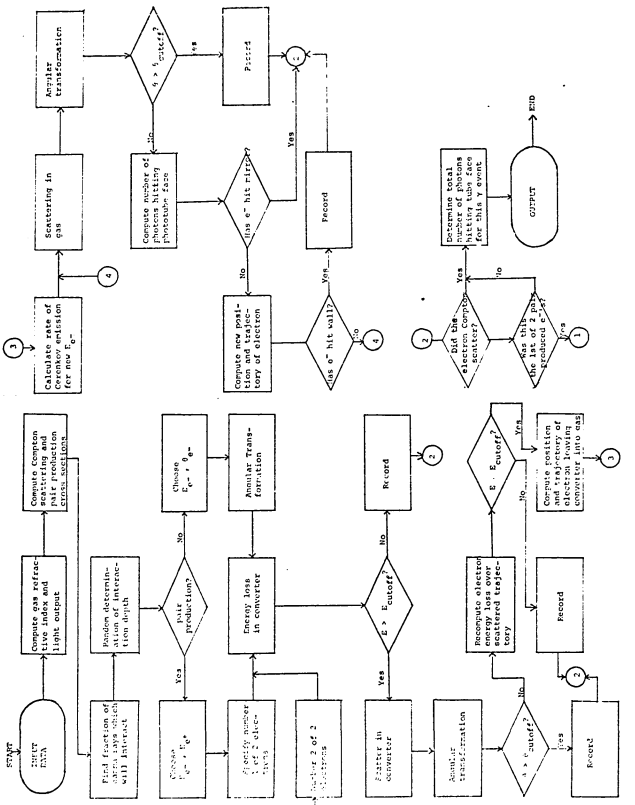

Figure 45

Flow chart of computer program for
Monte Carlo simulation of gamma ray detector

Reproduced with permission of the copyright owner. Further reproduction prohibited without permission.

APPENDIX II: GAS-ČERENKOV DETECTOR FOR LOW ENERGY GAMMA RAY ASTRONOMY

(H.Helmken and J.Hoffman, Nuclear Instruments and Methods, 80, 125.)

Reproduced with permission of the copyright owner. Further reproduction prohibited without permission.

PLEASE NOTE:

Pages 144-147, Appendix II:
"Gas-Cerenkov Detector For
Low Energy Gamma Ray Astronomy",
copyright by North-Holland
Publishing Co., not microfilmed
at request of school. Available
for consultation at Harvard
College Observatory Library.

UNIVERSITY MICROFILMS.

Reproduced with permission of the copyright owner. Further reproduction prohibited without permission.

REFERENCES

Reproduced with permission of the copyright owner. Further reproduction prohibited without permission.

REFERENCES

Adams,D.J., Cooke,B.A., Evans,K., and Pounds,K.A. (1969), "Rocket Observations of Virgo XR-1." Nature, 222, 757.

Albats,P., Frye,G.M.,Jr., Maynard,J.L., Staib,J.A., and Zych,A.D., (1970), "Background Evaluation for a Satellite Gamma Ray Spark Chamber." Paper presented at the American Physical Society Meeting, Washington, D.C., April, 1970.

Apparao,Krishna M.V. and Hoffman,Jeffrey (1970), "Compton-Synchrotron Radiation from Pulsars." Astrophys.Lett., 5, 25.

Bethe,Hans A. and Ashkin,Julius (1953), "Passage of Radiations through Matter." Experimental Nuclear Physics, (v.1) , E. Segré (ed.), John Wiley and Sons, Inc., New York.

Boldt,E.A., Desai,U.D., Holt,S.S., Serlemitsos,P.J., and Silverberg, R.F. (1969), "Pulsed X-ray Emission of NP0532 in March, 1968." Nature, 223, 280.

Bradt,H., Mayer,W., Naranan,S., Rappaport,S., and Spada,G. (1967), "Evidence for X-Radiation from the Radio Galaxy M87." Astrophys.J.Lett., 150, L199.

Bradt,H., Rappaport,S., Mayer,W., Nather,R.E., Warner,B., Macfarlane, M., and Kristian,J. (1969), "X-Ray and Optical Observations of the Pulsar NP0532 in the Crab Nebula." Nature, 222, 728.

Butcher,J.C. and Messel,H. (1958), "Electron Number Distribution in Electron-Photon Showers." Phys.Rev., 112, 2096.

Butcher,J.C. and Messel,H. (1960), "Electron Number Distribution in Electron-Photon Showers in Air and Aluminum Absorbers." Nuc.Phys., 20, 15.

Reproduced with permission of the copyright owner. Further reproduction prohibited without permission.

Byram,E.T., Chubb,T.A., and Friedman,H. (1966), "Cosmic X-Ray Sources, Galactic and Extragalactic." Science, 152, 66.

Byram,E.T., Chubb,T.A., and Friedman,H. (1971), "Variability of X-Ray Emission from M87." Nature, 229, 544.

Cavrak,S. (1971), "The Production of Gamma Rays in the Atmosphere." Ph.D. Thesis, Dept. of Physics, Harvard University, unpublished.

Clark,G.W., Garmire,G.P., and Kraushaar,W.L. (1968), "Observations of High-Energy Cosmic Gamma Rays." Astrophys.J.Lett., 153, L203.

Clark,G.W., Garmire,G.P., and Kraushaar,W.L. (1970), "Review of Observational Results on γ-Ray Background." Non-Solar X- and Gamma-Ray Astronomy, I.A.U. Symposium No. 37, L. Gratton (ed.), D. Reidel Co., Dordrecht, Holland.

Clayton,Donald D. and Silk,Joseph (1969), "Measuring the Rate of Nucleosynthesis with a Gamma Ray Detector." Astrophys.J.Lett., 158, L43.

Damle,S.V. (1968), "Measurement of the Ratio $He^3/(He^3 + He^4)$ in the Primary Cosmic Radiation at Relativistic Energies." Ph.D. Thesis, University of Bombay, Tata Institute of Fundamental Research, Bombay, unpublished.

DeVaucouleurs,G. (1969), "Photometry of the Outer Corona of Messier 87." Astrophys.Lett., 4, 17.

Ducros,G., Ducros,R., Rocchia,R., and Tarrius,A. (1970), "Pulsations in the X-radiation of the Crab Nebula." Nature, 227, 152.

Duthie,J.G. (1968), "Gamma Ray Astronomy." Can.J.Phys., 46, S401.

Evans,Robley D. (1955), The Atomic Nucleus. McGraw Hill, New York.

Reproduced with permission of the copyright owner. Further reproduction prohibited without permission.

Fazio,G.G. (1967), "Gamma Radiation from Celestial Objects." Ann.Rev. Astron.Astrophys., 5, 481.

Fazio,G.G., Helmken,H.F., Rieke,G.H., and Weekes,T.C. (1969), "Upper Limits to the Emission of 10^{11}-eV Gamma Rays from Discrete Sources." Proc.Eleventh Intern.Conf.Cosmic Rays, Budapest.

Fazio,G.G. (1970), "X-Ray and Gamma Ray Astronomy." Review paper presented at the Sixth Inter-American Cosmic Ray Seminar; La Paz, Bolivia; July, 1970.

Felten,James E. (1968), "The Radiation and Physical Properties of the M87 Jet." Astrophys.J., 151, 861.

Fichtel,C.E., Kniffen,D.A., and Ögelman,H.B. (1969), "Results of Gamma-Ray Balloon Astronomy." Astrophys.J., 158, 193.

Fichtel,C.E., Kniffen,D.A., Hartman,R.C., and Sommer,M. (1971), Results Presented at American Physical Society Meeting, Washington,D.C.,April,1971

Fishman,G.J., Harnden,F.R.,Jr., Johnson,W.N.,III, and Haymes,R.C. (1969), "The Period and Hard-X-Ray Spectrum of NP0532 in 1967." Astrophys. J.Lett., 158, L61.

Floyd,F.W., Glass,I.S., and Schnopper,H.W. (1969), "Hard X-Rays from the Crab Pulsar." Nature, 224, 50.

Friedman,H. and Byram,E.T. (1967), "X-Rays from Sources 3C273 and M87." Science, 158, 257.

Fritz,G., Henry,R.C., Meekins,J.F., Chubb,T.A., and Friedman,H. (1969), "X-ray Pulsar in the Crab Nebula." Science, 164, 709.

Fritz,G., Meekins,J.F., Chubb,T.A., Friedman,H., and Henry,R.C. (1971), "The X-Ray Spectra of the Crab Nebula and NP0532." Astrophys.J. Lett., 164, L55.

Reproduced with permission of the copyright owner. Further reproduction prohibited without permission.

Frye,G.M.,Jr. and Smith,Lawrence H. (1966), "Upper Limits to Cosmic γ-Rays in the Range 30 to 500 MeV." Phys.Rev.Lett., 17, 733.

Frye,G.M.,Jr. and Wang,C.G. (1968), "Search for Gamma Rays from 3C273 and M87." Can.J.Phys., 46, S448.

Frye,G.M.,Jr., Staib,J.A., Zych,A.P., Hopper,V.D., Rawlinson,W.R., and Thomas,J.A. (1969), "Evidence for a Point Source of Cosmic Gamma Rays." Nature, 223, 1320.

Frye,G.M.,Jr. and Wang,C.G. (1969), "Survey of Possible Sources of Cosmic Gamma Rays above 50 MeV in the Northern Hemisphere." Astrophys.J., 158, 925.

Gould,R.J. and Burbidge,G.R. (1965), "High Energy Cosmic Photons and Neutrinos." Annales d'Astrophysique, 28, 171.

Greisen, Kenneth (1966), "Experimental Gamma Ray Astronomy." Perspectives in Modern Physics, R.E.Marshak (ed.), Interscience, New York.

Greisen, Kenneth (1969), "The Physics of Cosmic X-ray, Γ-ray and Particle Sources." Lectures given at the Brandeis University Summer Institute in Physics, 1968.

Grindlay,J.E. and Hoffman,J.A. (1971),"Compton-Synchrotron Spectrum of the Crab Nebula with the Pulsar Magnetic Field." Astrophys. Lett., to be published.

Haymes,R.C., Ellis,D.V., Fishman,G.J., Kurfess,J.D., and Tucker,W.H. (1968), "Detection of Hard X-Radiation from Virgo." Astrophys. J.Lett., 151, L9.

Haymes,R.C., Fishman,G.J., and Harnden,F.R.,Jr. (1970), "The Flux of Hard Radiation from M87." Non-Solar X- and Gamma-Ray Astronomy, I.A.U. Symposium No. 37, L.Gratton (ed.), D.Reidel Co., Dordrecht, Holland.

Hearn,David (1968), "Consistent Analysis of Gamma Ray Astronomy Experiments." Smithosonian Astrophysical Observatory Spec. Rept. No. 277.

Reproduced with permission of the copyright owner. Further reproduction prohibited without permission.

Helmken,H. and Hoffman,J. (1970), "Gas-Čerenkov Detector for Low Energy Gamma Ray Astronomy." Nucl. Inst. and Meth., 80, 125.

Israel, Martin H. (1969), "Cosmic-Ray Electrons Between 12 MeV and 1 GeV in 1967." J.Geophys.Res., 74, 4701.

Jelley,J.V. (1958), Čerenkov Radiation and its Applications. Pergamon Press, New York.

Kinzer,R.L., Noggle,R.C., Seeman,N., and Share,G.H. (1971),"Experiment to Detect Pulsed γ-Rays from the Crab Nebula." Nature, 229, 187.

Kniffen,D.A. and Fichtel,C.A. (1970), "Gamma Rays from the Galactic Center." Astrophys.J.Lett., 161, L157.

Kraushaar,W.L. (1969), "Instrumental Aspects of Gamma Ray Astronomy: Serious Need for New Ideas and Developments." Astronautics and Aeronautics, 7, 28.

Kurfess,J. (1971), Private Communication to G.G.Fazio.

LePrince-Ringuet,Louis (1950), Cosmic Rays. Prentice-Hall, New York.

May,T.C. and Waddington,C.J. (1969), "A Search for Energetic Gamma-Ray Emission from the Supernova Remnant Cassiopeia A." Astrophys.J., 156, 437.

McClintock,J.E., Lewin,W.H.G., Sullivan,R.J., and Clark,G.W. (1969), "High-Energy X-Ray Study of M87." Nature, 223, 162.

Meyer,Peter (1969), "Cosmic Rays in the Galaxy." Ann.Rev.Astron.Astrophys., 7, 1.

Peterson,L.E. (1970), "Properties of Individual X-Ray Sources." Non-Solar X- and Gamma-Ray Astronomy, I.A.U. Symposium No. 37, L.Gratton (ed.), D. Reidel Co., Dordrecht, Holland.

Reproduced with permission of the copyright owner. Further reproduction prohibited without permission.

Puskin, Jerome S. (1970), "Low-Energy Gamma Rays in the Atmosphere." Smithsonian Astrophysical Observatory Spec.Rept.No. 318.

Rieke,G.H. and Weekes,T.C. (1969), "Production of Cosmic Gamma Rays by Compton Scattering in Discrete Sources." Astrophys.J., 155, 429.

Rossi,Bruno (1948), "Interpretation of Cosmic Ray Phenomena." Rev.Mod. Phys., 20, 537.

Rossi,Bruno (1952), High Energy Particles. Prentice-Hall, N.J.

Rossi,Bruno (1957), Optics. Addison-Wesley, Reading, Mass.

Sandström,A.E. (1965), Cosmic Ray Physics. Interscience, New York.

Scott,William T. (1963), "The Theory of Small-Angle Multiple Scattering of Fast Charged Particles." Rev.Mod.Phys., 35, 231.

Shklovskii,I.S. (1967), "The Nature of the X-Radiation of X-Ray Galaxies." Sov.Astron.-A.J., 11, 45.

Stecker,F.W. (1969), "Primordial Cosmic Ray Sources." Nature, 224, 870.

Stecker,F.W. (1970), "The Cosmic γ-Ray Spectrum from Secondary Particle Production in Cosmic-Ray Interactions." Astrophys.Space Sci., 6, 377.

Tamura,M. (1965), "A Study of Electron-Photon Showers by the Monte Carlo Method." Prog.Theor.Phys., 34, 912.

Vasseur,J., Agrinier,B., and Scarsi, L. ,(1970), Private Communication of Results of the Saclay-Milan-Palermo Gamma Ray Spark Chamber Collaboration

Verma,Satya Dev (1967), "Measurement of the Charged Splash and Re-Entrant Albedo of the Cosmic Radiation." J.Geophys.Res., 72, 915.

Reproduced with permission of the copyright owner. Further reproduction prohibited without permission.

Webber,W. and Chotkowski,Ch. (1967), "A Charged Particle Telescope for Use in the Measurement of the Cosmic Ray Electron Spectrum in the Energy Range 10 MeV-2 GeV." Nucl.Inst. and Meth., 49, 45.

Wolfendale,A.W. (1963), Cosmic Rays. Philosophical Library, New York.

Zerby,C.D. and Moran,H.S. (1963), "Studies of the Longitudinal Development of Electron-Photon Cascade Showers." J.Appl.Phys., 34, 2445.

Reproduced with permission of the copyright owner. Further reproduction prohibited without permission.